UC San Diego
UC San Diego Electronic Theses and Dissertations

Title
Modeling and Characterization of Efficient Carrier Multiplication in Highly Co-doped Semiconductors and Disordered Materials

Permalink
https://escholarship.org/uc/item/50c6z8jw

Author
Niaz, Iftikhar Ahmad

Publication Date
2019

Peer reviewed|Thesis/dissertation

eScholarship.org Powered by the California Digital Library
University of California

UNIVERSITY OF CALIFORNIA SAN DIEGO

Modeling and Characterization of Efficient Carrier Multiplication in Highly Co-doped Semiconductors and Disordered Materials

A dissertation submitted in partial satisfaction of the requirements for the degree Doctor of Philosophy

in

Electrical Engineering (Applied Physics)

by

Iftikhar Ahmad Niaz

Committee in charge:

Professor Yu-Hwa Lo, Chair
Professor Richard Averitt
Professor Chung Kuan Cheng
Professor Shadi Ahmad Dayeh
Professor Tse Nga Ng

2019

Copyright

Iftikhar Ahmad Niaz, 2019

All rights reserved.

The Dissertation of Iftikhar Ahmad Niaz is approved, and it is acceptable in quality and form for publication on microfilm and electronically:

____

____

____

____

____

Chair

University of California San Diego

2019

DEDICATION

To Allah (God) first and foremost and His prophet Muhammad, then my parents, wife and son and all others who helped me get through this long journey.

TABLE OF CONTENTS

Signature Page iii

Dedication iv

Table of Contents v

List of Figures viii

List of Tables xi

Acknowledgements xii

Vita xv

Abstract of the Dissertation xvii

Chapter 1 Introduction 1

1.1 Photodetectors 1

1.2 Solid-State Photodetectors 2

1.2.1 Photoconductors 2

1.2.2 Photodiodes 3

1.2.3 Avalanche Photodiode 4

1.2.4 Single Photon Avalanche Detector 6

1.3 Motivations and Challenges 7

1.4 Dissertation Outline 8

References 10

Chapter 2 Demonstration of Cycling Excitation Process 12

2.1 Introduction to Cycling Excitation Process (CEP) 12

2.1.1 Physical Mechanism 12

2.1.2 Experimental Results 15

2.2 First Principle Modeling of Localization 17

2.2.1 A Brief Introduction to Density Functional Theory (DFT) 17

2.2.2 Kohn-Sham Equation 18

2.3 Simulation Results from DFT Calculation 21

2.3.1 Electronic Band Structure and Density of States 21
2.3.2 Localization of Wavefunction 23
2.4 Conclusion … 26
References 27
Chapter 3 Carrier Multiplication in Disordered Materials 29
3.1 Demonstration of Carrier Multiplication in Disordered Materials 29
3.1.1 Motivation 29
3.1.2 Design of Amorphous Silicon (a-Si) Detector 30
3.1.3 Experimental Results 31
3.2 Modeling of Gain Mechanism in Amorphous Silicon 32
3.2.1 Numerical Modeling 33
3.2.2 Applicability of Local Field Dependent Velocity Model 36
3.2.3 Applicability of Local Field Dependent Impact Ionization Model 38
3.3 Results and Discussions 41
3.3.1 DC Gain Characteristics 42
3.3.2 Frequency Response 43
3.3.3 Gain Dependence on a-Si Thickness 46
3.4 Proposed Gain Mechanism in Amorphous Materials 48
3.5 Conclusion 51
References 53
Chapter 4 Quantitative Analysis of Defect Assisted Carrier Multiplication in Amorphous Silicon..56
4.1 DAP Assisted Carrier Multiplication Formulation 56
4.1.1 Theoretical Framework 56
4.1.2 Quantum Mechanical Formulation of Carrier Multiplication Rate 59
4.1.3 Carrier Multiplication Coefficient Calculation 63

4.2 Results and Discussions 68
4.2.1 Defect Assisted Carrier Multiplication Rate 68
4.2.2 Distribution Function and Carrier Multiplication Coefficient 70
4.2.3 Gain Dependence on a-Si Thickness..72
4.3 Conclusion 74
References 77
Chapter 5 Conclusions 80
5.1 Thesis Summary 80
5.2 Outlook 81
References 83
Appendix A: Modeling Gain Mechanisms in Amorphous Materials 85
A.1 Local Electric Field Dependent Impact Ionization Model 85
A.2 Parameters for Device Simulation of Chapter 3 88
Appendix B: Defect Assisted Multiplication Coefficient 90
B.1 Quantum Mechanical Calculation of Scattering Rate 90
B.2 Band Structure and Density of States 92
B.3 Average Kinetic Energy versus Thickness 92
B.4 Parameters for Device Simulation...93
References 94

LIST OF FIGURES

Figure 1.1: Schematic diagram of a photoconductor 3

Figure 1.2: Schematic diagram of a photodiode 4

Figure 1.3: The energy band diagram of an APD under illumination and large reverse bias conditions showing avalanche multiplication in the space charge region 5

Figure 2.1: Energy versus momentum diagram for a band-to-band transition in an indirect bandgap semiconductor with and without localized states involved. 13

Figure 2.2: Illustration of the cycling excitation process. The processes from (a) to (d) take place in sequence: **(a)** Primary photo generated electron excites an electron from a compensating acceptor........14

Figure 2.3: Bias, input light intensity, and temperature dependence of gain. (a) Bias and input light intensity dependence of gain. The illumination (635 nm) light power is represented by the...........16

Figure 2.4: Interacting system is mapped to a non-interacting fictitious system 19

Figure 2.5: Self-consistent scheme of density functional theory 20

Figure 2.6: (a) Band Diagram for 54 atoms Si supercell (L', Γ', X' denotes supercell Brillouin zone edge), (b)Band Diagram after unfolding (L, Γ, X denotes primitive cell Brillouin Zone edge), (c) BP.....22

Figure 2.7: Density of states comparison for bulk and BP doped Silicon.....23

Figure 2.8: Position of Phosphorous and Boron atoms along $[\bar{1}11]$ direction (In the case of bulk Si, all atoms are Si) 24

Figure 2.9: (a) Localization of probability density around Boron atom at Highest ..energy band below band gap, (b) corresponding k point

bulk Si band diagram and (c) corresponding k point at BP 25

Figure 3.1: (a) Schematic diagram of a-Si:H CEP device structure with the material and function of each layer. The photodiode operates under reverse bias. (b) Dark current versus reverse bias 31

Figure 3.2: DC photo-current gain of a carbon-doped a-Si:H CEP photodiode. Photodiode has a 30μm diameter photosensitive area 32

Figure 3.3: Calculated Gain versus Reverse Bias for (a) different trap density, (b) different mobility ratio, (c) different trap energy levels and (d) junction modulation gain coupled with carrier 42

Figure 3.4: (a) Measured gain vs frequency. (b) Simulated gain versus frequency when only traps (dashed) and only carrier multiplication (solid) are considered. Both curves are 45

Figure 3.5: (a) Photocurrent versus Electric Field for two different a-Si thicknesses, (b) Field dependence of electron impact ionization coefficient for different thickness of a-Si. The curves were 47

Figure 3.6: Pictorial representation of carrier multiplication processes in c-Si (a-d) and a-Si (bottom row, e-h). (a) and (e) show photogeneration of e-h pair by incidence of light. (b) and (f) show the hole 50

Figure 4.1: Schematic diagram of DAP pair assisted electron multiplication process in a-Si. (a) Before the start of multiplication process there are a high energy electron (state 1) and occupied acceptor 59

Figure 4.2 DAP assisted multiplication rate for (a) electrons and (b) holes at different kinetic energy. Solid curve is the fitted curve used for distribution function and gain calculation..................................69

Figure 4.3: Normalized electron distribution function at the end of a 40nm thick a-Si layer under different electric fields. Normalization means the distribution function is divided by the electron 70

Figure 4.4: Carrier multiplication coefficient of (a) electrons and (b) holes for different thickness of a-Si...71
Figure 4.5: Bias dependence of carrier multiplication coefficient of (a) electrons and (b) holes for different thickness of a-Si 73
Figure 4.6: (a) Gain of a-Si photodetector devices for various thickness of a-Si. (b) Gain of simulated and experimental photodetector device of ~30nm a-Si 74

LIST OF TABLES

Table A.1: Material Properties 88

Table A.2: Impact Ionization Parameters 88

Table A.3: Junction Modulation Parameters...89

Table B.1: Material Properties 93

ACKNOWLEDGEMENTS

First, I am grateful to my advisor, Professor Yu-Hwa Lo, who has been constantly guiding me throughout my PhD program. He was always involved and dedicated in collectively solving research problems along with encouraging personal development and thinking process of the student. I also like to thank Professor Shadi Dayeh who was my first contact at UCSD and helped me a lot through the long, tedious admission process. Also, after starting PhD, several discussions with him both as a course teacher and committee member helped me immensely. I'm also thankful to Professor Ng, Professor Averitt and Professor Cheng for serving in my committee and for the insightful feedback on my research. Professor Lu Sham has also worked with us for over two years and provided his valuable input on the theoretical end of the research. I'm also humbled to interact with Professor S.S. Lau, Professor Peter Asbeck, Professor Yuan Taur, Professor Kuzum, Professor Tzu-Chieh Hsueh in different capacity (course teacher, TA professor etc.).

I also want to thank my former lab-mates. Dr. Samia Nawar Rahman was my first mentor and guided me immensely in my first couple of quarters to adjust to new environment and make balance between research and courses. Dr. Yuchun Zhou and Dr. Yu-Hsin Liu introduced me to clean room work. I am grateful to both of them, specially Dr. Liu who I had the opportunity to learn almost every aspect of research beginning from fabrication to experiment, measurement, lab set up and overall a humble human being. I had the pleasure of spending long time with Dr. David Hall and learned a lot from him. I also had the pleasure of interacting with Dr. Arthur Zhang, Dr. Baoxia Li, Dr. Mahmut Sami Kavrik, Dr. Roger Liu, Dr. Tony Yen, Dr. Tiantian Zhang, Dr. Wei Cai and Dr. Yi Gu. I also need to thank the Nano3 staff for the excellent support they provided which made my research possible: Larry Grissom, Sean Parks, Ivan Harris, Dr. Xuekun Lu, Dr. Raffaella Fior, Ryan Anderson, Dr. Maribel Montero, and Dr. Bernd Fruhberger.

I would also like to thank my current and recently graduated lab mates who I collaborated intensively and also had so much interaction to grow myself as a better person. Mohammad Abu Raihan Miah has been my primary collaborator and mentor in many aspects of theoretical research which I appreciate greatly. Alex Zhang and Dr. Lujiang Yan were among my first colleagues who always helped me during ups and downs. I'm also grateful to Yugang Yu, Zihan Xu, Samir Damle, Ramkumar Subramanian, Yi-Huan Tsai, Ping-Wei Chen, Jiayun Zhao, Shaurya Arya, Zijiang Zheng for their help, friendship and collaboration.

I also had the pleasure of working and interacting with some great people who I need to mention: Dr. Renjie Chen, Dr. Atsunori Tanaka, Dr. Mehran Ganji, Dr. Poy Supanee Sukrittanon, Yun Goo Ro, Ahmed Youssef, Siam Umar Hussain, Roisul Hasan, Ibrahim Awwal, Iftekhar Chowdhury, Ahmed Naguib, Syed Sadat Nazrul, Dr. Hasan Imam and many others who I might forgot to mention.

Last but not the least, I am indebted to my family members for their immense sacrifice to make the person I'm today. My parents Dr. Niaz Ahmed and Dr. Nazma Islam Nargis were with me at every step of my life. Both being medical doctors, instilled in me the value of helping fellow human beings. My in laws, Dr. Mohammad Rezwan Khan and Mrs. Shahana Begum also treated me as a son and always helped me. Specially, Dr. Khan being a professor of electrical engineering in Bangladesh, had often taken out the time in his daily schedule to discuss with me things pertaining to research. Finally, I am grateful to my wife Dr. Nabeela Khan and our two and a half years old son Abdullah Shakir Ahmad. My wife's patience, perseverance and joyfulness have constantly motivated me to move forward with my efforts. Abdullah has not only filled our life with joyful bliss, but also has added a new perspective to it.

Portions of Chapter 2 have been published in the following publications: Y. H. Liu, L. Yan, A. C. Zhang, D. Hall, I. A. Niaz, Y. Zhou, L. J. Sham, and Y. H. Lo, "Cycling excitation process: An ultra-efficient and quiet signal amplification mechanism in semiconductor," Applied Physics Letters 107, 053505 (2015); M. A. R. Miah*, I.A. Niaz*, Y. H. Liu, D. Hall, and Y. H. Lo, "A high-efficiency low-noise signal amplification mechanism for photodetectors," Proc. SPIE 10108, Silicon Photonics XII, 101080X, 20 February 2017; (* →co-first authors). The dissertation author was a coauthor/co-first author of these papers.

Portions of Chapter 3 have been published in the following publications: L. Yan, Y. Yu, A. C. Zhang, D. Hall, I. A. Niaz, M.A.R. Miah, Y.H. Liu, Y.H. Lo "An amorphous silicon photodiode with 2 THz gain-bandwidth product based on cycling excitation process," Applied Physics Letters 111, 101104 (2017); I. A. Niaz, M.A.R. Miah, L. Yan, Y. Yu, Z. He, Y. Zhang, A. Zhang, J. Zhou, Y.H. Zhang and Y-H. Lo "Modeling Gain Mechanisms in Amorphous Silicon due to efficient carrier multiplication and trap induced junction modulation", Journal of Lightwave Technology, Vol: 37, Issue: 19, pp: 5056-5066, 2019. The dissertation author was a coauthor/primary author of these papers.

Portions of Chapter 4 has been submitted for publication in M.A.R. Miah*, I.A. Niaz*, Y.H. Lo, "Defect Assisted Carrier Multiplication in Amorphous Silicon"; IEEE Journal of Quantum Electronics; (* →co-first authors). The dissertation author is a co-first author of this material.

VITA

2012	Bachelor of Science, Bangladesh University of Engineering and Technology, Electrical and Electronic Engineering
2016	Master of Science, University of California San Diego Electrical Engineering (Applied Physics)
2019	Doctor of Philosophy, University of California San Diego Electrical Engineering (Applied Physics)

PUBLICATIONS

1. M.A.R. Miah*, **I.A. Niaz**,* Y-H. Lo, "Defect Assisted Carrier Multiplication in Amorphous Silicon", Submitted at IEEE Journal of Quantum Electronics

   *co-first author

2. **I. A. Niaz**, M.A.R. Miah, L. Yan, Y. Yu, Z. He, Y. Zhang, A. Zhang, J. Zhou, Y.H. Zhang and Y-H. Lo "Modeling Gain Mechanisms in Amorphous Silicon due to efficient carrier multiplication and trap induced junction modulation", Journal of Lightwave Technology, Vol: 37, Issue: 19, pp: 5056-5066, 2019

3. J. Zhou, M.A.R. Miah, Y. Yu, A.C. Zhang, Z. Zeng, S. Damle, **I.A. Niaz**, Y. Zhang, Y-H. Lo, "Room-temperature long-wave infrared detector with thin double layers of amorphous germanium and amorphous silicon", Optics Express, 2019 (accepted)

4. L. Yan, Y. Yu, Z. Xu, **I. A. Niaz**, M.A.R Miah, A. Zhang, J. Zhou, Y-H. Lo, "Low Noise, High Gain-Bandwidth Photodetectors Using Cycling Exciting Process (CEP) as Amplification Mechanism", IEEE International Conference on Electron Devices and Solid State Circuits (EDSSC), 2018

5. M.A.R. Miah*, **I. A. Niaz***, Y. Liu, D. Hall and Y-H. Lo "A high-efficiency low-noise signal amplification mechanism for Si photonic detectors", Photonic West OPTO 2017 Conference

   *co-first author

6. L. Yan, Y. Yu, A. Zhang, D. Hall, **I. A. Niaz**, M.A.R. Miah, Y-H. Liu, Y-H. Lo, "An amorphous silicon photodiode with 2 THz gain-bandwidth product based on cycling excitation process", Applied Physics Letters 111, 101104 (2017).

7. T. Zhang, T-H. Ku, Y. Han, R. Subramanian, **I. A. Niaz**, H. Luo, D. Cheng, J-J. Huang, Y-H. Lo, "Transient Induced Molecular Electronic Spectroscopy (TIMES) for study of protein-ligand interactions", Scientific Reports. 2016;6:35570

8. Y-H. Liu, L. Yan, A. C. Zhang, D. Hall, **I. A. Niaz**, M.S. Kavrik and Y-H. Lo " An ultra-efficient internal mechanism to amplify photoresponse for Si and compound semiconductor devices", 2016 IEEE Photonics Society Summer Topical Meeting Series (SUM), 17-18

9. Y-H. Liu, A. C. Zhang, M. A. R. Miah, D. Hall, **I. A. Niaz**, L. Yan, Y. Yu, M. S. Kavrik, and Y-H. Lo, "Cycling excitation process for light detection and signal amplification in semiconductors", Proc. SPIE 9933, Optical Sensing, Imaging, and Photon Counting: Nanostructured Devices and Applications 2016, 99330C (26 September 2016)

10. Y-H. Liu, L. Yan, A. Zhang, D. Hall, **I. A. Niaz**, Y. Zhou, L. J. Sham and Y-H. Lo "Cycling excitation process: An ultra efficient and quiet signal amplification mechanism in semiconductor", Appl. Phys. Lett. 107, 053505 (2015)

ABSTRACT OF THE DISSERTATION

Modeling and Characterization of Efficient Carrier Multiplication in Highly Co-doped Semiconductors and Disordered Materials

by

Iftikhar Ahmad Niaz

Doctor of Philosophy in Electrical Engineering (Applied Physics)

University of California San Diego, 2019

Professor Yu-Hwa Lo, Chair

This thesis offers modeling of a newly discovered gain mechanism for various photodetection applications. Conventional avalanche photodetectors have been in use for the past four decades with impact ionization being the underlying carrier multiplication mechanism. However, tradeoff between sensitivity, dynamic range and bandwidth are some of the drawbacks of the present day photodetection technology. The newly discovered cycling excitation process

(CEP) can be a potential candidate to address these issues with linear photo response, single photon sensitivity and high gain bandwidth product. The key feature of CEP is introduction of counter dopants in p-n junction silicon diode, with which the efficiency of auger excitation can be enhanced to great extent by facilitating relaxation of k selection rule. Higher uncertainty in k spaces dictates localization of carriers in real space. Hence, an initial hot carrier can excite electron-hole pair between localized states (e.g. from states closer to valence band to states closer to conduction band) at much lower bias. Another essential component of CEP is phonon/field assisted tunneling from localized states to mobile bands. Contrary to other photodetectors, phonons, actually, play a positive role in achieving gain. Experimentally gain of ~4000 at only 4V have been achieved in the CEP test structure along with photo response dependence on input light power, which is helpful for photon number resolving. Temperature dependent measurement also shows the positive role of phonons.

Density functional theory calculation shows the change in band structure with doping bulk crystalline silicon with boron (B) and phosphorous (P) simultaneously. Comparison of density of states exhibits existence of states inside band gap. Furthermore, charge density plot clearly demonstrates electron and hole localization centered around P and B atoms respectively. Hence, highly counter doping with BP atoms turns the crystalline silicon into a quasi-disordered material.

Since, highly counter doping introduces disorder in silicon, with this notion naturally disordered materials are explored as possible CEP gain media. Amorphous materials have low mobility due to their nature of disorder. Surprisingly, amorphous silicon (a-Si) photodiodes with thin a-Si layer (~40nm) have shown a gain-bandwidth product of over 2 THz with very low excess noise. To unveil the true gain mechanism, the thesis further delves into theoretical modeling and numerical analysis along with experimental data at different frequencies. Evidence of highly

effective carrier multiplication process within a-Si as the primary gain mechanism, especially at high frequency is shown. There is also trap-induced junction modulation at much lower frequency. The analysis further suggests that the carrier multiplication process in thin a-Si can be much more efficient than in thick a-Si, even stronger than single crystalline Si in some cases. Although seemingly counter intuitive, this is consistent with the proposed cycling excitation process (CEP) where the localized states in the bandtails of disordered materials such as a-Si relax the k-selection rule and increase the rate of carrier multiplication.

A more rigorous quantum mechanical scattering rate calculation also demonstrates the increase of strength of carrier multiplication with the presence of localized states and the increase of ionization coefficient with decreasing thickness of gain medium. A theoretical framework is offered to calculate the carrier multiplication process in a-Si or other disordered materials involving donor acceptor pairs (DAPs) and to answer several key and seemingly counter intuitive questions such as why amorphous silicon can be more efficient carrier multiplication material than single crystal silicon, why low carrier mobility of amorphous material helps rather than hurt carrier multiplication process, and why thin a-Si is more efficient than thick a-Si in carrier multiplication.

Chapter 1

Introduction

Semiconductor photodetectors detect optical signal by converting light into electrical signals. They are an essential component for optical communications for scientific and industrial applications, biomedical imaging, consumer electronics and so forth. Photodetectors mostly based on silicon have been widely used. This chapter presents an overview of different photodetection mechanism and the conventional physics employed behind them.

1.1 Photodetectors

Photodetectors use photoelectric effect to convert light into measurable electrical signal. Optical fibers have brought revolution in long distance communication where pulses of light travel through the fibers and then converted into binary electrical signal. Infrared photodetectors have been used for far range communication [1]. Biomedical applications also require photodetectors in the visible wavelength region for high contrast and sensitive imaging [2]. Moreover, near-IR wavelength detectors (~1060nm) have been used in medical and defense applications.

Some applications of photodetectors require very high sensitivity even to the level of single photon. In deep space communication, when the signal reaches the detector it becomes extremely weak. Hence, the necessity of single photon detector arises. The novel field of quantum communication also calls for single photo detection sensitivity [3].

1.2 Solid-State Photodetectors

Solid state photodetectors have been in forefront for optical fiber communications. Photodetectors at the 850nm, 1310nm and 1550nm wavelength bands are the receiving component in these systems. Solid state detectors for fiber optic communications commonly use InGaAs and InP for light absorption and carrier transport, respectively [4]. Silicon photodetectors are potential candidate for integration of photonics with existing CMOS processes. To date avalanche photodiodes (APD) have been considered as the most sensitive solid-state detectors due to their internal gain and relatively low noise compared to other types of detectors [4]–[7].

A photodetector is considered to have high resolution if the output has a linear relation with incident photon (i.e. photocurrent varies linearly with input photon numbers). Another figure of merit of photodetectors is signal to noise ratio (SNR), which in ideal case, should be only from thermal noise of the external circuit.

1.2.1 Photoconductors

A photoconductor is a piece of semiconductor (bulk or thin film form) with ohmic contacts connected to opposite sides. When light is incident on the surface of the photoconductor, electron-hole pairs are generated and increases the conductivity of the semiconductor.

The photocurrent can be expressed as

$$I_{ph} = q(\mu_n + \mu_p)G_0\tau_n\frac{AV}{L} \approx q\mu_n G_0\tau_n\frac{AV}{L} \qquad (1.1)$$

Here, G_0 is the optical generation rate, A is the surface area, V is the applied voltage and L is the length of the device. Since, electron mobility, μ_n is higher than hole mobility, μ_p, hence we

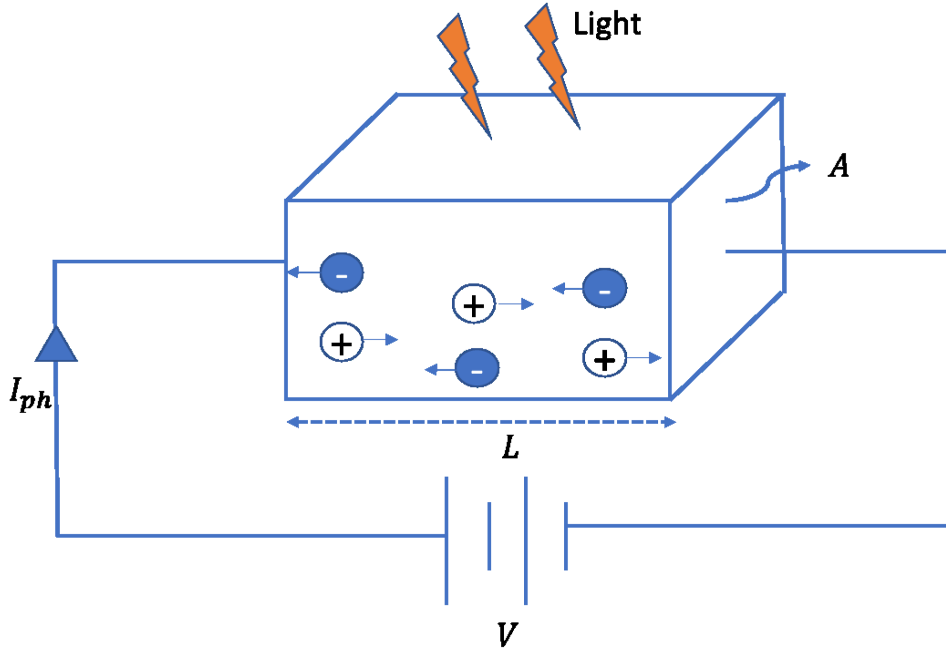

Figure 1.1: Schematic diagram of a photoconductor

can reasonably approximate as above $\left(i.e.\ \left(\mu_n + \mu_p\right) \approx \mu_n\right)$. τ_n denotes the lifetime of an electron before recombining with a hole. Using the relations, $\frac{V}{L} = \mathcal{E}; v_d = \mu_n \mathcal{E}; v_d = \frac{L}{\tau_t}$; we can rewrite the above:

$$I_{ph} = qG_0AL\frac{\tau_n}{\tau_t} \quad (1.2)$$

Here, τ_t is the transit time of carrier. The photoconductive gain is then given by

$$g_{ph} = \frac{\tau_n}{\tau_t} \quad (1.3)$$

1.2.2 Photodiodes

A photodiode has a structure similar to a regular semiconductor p-n junction or a p-i-n diode and is operated under reverse bias for optical signal detection. In the presence of light with

photon energy greater than the bandgap of the semiconductor, electrons from the valence band can be excited to the conduction band where they occupy mobile states. These free carriers are then swept by the built-in electric field across the p-n junction and collected at electrodes as current. The photocurrent is determined by the generation rate and absorption rate.

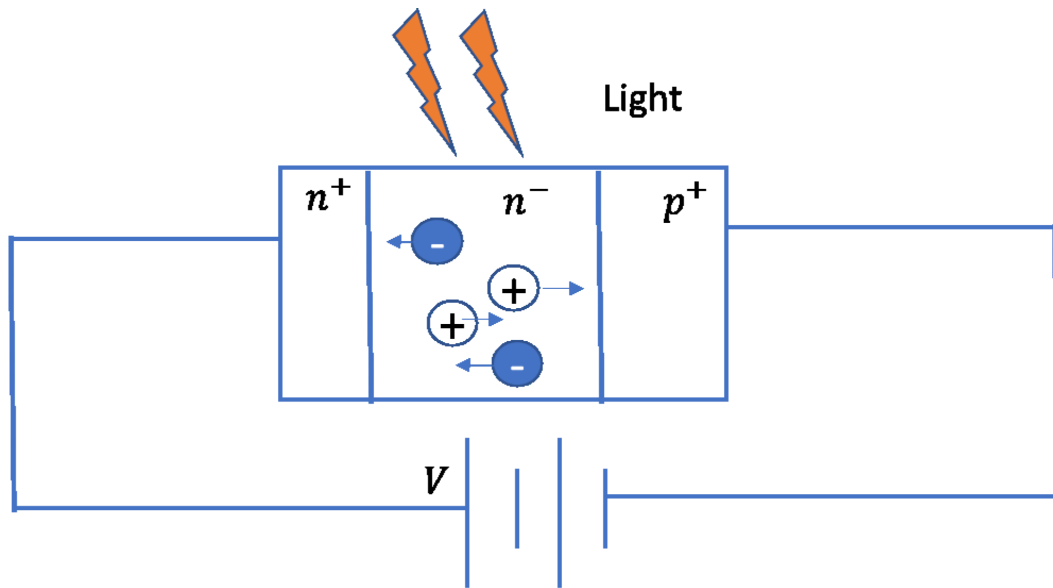

Figure 1.2: Schematic diagram of a photodiode

1.2.3 Avalanche Photodiode

Avalanche photodiodes (APDs) employ avalanche multiplication as their operating principle [8]–[10]. They operate at very high reverse bias almost close to their breakdown. When incident light generates an electron-hole pair, due to high voltage, the electron acquires high kinetic energy, and impact ionization can occur when collisions between carriers take place. Impact ionization produces more energetic electrons and holes and these carriers can generate further impact ionizations to produce more electron-hole pairs. Such processes can repeat to produce gain until it reaches a steady state or the limit determined by the series resistance and the external

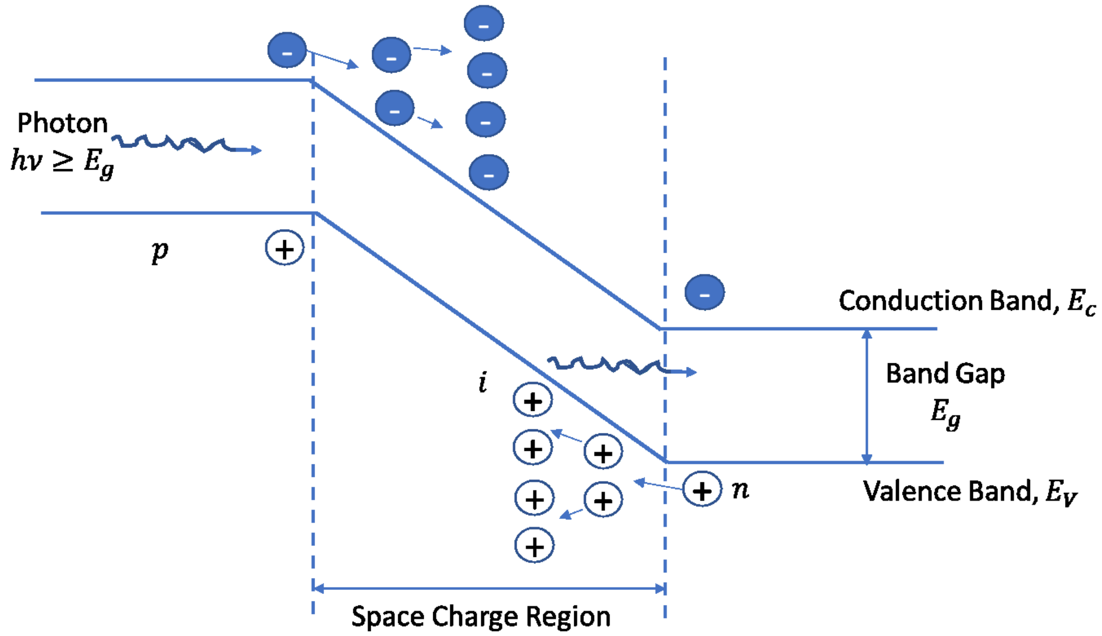

Figure 1.3: The energy band diagram of an APD under illumination and large reverse bias conditions showing avalanche multiplication in the space-charge region.

circuitry [11]. This avalanche multiplication process is illustrated in Fig. 1.3.

The impact ionization rate $\alpha_n(\mathcal{E})$ of electrons and $\alpha_p(\mathcal{E})$ of holes are defined as the number of electron and hole pairs generated by that electron or hole in a unit distance in the electric field. $\alpha_e(\mathcal{E})$ and $\alpha_p(\mathcal{E})$ depend on the electric field strength and the semiconductor band structure [12], [13].

$$\alpha_n(\mathcal{E}) = A_n \exp\left(-\left(\frac{B_n}{\mathcal{E}}\right)^{m_n}\right) \quad (1.1)$$

$$\alpha_p(\mathcal{E}) = A_p \exp\left(-\left(\frac{B_p}{\mathcal{E}}\right)^{m_p}\right) \quad (1.2)$$

$A_{n,p}$, $B_{n,p}$, $m_{n,p}$ are all ionization coefficients which can be determined empirically for a given material to give the ionization rate as a function of electric field, for example for Indium

Phosphide [14], and silicon [15].

Multiplication gain of electrons in a p-i-n diode with depletion layer width of W can be expressed as [11]

$$M = \left\{ 1 - \int_{0}^{W} \alpha_n \left[e^{-\int_x^W (\alpha_n - \alpha_p) dx'} \right] dx \right\}^{-1} \quad (1.3)$$

Here, $\alpha_{n,p}$ are spatially dependent due to non-uniformities of electric field or change of material. For uniform field and hence spatially uniform ionization rates the expression deduces to

$$M = \frac{1-k}{e^{-\alpha_n W[1-k]} - k} \quad (1.4)$$

Where, $k = \frac{\alpha_p}{\alpha_n}$. When the denominator becomes zero, the gain approaches infinity and the voltage that gives rise to infinite gain is called the breakdown voltage.

APDs are biased close to but below breakdown voltage. This allows the output signal to linearly vary with input optical power i.e. the detectors have photon number resolving capability. For optical fiber communications, InP based APDs have been used with speed of 10GHz [6]. However, both thermally generated (dark current) and photoexcited carriers (photocurrent) go through the same impact ionization processes. Hence, there is a trade-off between high gain and high dark current and noise.

1.2.4 Single Photon Avalanche Photodetector

As shown earlier impact ionization coefficients are strongly dependent on electric field and so is the gain of an APD. Single photon avalanche detectors are a category of avalanche photodetectors which operate above breakdown voltage. In this mode, even a small amount of

incident light can initiate the impact ionization process and the gain becomes very high and approaches infinite. Because of extremely high gain, a single photon can generate a strong signal by triggering an avalanche event. This mode of operation is called Geiger mode operation and are a good choice for single photon detection [16]–[19].

1.3 Motivations and Challenges

In Avalanche photodetectors, the gain is finite and moderately low depending on the applied field. Because of finite gain, input number of photons determines the output current and as such from output current, input power can be extrapolated. The state-of-the-art conventional detectors have a poor sensitivity due to the low operating gain and therefore the minimum number of detectable photons within a pulse signal is a few hundred [20].

Single photon APDs are superior in terms of sensitivity compared to conventional mode APDs. But as gain approaches infinite in these devices, they can be damaged by higher optical power and consequently higher current density. The device has to be quenched by an external circuit and output signals are of same strength for different number of input photons. So, the dynamic range of these devices is limited. No information regarding the input photon numbers can be extracted [21]. Another unwarranted case for SPADs are higher after pulsing, an effect by which impact ionization is initiated by carriers released from defect states

A highly sensitive photodetector with linear response will be of great use and if operated at low bias, will be compatible for CMOS integration. Avalanche multiplication induced by impact ionization is the primary internal signal multiplication process and requires 30-200V of operating voltage.

With these motivations, our group have been working on a novel carrier multiplication

process, capable of embodying the desired characteristics. With the new physical mechanism, we have successfully demonstrated a tremendous gain of ~4000 only at 5V reverse bias in silicon devices [22] and explored the new mechanism in other materials such as amorphous silicon [23]. With the promising results from the newly discovered internal carrier multiplication discovery, a thorough investigation of the physics and exploration of this gain mechanism in different materials is called for.

1.4 Dissertation Outline

This dissertation aims to physically model the new gain mechanism to have a deeper understanding and use that to extend this gain in new materials for various applications. The second chapter will firstly, discuss the experimental observations and rational behind the newly discovered gain mechanism, named cycling excitation process (CEP) and then show from first principle calculation the validity of the proposed physical picture. The main difference with the conventional impact ionization process of this new gain mechanism is introduction of counter doping and thus creating localized states and relaxing k selection rule required for momentum conservation in impact ionization process. The detailed results of band structure calculation, density of states and localization of carriers will be presented from density functional theory calculation.

The next chapter shows the extension of a similar gain mechanism in other materials involving localized states (e.g. amorphous silicon). This chapter will provide the experimental observation and will show from numerical simulation and physical reasoning, the unequivocal presence of the gain mechanism despite any nonideal effect from trap induced junction modulation. This chapter will end with showing with proper choice of thickness of amorphous material, the effective carrier multiplication coefficient can be enhanced, in some cases, even

higher than crystalline silicon material.

Chapter 4 presents a theoretical framework to calculate the carrier multiplication process in a-Si or other disordered materials involving donor acceptor pairs (DAPs). The analysis establishes the relations between detector characteristics and key parameters such as the density of band tail states, layer thickness, and applied electric field. Using the calculated carrier multiplication coefficients, voltage dependent gain of the device will be computed to show good agreement with the measured results of a-Si cycling excitation process (CEP) detectors.

Finally, chapter 5 concludes the thesis and sets the outlook for prospective directions.

References:

[1] H. Hemmati, A. Biswas, and I. B. Djordjevic, "Deep-Space Optical Communications: Future Perspectives and Applications," *Proceedings of the IEEE*, vol. 99, no. 11, pp. 2020–2039, Nov. 2011.

[2] R. Cubeddu, D. Comelli, C. D'Andrea, P. Taroni, and G. Valentini, "Time-resolved fluorescence imaging in biology and medicine," *Journal of Physics D: Applied Physics*, vol. 35, no. 9, pp. R61–R76, May 2002.

[3] R. H. Hadfield, "Single-photon detectors for optical quantum information applications," *Nature Photon*, vol. 3, no. 12, pp. 696–705, Dec. 2009.

[4] J. C. Campbell, "Recent Advances in Telecommunications Avalanche Photodiodes," *Journal of Lightwave Technology*, vol. 25, no. 1, pp. 109–121, Jan. 2007.

[5] G. P. Agrawal, *Fiber-optic communication systems*, 4th ed. New York: Wiley, 2010.

[6] Y. Kang, H-D. Liu, M. Moorse, M. J. Paniccia, M. Zadka, S. Litski, G., Sarid, A. Pauchard, Y-H., Kuo, H-W. Chen, W-S. Zaoui, J.E. Bowers, A. Beling, D.C. McIntosh, X. Zheng and J.C. Campbell, "Monolithic germanium/silicon avalanche photodiodes with 340 GHz gain–bandwidth product," *Nature Photonics*, vol. 3, no. 1, pp. 59–63, Jan. 2009.

[7] S. Nawar Rahman, D. Hall, and Y.-H. Lo, "Non-Geiger mode single photon detector with multiple amplification and gain control mechanisms," *Journal of Applied Physics*, vol. 115, no. 17, p. 173104, May 2014.

[8] P. Yuan, K.A. Anselm, C. Hu, H. Nie, C. Lenox, A.L. Holmes, B.G. Streetman, J.C. Cambell and R.J. McIntyre., "A new look at impact ionization-Part II: Gain and noise in short avalanche photodiodes," *IEEE Trans. Electron Devices*, vol. 46, no. 8, pp. 1632–1639, Aug. 1999.

[9] A. H. You, L. C. Low, and P. L. Cheang, "Avalanche Multiplication and Excess Noise Factor of Heterojunction Avalanche Photodiodes," in *2006 IEEE International Conference on Semiconductor Electronics*, Kuala Lumpur, Malaysia, 2006, pp. 324–328.

[10] Y. Taur and T. H. Ning, *Fundamentals of modern VLSI devices*, 2. [rev.] ed., first paperback ed. Cambridge: Cambridge Univ. Press, 2013.

[11] S. M. Sze and K. K. Ng, *Physics of semiconductor devices*, 3rd ed. Hoboken, N.J: Wiley-Interscience, 2007.

[12] D. A. Shushakov and V. E. Shubin, "New solid state photomultiplier," presented at the Photonics West '95, San Jose, CA, United States, 1995, p. 544.

[13] "Analysis and Simulation of Semiconductor Devices | S. Selberherr | Springer." [Online]. Available: https://www.springer.com/us/book/9783709187548. [Accessed: 19-Feb-2019].

[14] M. A. Saleh, M. M. Hayat, P. P. Sotirelis, A. L. Holmes, J. C. Campbell, B. E. A. Saleh

and M. C. Teich, “Impact-ionization and noise characteristics of thin III-V avalanche photodiodes,” *IEEE Trans. Electron Devices*, vol. 48, no. 12, pp. 2722–2731, Dec. 2001.

[15] R. Van Overstraeten and H. De Man, “Measurement of the ionization rates in diffused silicon p-n junctions,” *Solid-State Electronics*, vol. 13, no. 5, pp. 583–608, May 1970.

[16] A. Tosi, S. Cova, F. Zappa, M. Itzler, and R. Ben-Michael, “InGaAs/InP Single Photon Avalanche Diode Design and Characterization,” in *2006 European Solid-State Device Research Conference*, Montreux, Switzerland, 2006, pp. 335–338.

[17] M. A. Itzler, X. Jiang, M. Entwistle, K. Slomkowski, A. Tosi, F. Acerbi, F. Zappa and S. Cova, “Advances in InGaAsP-based avalanche diode single photon detectors,” *Journal of Modern Optics*, vol. 58, no. 3–4, pp. 174–200, Feb. 2011.

[18] S. Pellegrini, R. E. Warburton, L. J. J. Tan, J. S. Ng, A. B. Krysa, K. Groom, J. P. R. David, S. Cova, M. J. Robertson and G. S. Buller, “Design and Performance of an InGaAs–InP Single-Photon Avalanche Diode Detector,” *IEEE J. Quantum Electron.*, vol. 42, no. 4, pp. 397–403, Apr. 2006.

[19] D. Renker, “Geiger-mode avalanche photodiodes, history, properties and problems,” *Nuclear Instruments and Methods in Physics Research Section A: Accelerators, Spectrometers, Detectors and Associated Equipment*, vol. 567, no. 1, pp. 48–56, Nov. 2006.

[20] J.C. Campbell, S. Demiguel, F. Ma, A. Beck, X. Guo, S. Wang, X. Zheng, X. Li, J.D. Beck, M.A. Kinch, A. Huntington, L.A. Coldren, J. Decobert and N. Tscherptner, “Correction to ‘Recent Advances in Avalanche Photodiodes,’” *IEEE J. Select. Topics Quantum Electron.*, vol. 10, no. 6, pp. 1446–1447, Nov. 2004.

[21] M. A. Itzler ,R. Ben-Michael,C. -F. Hsu, K. Slomkowski, A. Tosi, S. Cova, F. Zappa and R. Ispasoiu, “Single photon avalanche diodes (SPADs) for 1.5 μm photon counting applications,” *Journal of Modern Optics*, vol. 54, no. 2–3, pp. 283–304, Jan. 2007.

[22] Y.H. Liu, L. Yan, A. Zhang, D. Hall, I. A. Niaz, Y. Zhou, L. J. Sham and Y-H. Lo, “Cycling excitation process: An ultra efficient and quiet signal amplification mechanism in semiconductor,” *Appl. Phys. Lett.*, vol. 107, no. 5, p. 053505, Aug. 2015.

[23] L. Yan, Y. Yu, A. Zhang, D. Hall, I. A. Niaz, M.A.R. Miah, Y. Liu, Y. Lo, “An amorphous silicon photodiode with 2 THz gain-bandwidth product based on cycling excitation process,” *Appl. Phys. Lett.*, vol. 111, no. 10, p. 101104, Sep. 2017.

Chapter 2

Demonstration of Cycling Excitation Process

Chapter 2 will describe a new carrier amplification mechanism in heavily doped, partially compensated silicon p-n junction devices. Physical mechanism of this process along with experimental results will be presented. Then, first principle calculated results of the underlying physical process will be discussed.

2.1 Introduction to Cycling Excitation Process (CEP)

Cycling excitation process (CEP) is a recently discovered internal carrier multiplication process that occurs at much lower bias (i.e., 3 V bias versus 30–200 V bias for APDs) than impact ionization and favors room temperature over cryogenic temperature in heavily doped and compensated silicon p-n junctions [1]–[3]. The main physical processes involved in this mechanism are auger excitation process and phonon absorption/field assisted tunneling.

2.1.1 Physical Mechanism

CEP involves highly counter doped p-n junction which creates localized states. Whereas conventional impact ionization involves extended states, or traveling Bloch waves, CEP uses both extended and localized states. Hence, the localization of states in counter doped materials relax the requirement of momentum conservation for the occurrence of carrier excitation to the mobile band.

The process starts with an optical excitation which creates electron-hole pair. If one of the charged carriers gains sufficient kinetic energy after crossing the junction, then it can create

another e-h pair. The key difference with the conventional impact ionization is that this creation of e-h pair doesn't necessarily need band to band transition. Rather due to highly co-doping both p side and n side of the junctions, localized states are created (to be shown from first principle calculation in section 2.3). For indirect bandgap detectors such as silicon, momentum conservation requires that a particle of suitable k-vector be involved in the transition to account for the difference in k-space between the conduction band minimum and valence band maximum. In the case of extended states, only one k-vector can meet this criterion. For localized states, however, the imprecision in required k-vector makes this criterion much more easily satisfied, as shown in Fig. 2.1.

Thus, localized states relax the k-selection rule (momentum conservation) [1], [4], [5], and enhances the probability of new e-h pair generation via collision between the energetic carrier and the localized electrons (holes).

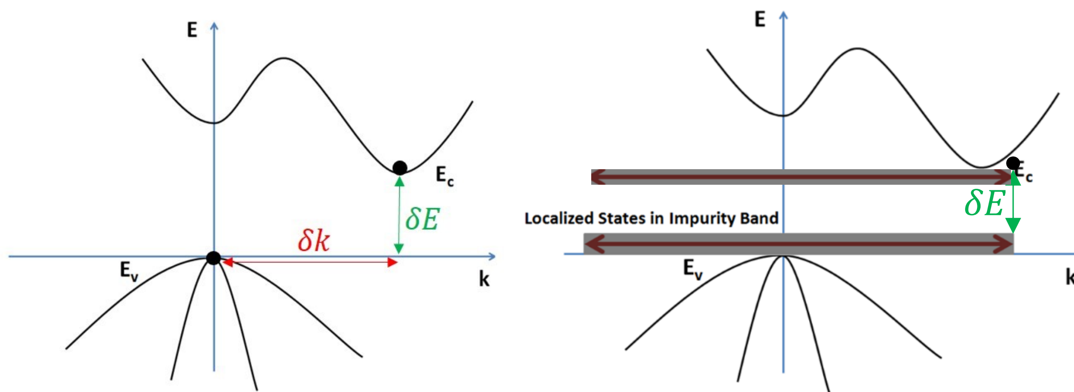

Figure 2.1: Energy versus momentum diagram for a band-to-band transition in an indirect bandgap semiconductor with and without localized states involved.

As an illustration, consider an electron accelerated by a potential drop in crossing the p-n junction towards the n region (Fig. 2.2(a)). In the heavily compensated n region, the photo-

generated electron acquires sufficient energy for an Auger process to excite an electron across the band gap from the acceptor. The hole left behind is susceptible to being filled by a valence band electron via phonon absorption (Fig. 2.2(b)). The Auger process is more probable from the acceptor than from the valence band because of the former's localized wave function. Furthermore, the band hole thus created, in crossing back the p-n junction, has a probability of a similar Auger excitation to produce an additional electron-hole pair from the compensating donors in the p-region (Figs. 2.2(c)–2.2(d)). The cycling process produces a series of events with geometrically decreasing probabilities, enhancing the photocurrent beyond the single electron-hole pair created by the original photon.

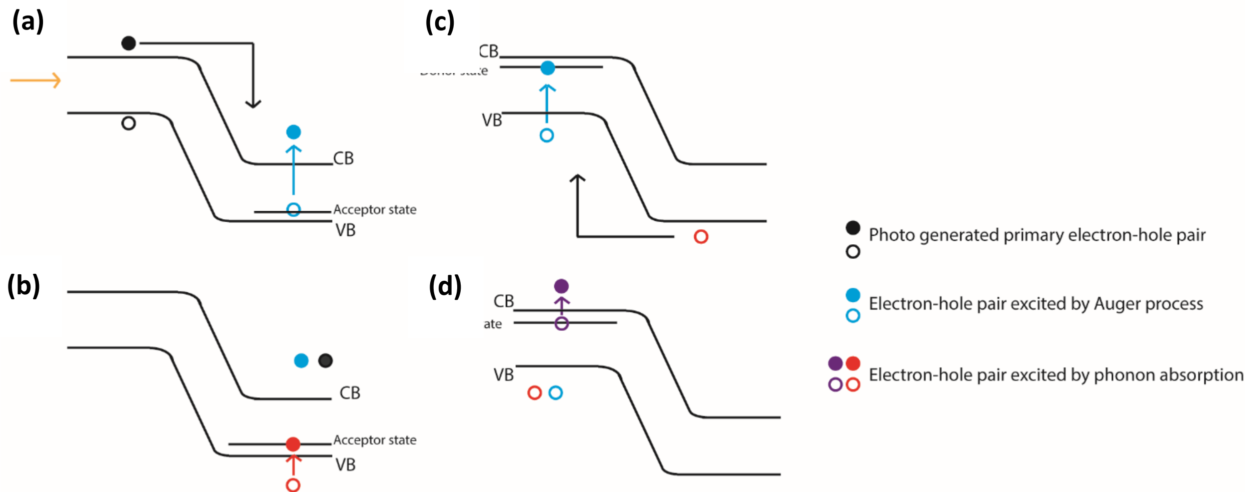

Figure 2.2: Illustration of the cycling excitation process. The processes from (a) to (d) take place in sequence: (a) Primary photo generated electron excites an electron from a compensating acceptor in the n-region to the conduction band, (b) followed by a phonon-absorption process to produce a hole carrier. (c) The Auger-plus-phonon created hole may similarly add an electron-hole pair from a compensating donor in the p-region. (d) the electron carrier is created by another phonon absorption.

Under the premise of ionization of a compensating impurity as essential for generating additional carriers, the gain is regulated by the state and dynamics of phonons [6]–[8], thus providing a feedback mechanism to stabilize the device and suppress the device noise. Should the

instantaneous gain be stronger than the mean value due to the stochastic nature of the amplification process, the limited number of local population of phonons provides a self-limiting mechanism to suppress the magnitude of gain fluctuation, thus reducing the noise.

The necessity of phonon assistance in the cycling means that increasing reverse bias would provide a greater number of high energy carriers outstripping the available phonons, thus providing a limiting mechanism for the saturation of the gain. For the cycling excitation process, phonons not only play an important role in producing the gain but also in regulating the instantaneous gain fluctuations to yield excellent noise characteristics

2.1.2 Experimental Results

The device structure is grown by the organometallic chemical vapor deposition (OMCVD) technique to achieve precise control of the doping profile and layer thickness [1], [2]. Although the device shows a rather typical p-n junction current-voltage characteristics in the dark condition, its photocurrent increases markedly with the reverse bias voltage, in sharp contrast with a standard p-n junction photodiode where the photoresponse remains nearly constant. At a reverse bias voltage as low as 3 V, the photoresponse gain reaches over 4000, as shown in Fig. 2.3(a). By contrast, for impact ionization to produce a gain of around 10, the p-n junction needs to be biased to over 20 V according to simulation (Silvaco software). This result demonstrates the superior characteristics of the CEP over the traditional avalanche multiplication process initiated by impact ionization. Notably, the gain of the CEP device decreases with increasing input optical power represented by the primary photocurrent in Fig. 2.3(a). The temperature dependence of gain shows a gain increase as the temperature increases (Fig. 2.3(b)). These results strongly suggest that phonons play significant roles in the CEP effect. The higher performance of the device with

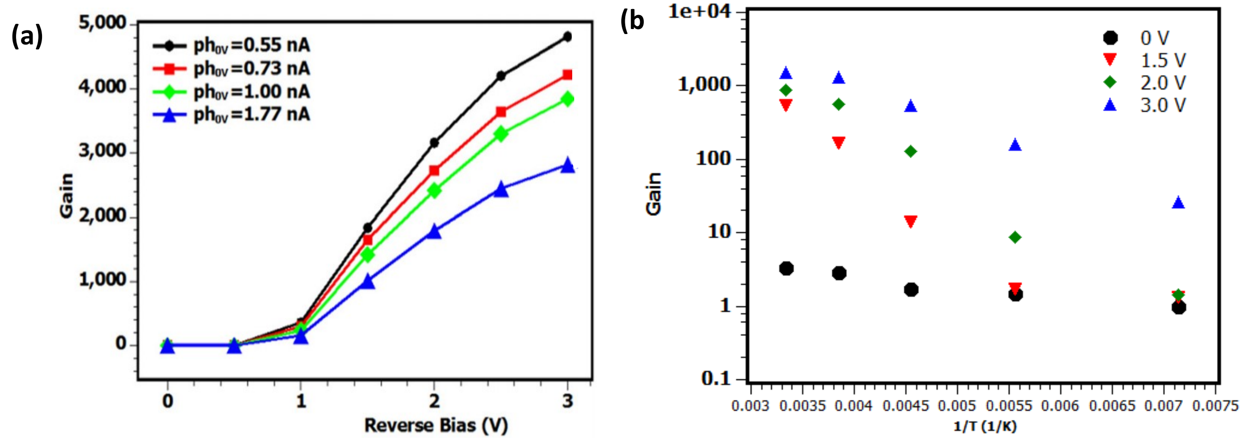

Figure 2.3: Bias, input light intensity, and temperature dependence of gain. (a) Bias and input light intensity dependence of gain. The illumination (635 nm) light power is represented by the primary photocurrent at zero volt. (b) Temperature dependence of gain under 635 nm illumination in Arrhenius plots.

increasing temperature suggests that phonons, actually assist in the amplification process rather than hinder it via phonon scattering, as discussed next.

In order for CEP to continue at maximum efficiency, the essential elements, namely, localized donor states, localized acceptor states, hot carriers, and phonon density, must have comparable density in the CEP region; missing any one of these elements creates a bottleneck. The CEP junction is designed to have a very large donor and acceptor density. Additionally, for large input photon number, the hot carrier density will also be high. The phonon density is the one element that is not straightforward to control. For large number of hot carriers, there can be a deficiency of phonons in the CEP region, i.e. there are not enough phonons to match to localized impurity states.

To summarize, a heavily doped and heavily compensated silicon p-n junction device has been demonstrated to produce the cycling excitation process to amplify signals with unprecedented efficiency. The low bias of the device, the simple and CMOS compatible fabrication process, the favorable temperature characteristics, and the ultralow noise of the amplification process make the

CEP effect a highly attractive, especially promising physical mechanism for a large family of devices beyond photodiodes.

2.2 First Principle Modeling of Localization

The high efficiency of CEP gain mechanism lies in the availability of localized donor and acceptor states. This localization relaxes k-selection rule and enhances impact ionization probability. In this section, we demonstrate localization of carriers from quantum mechanical (QM) calculation in highly co-doped system.

To calculate the charge distribution, interaction with neighboring electrons needs to be considered. So, to get the true electronic properties (band diagram, density of states etc.), a many body problem has to be solved. To this end, density functional theory (DFT) has been the most efficient computational technique for solving many body problems to investigate the structural, magnetic and electronic properties of molecules, materials and defects [9].

2.2.1 A Brief Introduction to Density Functional Theory (DFT)

The quantum mechanical wavefunction contains all the information about a system. For some systems (e.g. 2-D square potential or Hydrogen atom), Schrödinger equation can be analytically solved to calculate the wavefunction. However, it becomes computationally almost impossible to solve the same for a N-body system.

Schrödinger equation for a many body system can be written as:

$$\hat{H}\psi = E\psi \ldots\ldots\ldots (2.1)$$

Where, $\hat{H} = \hat{T}_N + \hat{V}_{NN} + \hat{T}_{ee} + \hat{V}_{Ne} + \hat{V}_{ee}$

Here

$\hat{T}_N$=Kinetic energy of the nuclei

$\hat{V}_{NN}$=Coulomb interactions between nuclei

$\hat{T}_{ee}$=Kinetic energy of the electrons

$\hat{V}_{Ne}$=Coulomb interactions between nuclei and electrons

$\hat{V}_{ee}$=Coulomb interactions between electrons

The many body Hamiltonian $(\hat{H})$ is a coupled electronic and nuclear problem. To reduce the complexity of the many body problem, Born-Oppenheimer proposed an approximation of separating the electronic problem from the nuclear problem [10]. Since, nuclei are heavy and slow compared to electrons, hence, motion of electrons can be deemed to be instantaneous. So, the kinetic energy of nuclei can be neglected and it is valid to assume that electrons will see external static potential of nuclei. This simplifies the Hamiltonian of (2.1) into

$$\hat{H}_e = \hat{T}_{ee} + \hat{V}_{ee} + \hat{V}_{ext} \dots \dots (2.2)$$

Even after this simplification, the problem requires to solve 3N variables (the coordinates of all N atoms in the system).

2.2.2 Kohn-Sham Equation

Hohenberg and Kohn proposed a theorem using electron density [11]. Their theorem states that the ground state property of a system can be determined by the density. A many electron system's total ground state energy is a functional (function of a function) of the density. If the electron density functional is known, then the total energy of the system will be known. Since,

electron density is a function of 3 variables (x,y,z), use of electron density would significantly reduce the computational complexity.

From Hohenberg-Kohn theorem, Kohn and Sham proposed a computationally feasible scheme by mapping the system of interacting particles onto a fictitious system of non-interacting particles in an effective potential, that reproduces the same electron density as the many-body problem of interest [9].

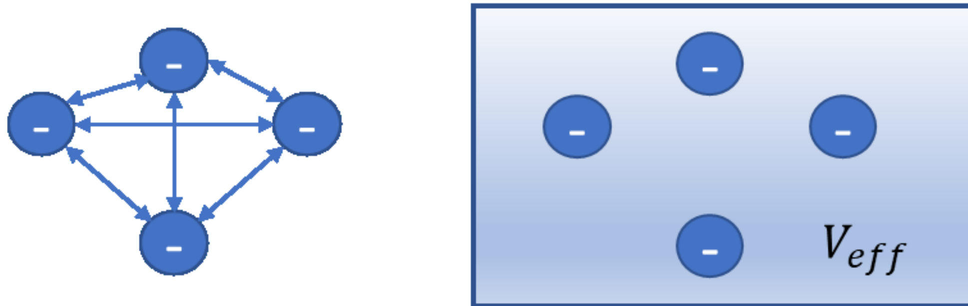

Figure 2.4: Interacting system is mapped to a non-interacting fictitious system

With this simplification, the Hamiltonian can be written as a sum of effective one particle Hamiltonians, $\hat{h}_e$

$$\hat{H}_e = \sum_{i=1}^{N} \hat{h}_e = \sum_{i=1}^{N} \hat{t}_{ee} + \sum_{i=1}^{N} \hat{v}_{eff} \dots\dots\dots (2.3)$$

The central quantities obtained in DFT are the total energy and the electron density. The basic iterative scheme of DFT calculation is given in the following flow chart of Fig. 2.5.

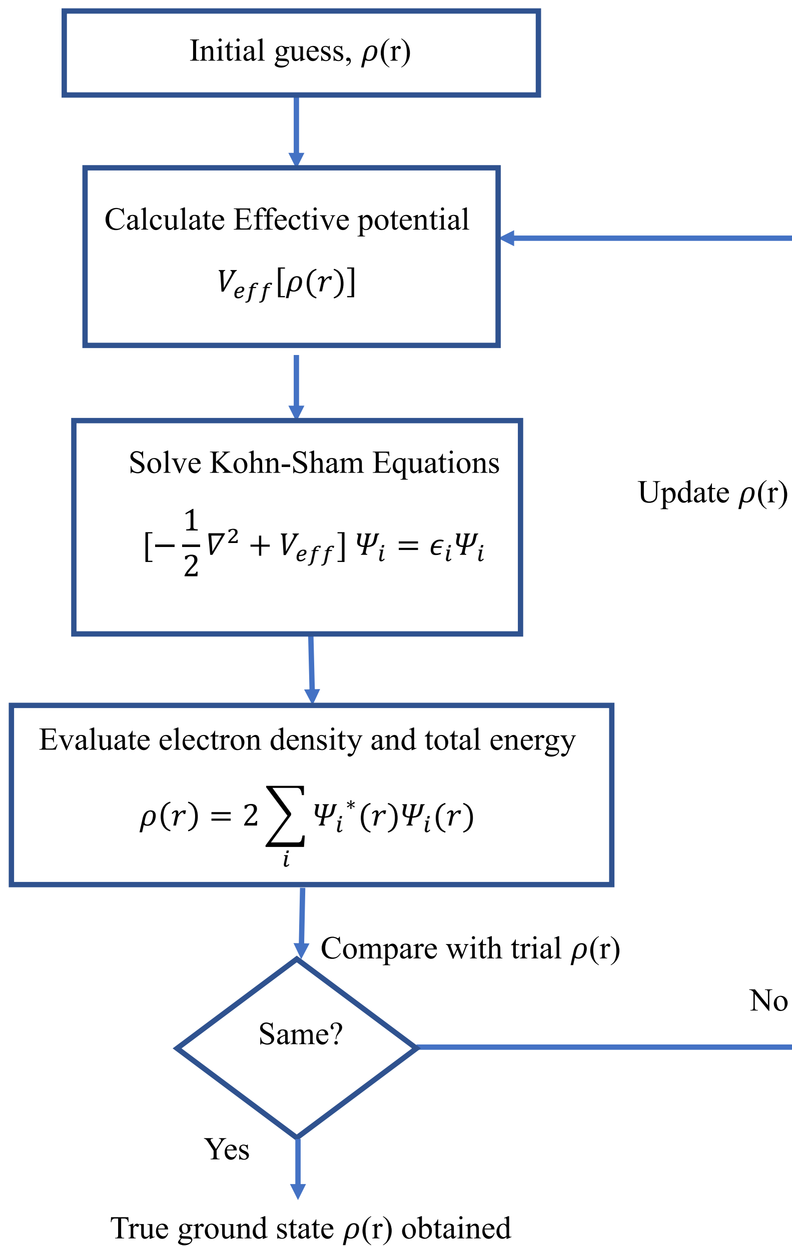

Figure 2.5: Self-consistent scheme of density functional theory

2.3 Simulation Results from DFT Calculation

Our DFT calculations were performed for both bulk silicon and heavily compensated doped silicon. We used plane wave basis set based simulation package, Quantum Espresso [12]. Due to complexity and computational cost, we used 54 atom unit cell for both Bulk Silicon (54 atom Si) and boron-phosphorous (BP) doped Silicon (52 atom Silicon, 1 B atom, 1 P atom) both with a lattice constant of $3a$ where $a = 5.43A^0$. Gradient Gradual Approximation (GGA) functional was used as exchange correlational functional [13]. Both k-point sampling and the plane wave basis set were checked for convergence, with a cutoff of 50 eV and k-point grid of $5\times 5 \times 5$ was found to be sufficient for 54 atom unit cell. For all atoms, ultrasoft pseudopotential found in the Quantum Espresso database was used in the calculations. Boron and phosphorus are placed as a substitutional impurity such that their relative distances is $2\sqrt{3}a$.

2.3.1 Electronic Band Structure and Density of States

At first, the band diagram for the bulk silicon was calculated using Quantum Espresso package. The computed band diagram is shown in Fig. 2.6(a). From the figure, it is evident that the resulted bandgap is 0.58 eV which is almost half of the known band gap of Silicon of 1.12 eV. This is a well-known problem of DFT calculation. The GGA functional can't compensate for the errors originating from QM interaction. That results in underestimation of bandgap [14].

As our supercell is three times larger than Face centered cubic (FCC) Si Primitive Cell (PC), so supercell Brillouin zone is shrunk and results in band folding. The resultant band diagram includes bands that cross the first BZ and reenters from opposite side as well as some projection points from other symmetry directions. The unfolding has been performed using the BandUp code

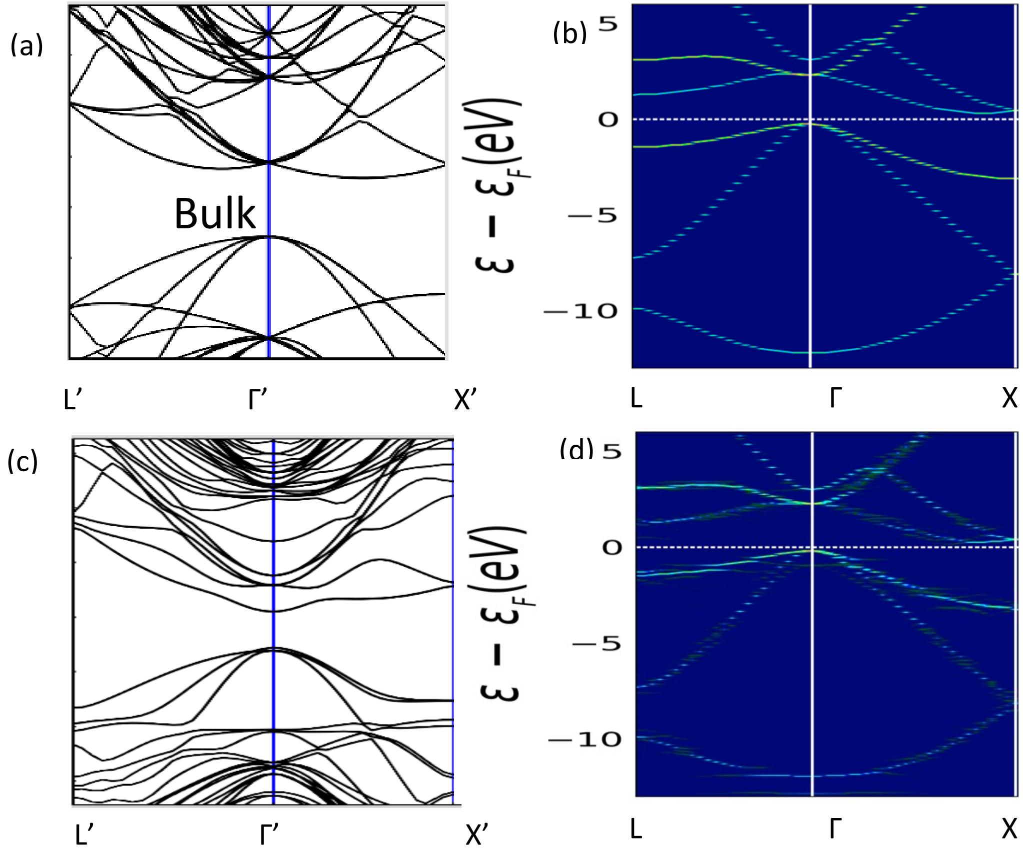

Figure 2.6: (a) Band Diagram for 54 atoms Si supercell (L’, Γ’, X’ denotes supercell Brillouin zone edge), (b)Band Diagram after unfolding (L, Γ, X denotes primitive cell Brillouin Zone edge), (c) BP pair doped 54 atoms Supercell band diagram, (d) Band Diagram of BP pair doped Si after unfolding (distortions at different bands denotes presence of impurities)

[15], [16]. The unfolded band diagram is shown in Fig. 2.6(b). It is clearly seen that the shape of the band diagram is that of silicon band diagram found in literature.

The band diagram of BP doped Silicon was computed to find the impact of them in the band properties. The resulted band diagram is shown in Fig. 2.6(c). and the unfolded band diagram is shown in Fig. 2.6(d). Though in Fig. 2.6(c). the band diagram seems to be direct as the band minimum above the band gap is found in Γ’ point, but it is clear from the unfolded diagram that this point is a mirror symmetry of the $\frac{2}{3}^{\text{rd}}$ point on Γ-X direction introduced due to phosphorus

impurity. As it is a fully compensated structure, change in Fermi level is negligible with respect to the bulk structure, but we see the impact of broken translational symmetry and p-n doping on the unfolded band diagram in Fig. 2.6(d). The density of states is plotted in Fig 2.7 which shows the presence of states inside band-gap in case of quasi disordered Si by BP doping.

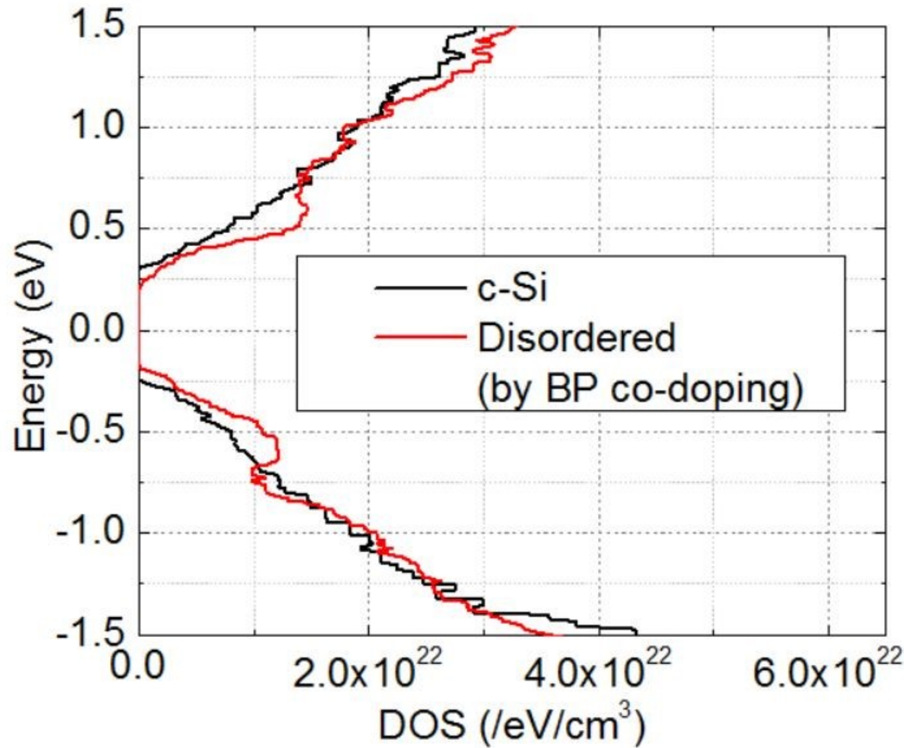

Figure 2.7: Density of states comparison for bulk and disordered silicon

2.3.2 Localization of Wavefunction

As we had seen the impact of BP doping on the band diagram and density of states of Silicon, we had further investigated our claim of localization due to high doping in compensated Silicon. The reason is that when we substitutional dope with Boron, we expect in the band diagram to have localized band around valence band maxima. However, Windl's work shows that boron interstitial complex is needed to see the distortion in valence band from boron doping [17]. On the

other hand, phosphorus doping distorts the band diagram near conduction band minima from regular crystalline structure.

The direction and relative position of the Silicon, Boron and Phosphorous atom in the $[\bar{1}11]$ direction is shown in Fig 2.8. For bulk silicon case, all the atoms are silicon. We have plotted the charge density in the $[\bar{1}11]$ direction for the valence band maxima for both bulk silicon and disordered silicon at the Γ' point. The positions of the atoms in this direction are shown in Fig 2.8.

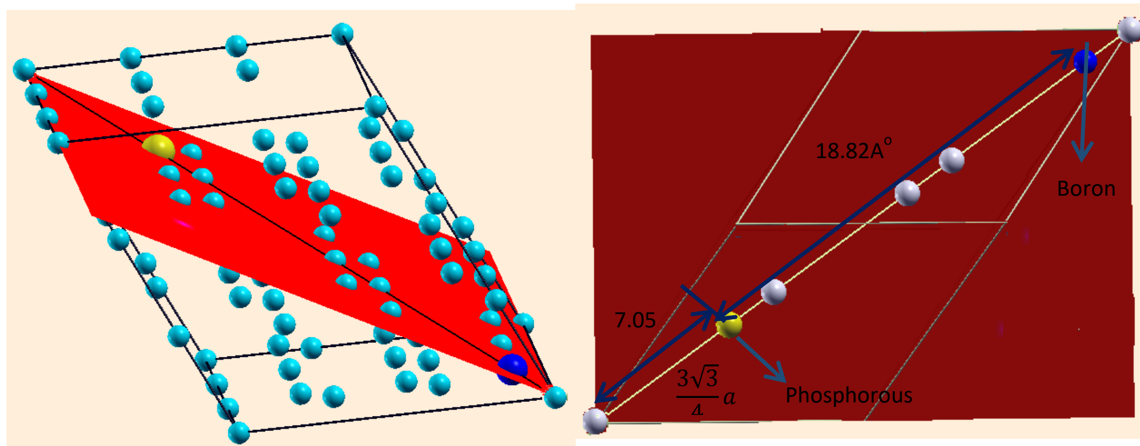

Figure 2.8: Position of Phosphorous and Boron atoms along $[\bar{1}11]$ direction (In the case of bulk Si, all atoms are Si)

Fig. 2.9(a) shows the strong localization around boron atom whereas the periodicity in the charge density is same in bulk silicon. Figs 2.9(b) and 2.9(c) show the corresponding k point used in the plots. Similarly, charge density is plotted for the conduction band minima for both cells. Localization around the phosphorus atom is clearly seen Fig 2.9(d) for BP pair Silicon, whereas we see periodic Bloch wave like behavior in bulk silicon. Figs 2.9(e) and 2.9(f) indicate the k point used for plotting. So, these results demonstrate localized band around the impurity which in turn supports k relaxation and efficient secondary electron generation process.

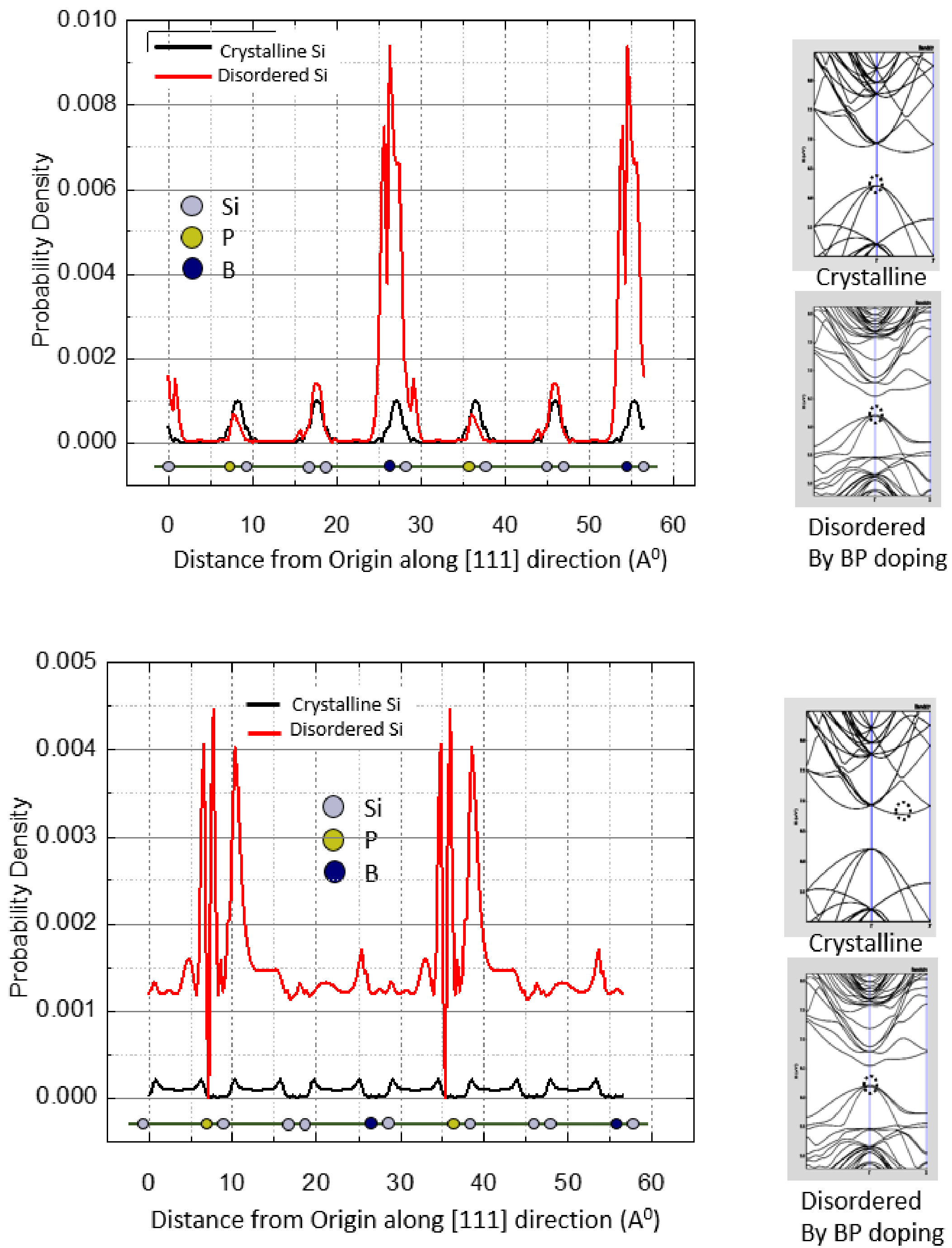

Figure 2.9: (a) Localization of probability density around Boron atom at valence band maxima, (b) corresponding k point bulk Si band diagram and (c) corresponding k point at disordered Si (by BP doping) band diagram. (d) Localization of probability density around Phosphorous atom at lowest energy band above band gap, (e) and (f) corresponding k points in bulk Si and disordered Si respectively.

2.4 Conclusion

This chapter introduced Cycling Excitation Processes (CEP) as an alternative internal signal amplification mechanism to impact ionization and demonstrated the key feature of this process from first principle modeling. CEP uses two key physical processes of Auger excitation and phonon absorption. A CEP detector using heavily doped and partially compensated silicon with a gain of ~4000 at 3V bias at 635 nm illumination was achieved. Phonon bottleneck provides negative feedback resulting in higher gain with lower input optical power, gain saturation at operation bias, and higher gain at room temperature operation.

The key difference with conventional impact ionization process lies in the participation of localized states inside bandgap in Auger excitation process in highly co-doped materials to relax the k-selection rule of momentum conservation. Density functional theory calculation proves the existence of localized states and localization of carriers is observed from charge density profile.

This chapter, in part, is a reprint of material as it appears in the following publications:

Y. H. Liu, L. Yan, A. C. Zhang, D. Hall, I. A. Niaz, Y. Zhou, L. J. Sham, and Y. H. Lo, "Cycling excitation process: An ultra efficient and quiet signal amplification mechanism in semiconductor," Applied Physics Letters 107, 053505 (2015)

M. A. R. Miah*, I.A. Niaz*, Y. H. Liu, D. Hall, and Y. H. Lo, "A high-efficiency low-noise signal amplification mechanism for photodetectors," Proc. SPIE 10108, Silicon Photonics XII, 101080X, 20 February 2017; (* →co-first authors).

The dissertation author was a coauthor/ primary author of these papers.

References:

[1] Y. Zhou, Y.-H. Liu, S. N. Rahman, D. Hall, L. J. Sham, and Y.-H. Lo, "Discovery of a photoresponse amplification mechanism in compensated PN junctions," *Applied Physics Letters*, vol. 106, no. 3, p. 031103, Jan. 2015.

[2] Y.H. Liu, L. Yan, A. Zhang, D. Hall, I. A. Niaz, Y. Zhou, L. J. Sham and Y-H. Lo, "Cycling excitation process: An ultra efficient and quiet signal amplification mechanism in semiconductor," *Appl. Phys. Lett.*, vol. 107, no. 5, p. 053505, Aug. 2015.

[3] L. Yan, Y. Yu, A. Zhang, D. Hall, I. A. Niaz, M.A.R. Miah, Y. Liu, Y-H. Lo,, "An amorphous silicon photodiode with 2 THz gain-bandwidth product based on cycling excitation process," *Appl. Phys. Lett.*, vol. 111, no. 10, p. 101104, Sep. 2017.

[4] P. J. Dean, J. R. Haynes, and W. F. Flood, "New Radiative Recombination Processes Involving Neutral Donors and Acceptors in Silicon and Germanium," *Physical Review*, vol. 161, no. 3, pp. 711–729, Sep. 1967.

[5] S. M. Sze and K. K. Ng, *Physics of semiconductor devices*, 3rd ed. Hoboken, N.J: Wiley-Interscience, 2007.

[6] V. V. Paranjape and B. V. Paranjape, "Phonon Excitation by Electric Field in Semiconductors," *Physical Review*, vol. 166, no. 3, pp. 757–762, Feb. 1968.

[7] G. Paulavičius, V. V. Mitin, and N. A. Bannov, "Coupled electron and nonequilibrium optical phonon transport in a GaAs quantum well," *Journal of Applied Physics*, vol. 82, no. 11, pp. 5580–5588, Dec. 1997.

[8] J. Zou and A. Balandin, "Phonon heat conduction in a semiconductor nanowire," *Journal of Applied Physics*, vol. 89, no. 5, pp. 2932–2938, Mar. 2001.

[9] W. Kohn and L. J. Sham, "Self-Consistent Equations Including Exchange and Correlation Effects," *Physical Review*, vol. 140, no. 4A, pp. A1133–A1138, Nov. 1965.

[10] M. Born and R. Oppenheimer, "Zur Quantentheorie der Molekeln," *Annalen der Physik*, vol. 389, no. 20, pp. 457–484, 1927.

[11] P. Hohenberg and W. Kohn, "Inhomogeneous Electron Gas," *Physical Review*, vol. 136, no. 3B, pp. B864–B871, Nov. 1964.

[12] P. Giannozzi1, S. Baroni1, N. Bonini, M. Calandra, R. Car, C. Cavazzoni, D. Ceresoli, G. L. Chiarotti, M. Cococcioni, I. Dabo, A. D. Corso, S. D. Gironcoli1, S. Fabris, G. Fratesi, R. Gebauer, U. Gerstmann, C. Gougoussis, A. Kokalj, M. Lazzeri, L. Martin-Samos, N. Marzari, F. Mauri, R. Mazzarello, S. Paolini, A. Pasquarello, L. Paulatto, C. Sbraccia, S. Scandolo, G. Sclauzero, A. P. Seitsonen, A. Smogunov, P. Umari and R. M. Wentzcovitch, "QUANTUM ESPRESSO: a modular and open-source software project for quantum simulations of materials," *Journal of Physics: Condensed Matter*, vol. 21, no. 39, p. 395502, Sep. 2009.

[13] P. J. Hasnip, K. Refson, M. I. J. Probert, J. R. Yates, S. J. Clark, and C. J. Pickard, “Density functional theory in the solid state,” *Philosophical Transactions of the Royal Society A: Mathematical, Physical and Engineering Sciences*, vol. 372, no. 2011, p. 20130270, Mar. 2014.

[14] V. Sahni, J. Gruenebaum, and J. P. Perdew, “Study of the density-gradient expansion for the exchange energy,” *Physical Review B*, vol. 26, no. 8, pp. 4371–4377, Oct. 1982.

[15] P. V. C. Medeiros, S. Stafström, and J. Björk, “Effects of extrinsic and intrinsic perturbations on the electronic structure of graphene: Retaining an effective primitive cell band structure by band unfolding,” *Physical Review B*, vol. 89, no. 4, Jan. 2014.

[16] P. V. C. Medeiros, S. S. Tsirkin, S. Stafström, and J. Björk, “Unfolding spinor wave functions and expectation values of general operators: Introducing the unfolding-density operator,” *Physical Review B*, vol. 91, no. 4, Jan. 2015.

[17] W. Windl, X-Y. Liu and M. P. Masquelier, “First-Principles Modeling of Boron Clustering in Silicon”, *Physica Status Solidi B*, vol. 226, no. 1, May. 2001.

Chapter 3

Carrier Multiplication in Disordered Materials

Chapter 3 describes highly efficient carrier multiplication in disordered materials such as amorphous silicon. High gain at low bias, lower dark current are demonstrated. Physics based model along with numerical simulations are presented to decouple the unequivocal inherent gain in disordered materials from any other non-ideal effects emanating from metal-semiconductor interface.

3.1 Demonstration of Carrier Multiplication in Disordered Materials

3.1.1 Motivation

On the premise that CEP effect uses Auger excitation involving localized states to relax the k-selection rule, the design of the previous CEP photodetector consists of a heavily-doped and heavily compensated p-n junction as discussed in chapter 2 [1], [2]. Having these compensating impurities as localized states to support the CEP process, efficient amplification of primary photocurrent has been achieved under low bias [2], [3]. However, the delicate balance in doping compensation presents significant challenges in dark current and process compatibility. Furthermore, the gain-bandwidth product and the required material properties to produce the CEP effect remain unclear. Earlier experimental results [4] and density functional theory calculations

[5] have suggested that high density of localized states and strong electron-phonon coupling are two properties that favor the CEP effect. We recognize that many disordered semiconductors possess such properties. In fact, one can treat the heavily-doped, heavily compensated p-n junction as a method to turn crystalline silicon into a quasi-disordered material. To this end, many of the low cost, easy-to-process disordered materials can be used as the primary gain medium, which can be formed on many kinds of rigid and flexible substrates.

3.1.2 Design of Amorphous Silicon (a-Si) Detector

Following this rationale, we infer that amorphous silicon (a-Si), as a disordered material, can present CEP effect too. Because of its bonding and topological disorder, amorphous silicon has long band tails of localized states [6] which have strong electron phonon interaction [7], [8] as well. However, there are also deep states within its bandgap due to structural defects and dangling bonds. Although the deep states are also localized states, they are too deep to be excited by phonons and rely on field enhanced direct/indirect tunneling to move the localized carriers to the mobile bands. Therefore, the amorphous silicon was treated with hydrogen plasma to passivate the dangling bonds of Si with H atoms to control the density of those deep states. A small percentage of carbon (~5%) was also introduced into the hydrogenated amorphous silicon (a-Si:H) to increase the level of disorder [9] and to tailor the phonon energy and strength of electron-phonon coupling [10]. With this approach, our group fabricated devices with a 40nm Carbon-doped (C-doped) a-Si:H CEP layer sandwiched between a top transparent contact and an n^+-Si substrate. Indium Tin Oxide (ITO) was used for the top contact as a transparent electrode.

3.1.3 Experimental Results

A schematic diagram of the device cross-section is shown in Fig. 3.1(a). Fig. 3.1(b) shows the device dark current for various designs of CEP active gain layer. The CEP device with C-doped a-Si:H shows excellent dark current. The compensated silicon p-n junction devices have the highest dark current, mostly due to high tunneling current. The a-Si:H devices show much lower dark current because of their higher bandgap which suppresses tunneling. Doping the a-Si:H with ~5% carbon further suppresses the dark current by more than three orders of magnitude. At -3V bias, the dark current density of the 5% carbon-doped a-Si:H device is about 22μA/cm^2.

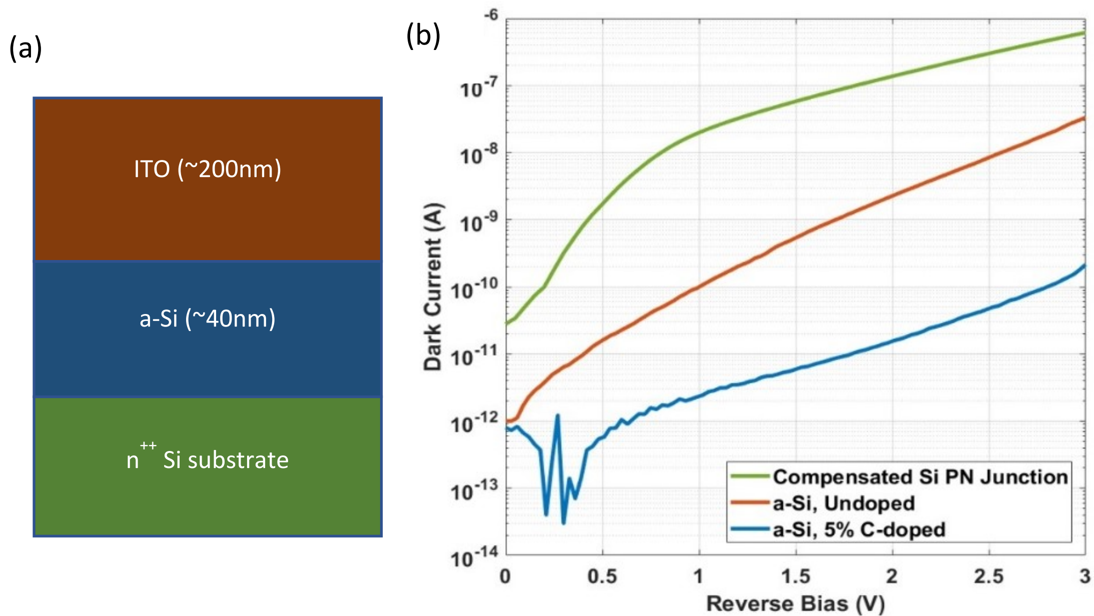

Figure 3.1: (a) Schematic diagram of a-Si:H CEP device structure with the material and function of each layer. The photodiode operates under reverse bias. (b) Dark current versus reverse bias voltage plots for a CEP photodiode made of a compensated silicon p/n junction, a 40nm undoped a-Si:H layer, and a 40nm 5% C-doped a-Si:H layer. All three devices have the same structure and size.

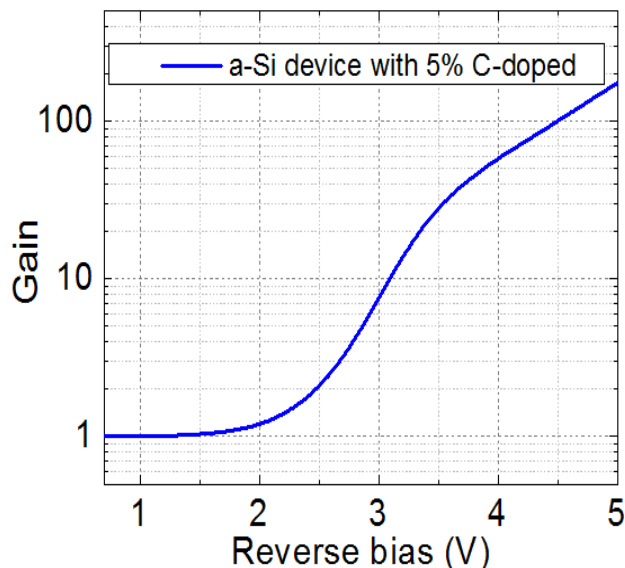

Figure 3.2: DC photo-current gain of a carbon-doped a-Si:H CEP photodiode. Photodiode has a 30µm diameter photosensitive area.

To probe the intrinsic properties of the CEP effect in the amorphous silicon layer, the device was illuminated with 635nm laser wavelength, because of its shallow absorption depth (<100nm). This causes the initial hot electron injection from n+ substrate and minimizes masking of the intrinsic properties of CEP process within the (C-doped) a-Si:H layer. The CEP photocurrent gain of a-Si:H device is shown in Fig. 3.2. The gain is defined as the ratio of photocurrent under a given bias voltage to photocurrent under low-bias where the photocurrent level is relatively flat before the field crosses carrier multiplication threshold value.

3.2 Modeling of Gain Mechanisms in Amorphous Silicon

To unveil the true gain mechanism in a-Si, we performed theoretical modeling and numerical analysis along with experimental data at different frequencies. We show evidence of highly effective carrier multiplication process within a-Si as the primary gain mechanism, especially at high frequency. We also show presence of trap-induced junction modulation at much lower frequency.

In this section, we show from physical modeling and experimental results the existence of highly efficient carrier multiplication in thin a-Si (<50nm) and the existence of a significant difference in the carrier multiplication efficiency for devices with different a-Si thickness. When the a-Si thickness increases, the carrier multiplication efficiency drops. In addition, due to the dynamics of the donor and acceptor traps in a-Si, the tentatively trapped carriers can modulate the effective barrier height and thickness for electron tunneling from the electrodes, producing another path for photocurrent amplification which we refer to the effect of junction modulation. We show that DC measurement of photocurrent cannot distinguish gains from carrier multiplication or junction modulation. However, the contributions of both mechanisms can be clearly separated with frequency dependent photocurrent gain because the junction modulation gain due to trap dynamics rolls off quickly at KHz range while the carrier multiplication mechanism has a much higher frequency response.

3.2.1 Numerical Modeling

Here, we describe the numerical model to study the gain mechanism in a-Si. The device structure consists of a thin layer of a-Si (~40nm) as both the light absorption layer and the gain medium that is sandwiched between Indium Tin Oxide (ITO) and degenerately doped n-type (n++) crystalline Si (c-Si). Due to the difference between ITO work function and electron affinity of n-Si, a built-in field exists to produce a photocurrent under zero bias.

To model carrier transport in our structure, we solved the Poisson's equation (3.1) and the carrier continuity equation (3.2) coupled with the current density equation (3.3), as described in Silvaco [11]. The a-Si layer is undoped but contains charge in the ionized donor and acceptor states due to material defects.

$$\frac{\partial^2 \phi(x,t)}{\partial x^2} = \frac{-q}{\epsilon}[p - n + N_{tD}^+(x,t) - N_{tA}^-(x,t)] \quad (3.1)$$

$$\frac{\partial n(x,t)}{\partial t} = \frac{1}{q}\nabla J_n(x,t) + G(x,t) - R_n(x,t) \qquad (3.2a)$$

$$\frac{\partial p(x,t)}{\partial t} = -\frac{1}{q}\nabla J_p(x,t) + G(x,t) - R_p(x,t) \quad (3.2b)$$

$$J_n(x,t) = qn(x,t)v_n(\mathcal{E}) + qD_n\frac{\partial n(x,t)}{\partial x} \qquad (3.3a)$$

$$J_p(x,t) = qp(x,t)v_p(\mathcal{E}) - qD_p\frac{\partial p(x,t)}{\partial x} \quad (3.3b)$$

In (3.1) and (3.2), n and p are the electron and hole carrier densities and N_{tD}^+ and N_{tA}^- are the densities of ionized donor and acceptor traps. In a-Si, donor type traps are located near or below the intrinsic Fermi level, E_i [12]. An empty donor type trap is charge positive and can emit a hole (or capture an electron), and an occupied donor type trap is charge neutral and can capture a hole (or emit an electron). As for acceptor type traps, they are located above E_i [12]. These acceptor type traps are neutral when empty and negatively charged when filled with an electron. In (2a) and (3a), J_n and in (2b) and (3b), J_p are electron and hole current densities respectively, $v_n(v_p)$ is electron (hole) drift velocity, $\mathcal{E}$ is the local electric field, G is the sum of carrier generation by photon absorption, G_{opt} and by carrier multiplication via impact ionization, G_{imp}. R_n (R_p) is the net electron (hole) recombination rate that is equal to the difference between carrier recombination and thermal generation. Drift velocity can be represented by $v_{n,p}(\mathcal{E}) = \mu_{n,p}(\mathcal{E})\mathcal{E}$ with $\mu_{n,p}(\mathcal{E})$ being field-dependent electron (hole) mobility. The electron (hole) velocity reaches its saturation velocity at high field [13].

To incorporate the dynamics of the donor and acceptor type traps, the following equations were employed [14].

$$\frac{\partial N_{tD}^{+}(x,t)}{\partial t} + \left(C_{pD}p(x,t) + C_{nD}n(x,t)\right) N_{tD}^{+}(x,t) + \left(e_{pD} + e_{nD}\right)N_{tD}^{+}(x,t)$$

$$= \frac{p(x,t)}{\tau_{pD}} + e_{nD}N_{tD} \quad (3.4a)$$

$$\frac{\partial N_{tA}^{+}(x,t)}{\partial t} + \left(C_{nA}n(x,t) + C_{pA}p(x,t)\right) N_{tA}^{+}(x,t) + \left(e_{pA} + e_{nA}\right)N_{tA}^{+}(x,t)$$

$$= \frac{n(x,t)}{\tau_{nA}} + e_{pA}N_{tA} \quad (3.4b)$$

In (3.4a), C_{pD} (C_{nD}) is the capture constant of hole (electron) by donor type trap states and e_{pD} (e_{nD}) is emission rate of holes (electrons). Similar terms exist for acceptor type trap states in (3.4b). The time constants are defined as: $C_{pD}N_{tD} = 1/\tau_{pD}$ and $C_{nA}N_{tA} = 1/\tau_{nA}$.

The dynamic trap equations take into account the dynamics of electron (hole) emission and capture by the defect states. The carrier generation rate consists of photogeneration (depends on input light) and impact ionization

$$G = G_{opt} + G_{imp} \qquad (3.5)$$

Here, $G_{opt} = k\frac{P\lambda}{hc}$ where k is light absorption coefficient of the material and P(t) is the input optical power at wavelength λ.

We used local electric field dependent impact ionization model to simulate the carrier multiplication phenomenon [15]. To best fit the experimental results, we had to adjust impact ionization coefficients over the electric field range of interest. The general impact ionization model is described in Eq. (3.6).

$$G_{imp} = \frac{1}{q}\left[\alpha_n|J_n| + \alpha_p|J_p|\right] \quad (3.6)$$

$\alpha_{n,p}$ are the impact ionization coefficients for electrons and holes. In this model, impact ionization coefficients (i.e. number of electron-hole pairs generated by a carrier per unit distance), are given by

$$\alpha_{n,p} = A_{n,p} \exp\left(-\left(\frac{B_{n,p}}{\mathcal{E}}\right)^{\beta_{n,p}}\right) \quad (3.7)$$

Finally, at the boundary, the front ITO was modeled as a Schottky electrode with work function of 4.95eV [16], [17]. Contributions from thermionic emission as in (3.8) and Fowler-Nordheim (FN) tunneling as in (3.9) were employed at Schottky contact interface of ITO and a-Si.

$$J_{therm} = A^* T^2 \exp\left(-\frac{q\varphi_B}{kT}\right)\left(\exp\left(\frac{qV}{kT}\right) - 1\right) \quad (3.8)$$

$$J_{FN} = \frac{q^2}{8\pi h \varphi_B} \mathcal{E}^2 \exp\left(-\frac{8\pi\sqrt{2m_{tunnel}}(\varphi_B)^{3/2}}{3h\mathcal{E}}\right) \quad (3.9)$$

Here φ_B is the Schottky barrier, A^* is the Richardson constant for a-Si and V is the applied bias. The a-Si thickness for the simulation was chosen to be 45nm. The simulations were performed using Silvaco Atlas [11]. (See appendix A.2 for detailed parameters).

3.2.2 Applicability of Local Field Dependent Velocity Model

Due to very fast momentum relaxation time in a-Si [18], within a very short period of time (<10fs), the velocity in a-Si becomes independent of past history and depends only on the local electric field. The empirical equation of motion for electrons in a-Si can be written as [19]:

$$\frac{dv_d}{dt} = \frac{q\mathcal{E}}{m^*} - \frac{v_d}{\tau_p} \quad (3.10)$$

Here, v_d is the drift velocity and τ_p is the momentum relaxation time. Now solving for v_d, we get:

$$\frac{d}{dt}\left(e^{t/\tau_p} v_d\right) = e^{t/\tau_p} \frac{q\mathcal{E}}{m^*}$$

$$e^{t/\tau_p} v_d = \frac{\tau_p q\mathcal{E}}{m^*} e^{t/\tau_p} + C$$

$$v_d = \frac{\tau_p q\mathcal{E}}{m^*} + Ce^{-t/\tau_p}$$

Using the boundary condition, @t=0, v_d=0; we get:

$$C = -\frac{\tau_p q\mathcal{E}}{m^*}$$

$$v_d = \frac{\tau_p q\mathcal{E}}{m^*}\left(1 - e^{-t/\tau_p}\right) \quad (3.11)$$

The steady state value of $v_d = \frac{\tau_p q\mathcal{E}}{m^*} = \mu\mathcal{E}$.

Since our device dimension is small, we want to see if this is applicable in our case. To estimate the distance travelled to reach this steady state velocity, we assume that it takes $5\tau_p$.

$$v_d = \frac{dx_d}{dt} \Rightarrow x_d = \int v_d dt$$

$$x_d = \int_0^{5\tau_p} \frac{\tau_p q\mathcal{E}}{m^*}(1 - e^{-t/\tau_p})dt$$

$$= \frac{\tau_p q\mathcal{E}}{m^*}[t + \tau_p e^{-t/\tau_p}]_0^{5\tau_p} = \frac{\tau_p q\mathcal{E}}{m^*}\left[5\tau_p + \tau_p e^{-5} - \tau_p\right] = \frac{\tau_p{}^2 q\mathcal{E}}{m^*}[4 + e^{-5}]$$

$$x_d = \frac{4\tau_p{}^2 q\mathcal{E}}{m^*} \quad (3.12)$$

After travelling this distance, the velocity becomes independent of previous history and depends only on the local electric field. In order to see, if this model is applicable for our device dimension, we plug in the values from [18], $\tau_p = 1fs, m^* = 0.2m_e$ and Electric field in our case, E=10^6 V/cm, we get, $x_d = 3.51\, A^0\ (0.351nm)$. This is much shorter than the thickness of a-Si even for the case of thin a-Si layer. Therefore, it is reasonable to relate electron velocity to the local electric field, which gives the notion of mobility (i.e. $v_d = \mu\mathcal{E}$) in our transport equations (3.3a) and (3.3b).

3.2.3 Applicability of Local Field Dependent Impact Ionization Model

Similar to local field dependent velocity model, in order to apply local electric field dependent impact ionization model in (3.7) for mesoscopic systems, we need to justify the carrier multiplication coefficients can be represented by a function of local electric field even though in theory, they should depend on the kinetic energy of carriers under certain bias voltage. In the following passage, we present physical arguments to justify the use of this local model in sub 100nm a-Si system.

For carrier multiplication to occur, the carrier kinetic energy needs to reach a threshold energy, E_0 that requires a minimum distance for the carrier to gain such energy. Neglecting inelastic phonon scattering which involves small energy changes compared to E_0, we approximate the minimum distance a carrier needs to travel to achieve E_0: $d = \frac{E_0}{q\mathcal{E}}$,There is no multiplication within distance less than d, which is often called the "dead space" for carrier multiplication. Using the energy relaxation time model [19], the evolution of electron energy in a-Si can be represented

by (3.13a) and (3.13b). In (3.13a) and (3.13b), the first term in the R.H.S. is the kinetic energy gained from the external electric field, the second term corresponds to the rate of energy loss due to inelastic scattering, and the third term in R.H.S. of (3.13b) denotes energy loss by impact ionization.

$$\frac{dT}{dt} = qv_d(\mathcal{E})\mathcal{E} - \frac{T}{\tau_e}\,; \quad for\ 0 \le t \le t_d \qquad (3.13a)$$

$$\frac{dT}{dt} = qv_d(\mathcal{E})\mathcal{E} - \frac{T}{\tau_e} - \overline{\alpha_e} v_d E_o; \quad for\ t_d \le t \le t_{tr} \qquad (3.13b)$$

Here T is the electron kinetic energy, τ_e is the energy relaxation time, t_d is the time to cross the dead space, t_{tr} is the transit time across the a-Si layer, E_0 is the average energy loss by the hot electron after creating impact ionization, and $\overline{\alpha_e}$ is the electron impact ionization coefficient averaged over the range of kinetic energy. Formally the electron impact ionization coefficient, α_e depends on the kinetic energy and should be written as $\alpha_e(T)$ [20], [21]. Because our main purpose here is to show how the local field approximation for impact ionization works for different a-Si layer thickness, we assume that for a given a-Si layer thickness, one can use an average impact ionization coefficient $\overline{\alpha_e}$ in (3.13) to simplify the equation. Then we can solve (3.13) as:

$$T(t) = v_d\tau_e[q\mathcal{E}]\left(1 - e^{-t/\tau_e}\right); \ for \ 0 \le t \le t_d \qquad (3.14a)$$

$$T(t) = v_d\tau_e[q\mathcal{E} - \overline{\alpha_e}E_o]\left(1 - e^{-(t-t_d)/\tau_e}\right) + T(t_d)e^{-(t-t_d)/\tau_e}; for\ t_d \le t \le t_{tr} \qquad (3.14b)$$

We define energy relaxation length due to phonon scattering, $l_e = v_d\tau_e$ which $v_s\tau_e$ (v_s: electron saturation velocity) under high field. By changing the variable in (3.14) from time to distance, we represent the electron kinetic energy dependence on distance as:

$$T(x) = v_d \tau_e [q\mathcal{E}](1 - e^{-x/l_e}); \;\; for\; 0 \le x \le d \qquad (3.15a)$$

$$T(x) = v_d \tau_e [q\mathcal{E} - \overline{\alpha_e} E_o](1 - e^{-(x-d)/l_e}) + d[q\mathcal{E}]e^{-(x-d)/l_e}; \quad for\; d \le x \le l_a \qquad (3.15b)$$

Here, l_a is the thickness of a-Si. In order to have impact ionization, a-Si has to be thicker than the dead space (i.e. $l_a > d$) so that the carrier kinetic energy can reach the required impact ionization energy. On the other hand, if the a-Si thickness is much greater than the energy relaxation length (i.e. $l_a \gg l_e$), the exponential terms in (3.15b) vanish and the electron kinetic energy becomes

$$T(\infty) = l_e[q\mathcal{E} - \overline{\alpha_e}(\infty)E_0] \qquad (3.16)$$

Where, $\overline{\alpha_e}(\infty)$ is the average electron impact ionization coefficient for thick a-Si. This is the usual case where the local-field impact ionization model works since the electron kinetic energy depends only on the local electric field $\mathcal{E}$, and so is the average impact ionization coefficient $\overline{\alpha_e}(\infty)$. Therefore, for a thick a-Si layer (i.e. $l_a \gg l_e$), it is justified to represent the impact ionization coefficient as a function of the local E-field (i.e. $\alpha_e(\mathcal{E})$) which is the local field model in (3.7).

However, the above results need to be modified for thin a-Si that satisfies the relation: $d < l_a < l_e$ (i.e. $\frac{l_e}{l_a} > 1$). Here we find the average kinetic energy of electrons outside the dead space ($l_a > d$) can be represented by the following expression (details in appendix A.1)

$$\bar{T} = l_e\left[q\mathcal{E} + \left(\frac{l_e}{l_a} - 1\right)\overline{\alpha_e}E_0\right] \qquad (3.17)$$

where $\bar{T}$ is the average electron kinetic energy. Therefore, we can obtain the following relation as the lower bound for $\bar{T}$ in the case of thin a-Si:

$$\bar{T} \ge l_e\left[q\mathcal{E} + \left(\frac{l_e}{l_a} - 1\right)\overline{\alpha_e}(\infty)E_0\right] > T(\infty) \; (3.18)$$

The result in (3.18) contains two important messages. First of all, (3.18) shows that even a conservative estimate of the average electron kinetic energy (i.e. if we consider equality sign in equation (18)) for thin a-Si is greater than that of a long a-Si layer (i.e. $\bar{T} > T(\infty)$). Secondly, and more importantly, since the electron impact ionization coefficient is a monotonically increasing function of the kinetic energy, $\bar{T} > T(\infty)$ also means $\overline{\alpha_e} > \overline{\alpha_e}(\infty)$. In other words, the average electron impact ionization coefficient for a thin a-Si that satisfies the condition $d < l_a < l_e$ has a greater impact ionization coefficient than that of a thick a-Si layer. Here "thick" a-Si layer means $l_a \gg l_e$. In both cases, one can approximately represent the impact ionization coefficient as a function of electric field as shown in (3.7) but for devices with a thin a-Si layer, the parameters in (3.7) needs to be adjusted from the values used to model thick a-Si layers. We will adopt this approach in the following section when we compare the experimental results with the simulation results.

3.3 Results and Discussions

This section is comprised of four parts. At first, we show the DC characteristics of the device from our simulations and present the rationale to perform frequency dependent analysis. Next, we show the frequency response of the device and compare the calculated results with experiment. Afterwards, we explain the reason of discrepancy in gain value in thin and thick a-Si. Finally, we propose the physical picture of the gain mechanism in amorphous materials in general.

3.3.1 DC Gain Characteristics

For photoconductors with ohmic contacts, the photoconductive gain is equal to $\frac{\tau_R}{\tau_{tr}}$, the ratio of minority carrier lifetime to carrier transit time [22]. When one or both ohmic contacts are replaced with Schottky contact(s), gain has also been observed [23]–[26] although its value is no longer described by the simple relation $\frac{\tau_R}{\tau_{tr}}$.

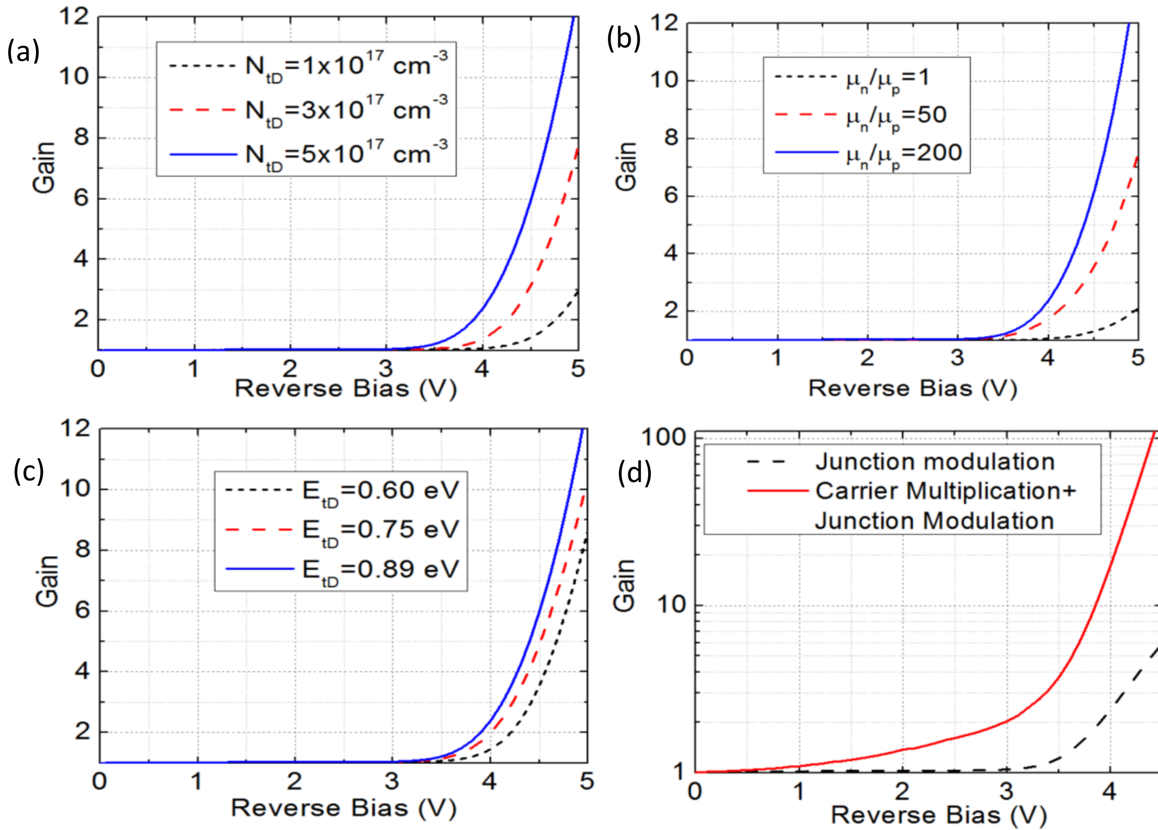

Figure 3.3: Calculated Gain versus Reverse Bias for (a) different trap density, (b) different mobility ratio, (c) different trap energy levels and (d) junction modulation gain coupled with carrier multiplication gain. The calculations in (a-c) include only junction modulation gain from material defects.

Instead, its gain was found to be related to the defect states (traps) in the semiconductor. In the presence of traps, photogenerated carriers can be captured in the defect states, which alters the potential profile inside the semiconductor. This results in additional band bending and affects

the tunneling current at the electrode/semiconductor junction [23]–[26]. Applying such model to a device with an a-Si layer sandwiched by two metal (or ITO) contacts, we find that indeed there is an increase in the tunneling current due to photogenerated carrier trapping and modulation of the potential profile at the metal/a-Si junction, manifested as amplification of photoresponse. Since holes travel at a much lower speed than electrons in a-Si, they are more likely to be captured by the donor states as they move towards the ITO electrode (cathode). The local accumulation of holes lowers the effective thickness of tunneling barrier, increasing the tunneling current. Since such current increase is resulted from trapping of photogenerated holes, it can be considered as a different type of photoconductive gain, which is also referred as the effect of junction modulation[26], [27].

Fig. 3.3 shows the dependence of junction modulation gain on different material parameters including the trap density, the mobility ratio between electrons and holes, the energy level of traps (i.e. donor trap energy from the top of valence band), and at last, the combined effects of traps and carrier multiplication by impact ionization. In our structure of ITO/a-Si/n+ Si substrate, donor type traps are found to have the strongest effect on the junction modulation gain due to their abilities to capture holes. For simplicity, we have assumed both donor type traps and acceptor type traps have a single energy level, and the density is in the similar order of magnitude found in deep level transient spectroscopy (DLTS) measurements in a-Si [12].

3.3.2 Frequency Response

To investigate the origins of gain in a-Si devices, we measured the frequency dependence of gain hypothesizing that those deep traps having the strongest effect on junction modulation will have a much lower frequency response than impact ionization. We measured the gain of a-Si

devices from 200 Hz to 10 MHz and compared the results with simulations. Experimentally we observed that between 1KHz and 10KHz, the gain started to drop with frequency from ~1300 to ~350 and then stayed at this value throughout 10 MHz, the highest frequency we have measured (Fig. 3.4(a)).

To understand the behaviors of frequency dependent gain, we simulated a few scenarios. First, we simulated two cases: (i) only with traps without carrier multiplication process and ii) with carrier multiplication without any traps. For the first case, we observed high gain at low frequency, but the gain dropped significantly when the frequency was greater than 1 KHz (Fig. 3.4(b), dashed). For the second case, the gain remained flat over the entire frequency range (Fig. 3.4(b), solid). Next, we included both traps and carrier multiplication effect and adjusted the multiplication coefficients and trap parameters to match experimental gain values. The result shown in Fig. 3.4(c) displays a trend that agrees well with the experimental results in Fig. 3.4(a).

From the above analyses, we conclude that low frequency gain in a-Si photodetectors is attributed to the combined contributions of junction modulation gain and carrier multiplication gain. Above certain frequencies (e.g. 1kHz-10kHz), the trap dynamics cannot keep up with the photocarrier modulation by the incoming light. As a result, the observed gain at higher than 10 KHz is almost entirely produced by carrier multiplication.

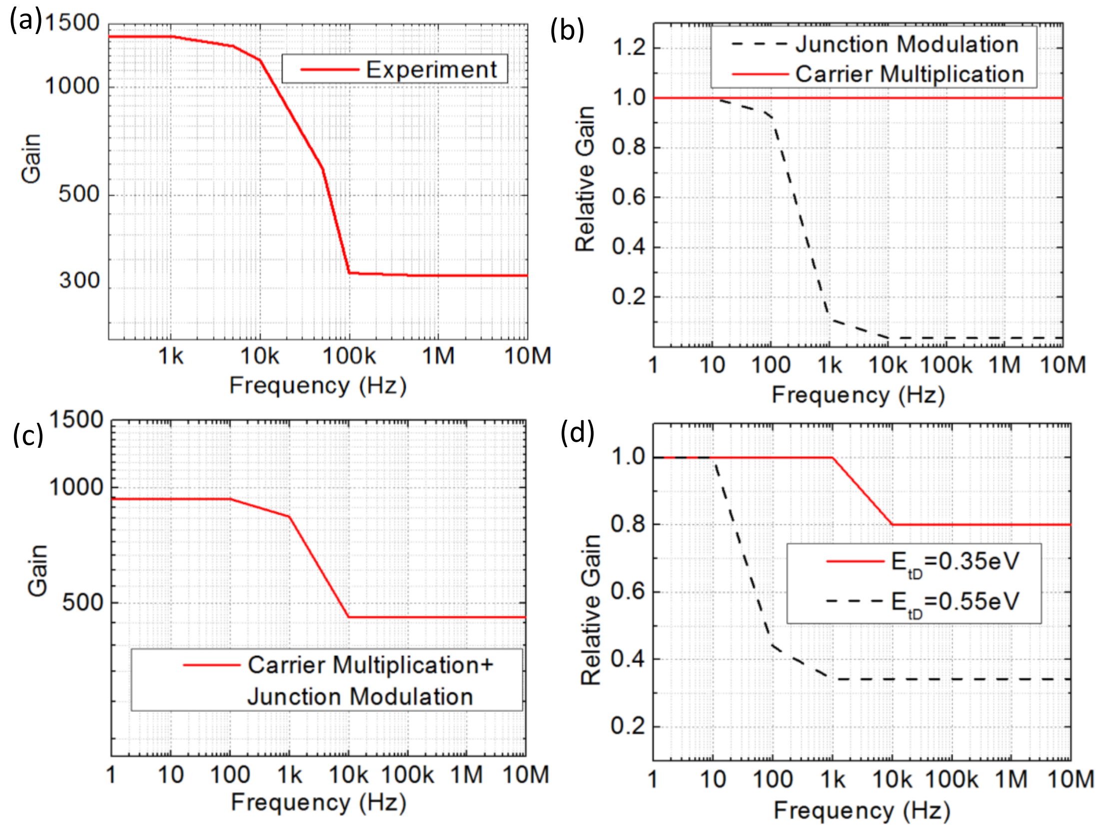

Figure 3.4: (a) Measured gain vs frequency. (b) Simulated gain versus frequency when only traps (dashed) and only carrier multiplication (solid) are considered. Both curves are normalized to their respective low frequency values. (c) Simulated gain vs frequency including both trap-induced junction modulation and carrier multiplication to match experimental results in (a). (d) Normalized frequency dependence of gain (including junction modulation and carrier multiplication) for different energy level of traps.

We further investigated the significance of trap energy level on the frequency response of gain. As shown in Fig. 3.4(d), as energy level of trap goes further away from band edge, the frequency response decreases. This is consistent with the property that carriers captured by deeper levels take longer time to escape, thus showing an earlier gain roll off. On the other hand, for traps closer to band edges (solid curve), the gain change from low frequency to high frequency is not significant and the gain is mainly dominated by carrier multiplication.

3.3.3 Gain Dependence on a-Si Thickness

The above numerical results from the transport equations and experimental data provide unequivocal evidences for the existence of carrier multiplication effect in a-Si. However, there is an appreciable difference in the measured carrier multiplication gain in thin [28] and thick [29] a-Si layer under similar magnitude of electric field. Fig. 3.5(a) shows the measured dependence of photocurrent on the applied electric field for devices with 100nm and 40nm thick a-Si. Due to effects of non-uniform field distribution and mesa side wall, we were not able to perfectly fit the measured results using the impact ionization model in (3.7). However, from the parameters that produced the closest fit (Fig. 3.5(a)), we found that the impact ionization coefficient for thin a-Si devices is significantly greater than the value for thick a-Si devices. The field dependent impact ionization coefficients for both a-Si thicknesses are plotted in Fig. 3.5(b). Next, we elucidate how the impact ionization coefficient for a-Si can be thickness dependent.

There have been many works to model impact ionization in crystalline material [31]–[33]. Theories for impact ionization were first discussed in Shockley's lucky electron model [31] and later on were modified for lucky drift model where the carriers continue to gain energy after elastic collisions by drifting along the electric field [32], [33]. Lucky drift model was extended to a-Si and other low mobility materials [34]–[36] but these models do not provide explanations for dependence of impact ionization efficiency on the thickness of a-Si observed experimentally.

These results can be interpreted as follows using (3.18), which shows that the average electron kinetic energy increases as the a-Si thickness (l_a) decreases. Since the electron impact

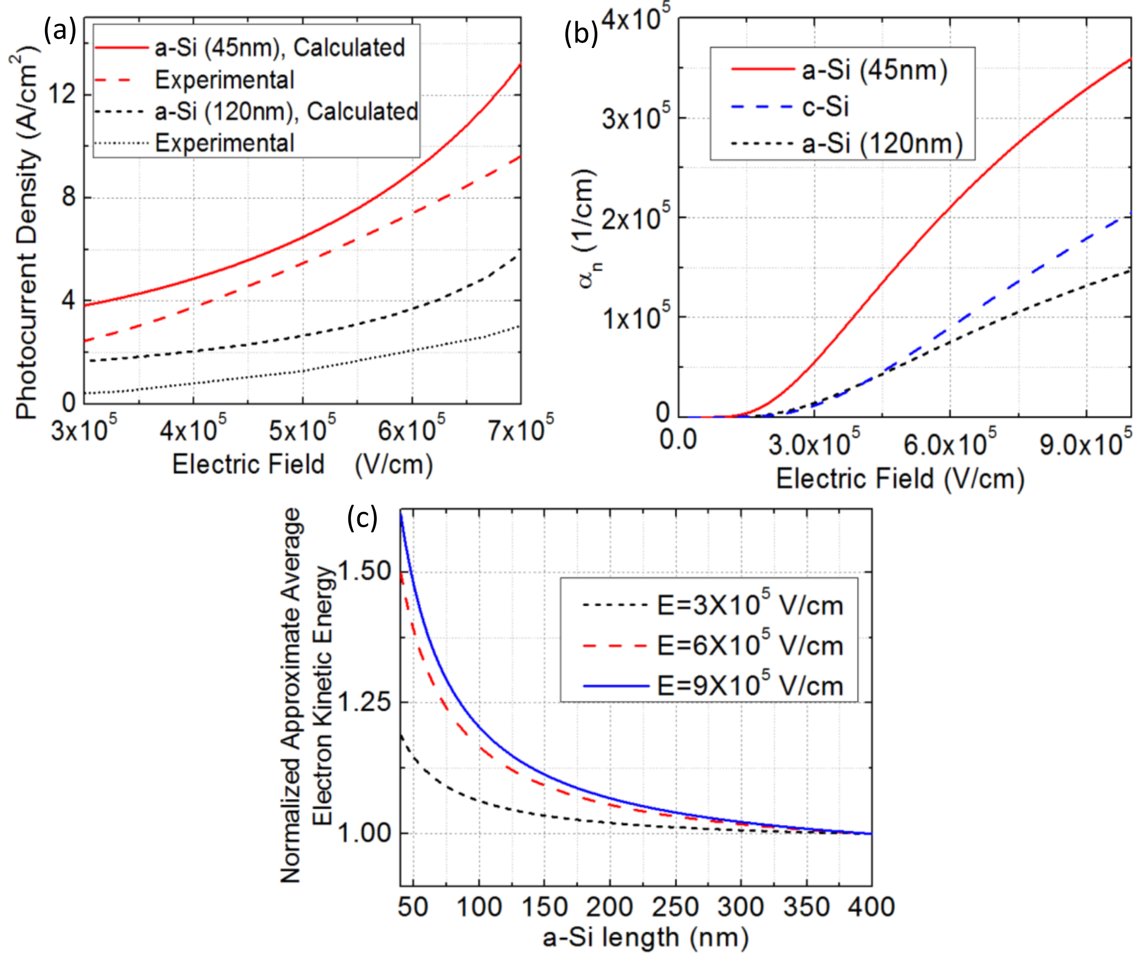

Figure 3.5: (a) Photocurrent versus Electric Field for two different a-Si thicknesses, (b) Field dependence of electron impact ionization coefficient for different thickness of a-Si. The curves were calculated from the local field model with parameters that produce the best fit with the experimental results in (a). Also included in (b) is the literature reported value for crystalline Si (c-Si) [30]. (c) Approximate average electron kinetic energy (normalized w.r.t. infinitely thick a-Si) vs a-Si length under different applied E-field, calculated from (3.18)

ionization coefficient, α_e increases monotonically with the electron kinetic energy, equation (3.18) and Fig. 3.5(c) also show that α_e increases as the a-Si thickness decreases, which explains qualitatively the results in Fig. 3.5(b). It was reported that the electron energy relaxation time in a-Si is around 1 pico-second, which is more than 2 orders magnitude longer than the momentum relaxation time [18]. This produces an energy relaxation length, l_e of the order of 100 nm in high electric field. With this estimated l_e, the lower limit of $\bar{T}(l_a)$ (normalized w.r.t. infinitely thick

a-Si) from equation (3.18) is plotted in Fig 3.5(c) where the E-field dependence of $\overline{\alpha_e}(\infty)$ is obtained from the empirical formula of local field approximation in equation (3.7).

The results in Fig. 3.5(c) can be understood by the following intuitive explanation. In the system there is only one source for carriers to gain energy (i.e. the applied E-field) but there are two sources from which the carriers lose their kinetic energy: impact ionization and inelastic phonon scattering. If the a-Si layer thickness is much greater than the characteristic length for inelastic phonon scattering, the electron kinetic energy reaches its steady state value. However, if the a-Si thickness is smaller than l_e, then one of the two energy loss mechanisms (i.e. inelastic phonon scattering) does not produce its full effect, thus leading to a higher average electron kinetic energy. This phenomenon can be considered as "electron kinetic energy overshoot" rather than "electron velocity overshoot". Since electron (hole) impact ionization coefficient is a monotonically increasing function of electron (hole) kinetic energy [20], such "electron (hole) kinetic energy overshoot" gives rise to a higher impact ionization coefficient.

By fitting the impact ionization coefficients for electrons and holes in thin and thick a-Si to match the experimental data (Fig. 3.5(b)), we found a particularly interesting phenomenon that the electron impact ionization coefficient for a thin (<50nm) a-Si layer can be even greater than that of crystalline silicon [30] even though the latter is known to have much superior material quality and carrier mobility. On the other hand, for ~100nm thick a-Si, the electron multiplication coefficient is lower than c-Si as one would expect.

3.4 Proposed Gain Mechanism in Amorphous Materials

Intuitively, one would expect the chance for a carrier to achieve sufficient kinetic energy to reach the impact ionization threshold is less in a-Si than in c-Si due to scattering with random

potential fluctuations. However, this unusual characteristic can be explained by a different impact ionization process in a-Si that involves the localized states in the bandtails, as illustrated in Fig. 3.6.

In conventional crystalline silicon, impact ionization excites electrons from valence band to conduction band with all particles being Bloch waves with well defined k-vectors. Fig. 3.6(a-d) shows the impact ionization processes in c-Si. Due to the nature of disorder, a-Si has long band tails of localized states [6], [9] as well as strong and localized electron-phonon coupling [8]. Due to the above material properties, the carrier multiplication process in a-Si can have different pathways than c-Si. Photogenerated electrons are collected at the n++ Si and holes will gain kinetic energy as they move toward the ITO electrode along the applied electric field (Fig. 3.6(e)). If the kinetic energy is higher than the required energy for impact ionization, these holes can excite electrons from the valence band (V.B.) to localized states near the conduction band (C.B.) (bottom of Fig. 3.6(f)). The presence of shallow traps as bandtail states facilitate the excitation because electrons in these states are localized and help relax the k-selection rule. Subsequently, the electrons in the localized bandtail states can enter the mobile states in the conduction band (C.B.) via phonon excitation or field-enhanced tunneling (Fig. 3.6(g)). At the same time, the presence of deep states can capture some mobile carriers and change the band bending at the metal/electrode interface and hence create a path for enhanced tunneling injection current as shown in top of Fig. 3.6(f). The electrons in mobile conduction band will then gain kinetic energy from the applied E-field and excite new e-h pairs where the secondary holes can come from the localized states from the tail of the V.B., which again relaxes the k-selection rule. As a result, the impact ionization process in disordered material like a-Si is similar to the impact ionization in c-Si except that in a-Si, the carrier multiplication process may involve localized states to help relax the k-selection rule.

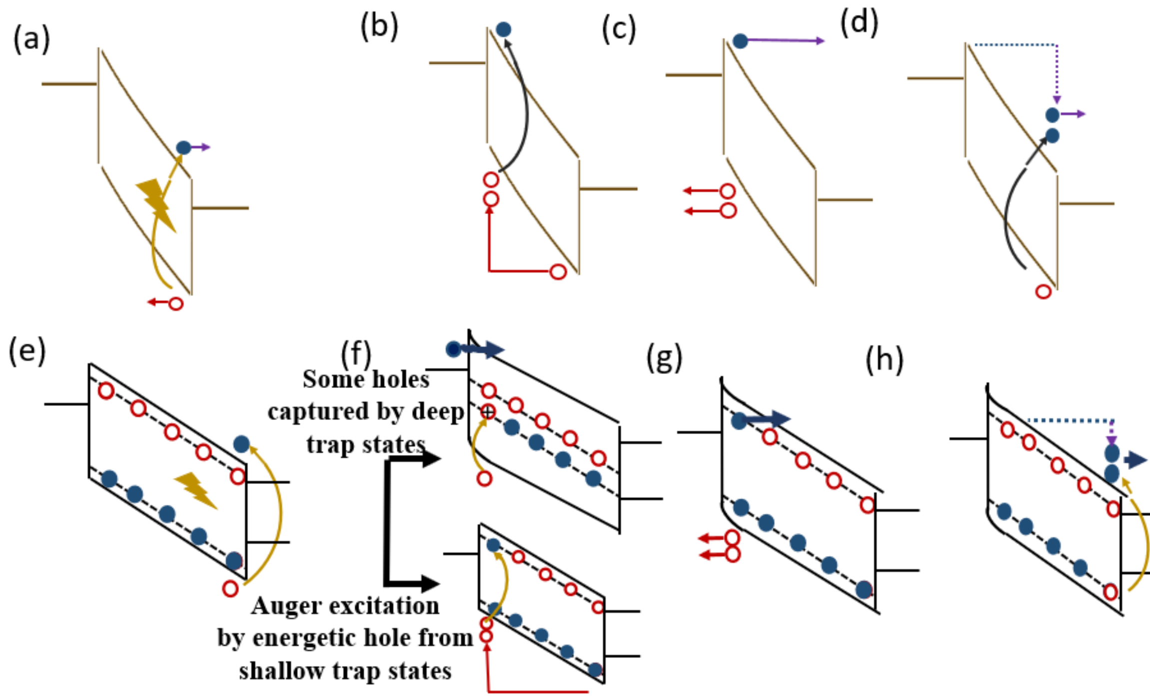

Figure 3.6: Pictorial representation of carrier multiplication processes in c-Si (a-d) and a-Si (bottom row, e-h). (a) and (e) show photogeneration of e-h pair by incidence of light. (b) and bottom of (f) show the hole can excite another e-h pair via impact ionization by losing its kinetic energy gained from the applied E-field. It is to be noted that the process in c-Si (b) requires band to band transition whereas the process in a-Si (f) involves a localized state that relaxes the k-selection rule to make the excitation process more likely. At the same time, some of the holes can be captured by deep donor states and can cause additional band bending to create another path of additional electron injection through junction modulation as shown in top of (f). (c) and (g) show the movement of the electron. In c-Si, the electron is already in mobile band but in a-Si the electron from a localized state needs to enter the mobile band via phonon absorption or field-enhanced tunneling. (d) and (h) show this secondary electron can create another cycle of e-h pair generation.

These differences can result in different material parameters that model the impact ionization coefficients in (3.7) and have been observed experimentally in cycling excitation process (CEP) devices [28], [1], [2], [5].

3.5 Conclusion

To summarize, we have performed numerical analysis of the transport equations in a thin a-Si layer to explore and interpret the physical mechanisms for photocurrent gain. We have considered dynamics of donor type and acceptor type traps as well as the effect of impact ionization. We also provided physical arguments of mean free paths for momentum relaxation and energy relaxation to justify the use of local field approximation to model impact ionization coefficient in thin a-Si. The simulation results show that although both the effect of junction modulation and impact ionization contribute to the DC gain, the junction modulation effect resulted from deep traps has a low frequency response. At frequencies above 10 KHz, the gain is almost entirely produced by impact ionization. The simulation results agree well with the experimental results, providing strong evidences for the existence of highly efficient carrier multiplication process in a thin a-Si layer.

Then we explained why the impact ionization coefficient in thin a-Si devices can be greater than that in thick a-Si devices. We infer that when the a-Si layer thickness is smaller than the characteristic length for energy relaxation, the average kinetic energy of carriers can be greater than that in a thick a-Si layer, leading to a greater impact ionization coefficient. Finally, by comparing the impact ionization coefficients between c-Si [30] and a-Si using values that fit the experimental data, we found that the impact ionization coefficients for thin a-Si can be greater than the values for c-Si. Therefore, besides clarifying the gain mechanisms in a-Si, this chapter also sheds light on the recent thin a-Si CEP detectors that report high gain and high gain-bandwidth product [28] and more recently, single photon sensitivity [37].

This chapter, in part, is a reprint of material as it appears in the following publications:

I. A. Niaz, M.A.R. Miah, L. Yan, Y. Yu, Z. He, Y. Zhang, A. C. Zhang , J. Zhou , Y.H. Zhang and Y-H. Lo "Modeling Gain Mechanisms in Amorphous Silicon due to efficient carrier multiplication and trap induced junction modulation", Journal of Lightwave Technology , 2019.

L. Yan, Y. Yu, A. C. Zhang, D. Hall, I. A. Niaz, M.A.R. Miah, Y-H. Liu, Y-H. Lo "An amorphous silicon photodiode with 2 THz gain-bandwidth product based on cycling excitation process," Applied Physics Letters 111, 101104 (2017)

The dissertation author was primary/co-author of these papers.

References:

[1] Y. Zhou, Y.-H. Liu, S. N. Rahman, D. Hall, L. J. Sham, and Y-H. Lo, “Discovery of a photoresponse amplification mechanism in compensated PN junctions,” *Applied Physics Letters*, vol. 106, no. 3, p. 031103, Jan. 2015.

[2] Y-H. Liu, L. Yan, A. Zhang, D. Hall, I. A. Niaz, Y. Zhou, L. J. Sham and Y-H. Lo, “Cycling excitation process: An ultra efficient and quiet signal amplification mechanism in semiconductor,” *Appl. Phys. Lett.*, vol. 107, no. 5, p. 053505, Aug. 2015.

[3] D. Hall, B. Li, Y-H. Liu, L. Yan, and Y-H. Lo, “Complementary metal–oxide–semiconductor compatible 1060 nm photodetector with ultrahigh gain under low bias,” *Opt. Lett., OL*, vol. 40, no. 19, pp. 4440–4443, Oct. 2015.

[4] Y-H. Liu, A. Zhang, M. A. R. Miah, D. Hall, I. A. Niaz, L. Yan, Y. Yu, M. S. Kavrik, and Y-H. Lo, “Cycling excitation process for light detection and signal amplification in semiconductors,” presented at the SPIE Nanoscience + Engineering, San Diego, California, United States, 2016, p. 99330C.

[5] M. A. Raihan Miah, I. A. Niaz, Y-H. Liu, D. Hall, and Y.H. Lo, “A high-efficiency low-noise signal amplification mechanism for photodetectors,” presented at the SPIE OPTO, San Francisco, California, United States, 2017, p. 101080X.

[6] G. Allan, C. Delerue, and M. Lannoo, “Electronic structure and localized states in a model amorphous silicon,” *Phys. Rev. B*, vol. 57, no. 12, pp. 6933–6936, Mar. 1998.

[7] D. A. Drabold and P. A. Fedders, “Electronic consequences of the mutual presence of thermal and structural disorder,” *Phys. Rev. B*, vol. 60, no. 2, pp. R721–R725, Jul. 1999.

[8] R. Atta-Fynn, P. Biswas, and D. A. Drabold, “Electron--phonon coupling is large for localized states,” *Phys. Rev. B*, vol. 69, no. 24, p. 245204, Jun. 2004.

[9] K. Chew, Rusli, S. F. Yoon, J. Ahn, Q. Zhang, V. Ligatchev, E. J. Teo, T. Osipowicz, and F. Watt, “Gap state distribution in amorphous hydrogenated silicon carbide films deduced from photothermal deflection spectroscopy,” *Journal of Applied Physics*, vol. 91, no. 7, pp. 4319–4325, Mar. 2002.

[10] J. Bullot and M. P. Schmidt, “Physics of Amorphous Silicon–Carbon Alloys,” *phys. stat. sol. (b)*, vol. 143, no. 2, pp. 345–418, Oct. 1987.

[11] “Atlas User Manual.” Silvaco Inc., 30-Aug-2016.

[12] D. V. Lang, J. D. Cohen, and J. P. Harbison, “Measurement of the density of gap states in hydrogenated amorphous silicon by space charge spectroscopy,” *Phys. Rev. B*, vol. 25, no. 8, pp. 5285–5320, Apr. 1982.

[13] D. M. Caughey and R. E. Thomas, “Carrier mobilities in silicon empirically related to

doping and field,” *Proceedings of the IEEE*, vol. 55, no. 12, pp. 2192–2193, Dec. 1967.

[14] W. T. White, C. G. Dease, M. D. Pocha, and G. H. Khanaka, “Modeling GaAs high-voltage, subnanosecond photoconductive switches in one spatial dimension,” *IEEE Transactions on Electron Devices*, vol. 37, no. 12, pp. 2532–2541, Dec. 1990.

[15] “Analysis and Simulation of Semiconductor Devices | S. Selberherr | Springer.” [Online]. Available: https://www.springer.com/us/book/9783709187548. [Accessed: 19-Feb-2019].

[16] T. Ishida, H. Kobayashi, and Y. Nakato, “Structures and properties of electron-beam-evaporated indium tin oxide films as studied by x-ray photoelectron spectroscopy and work-function measurements,” *Journal of Applied Physics*, vol. 73, no. 9, pp. 4344–4350, May 1993.

[17] Y. Park, V. Choong, Y. Gao, B. R. Hsieh, and C. W. Tang, “Work function of indium tin oxide transparent conductor measured by photoelectron spectroscopy,” *Applied Physics Letters*, vol. 68, no. 19, pp. 2699–2701, May 1996.

[18] P. M. Fauchet, D. Hulin, R. Vanderhaghen, A. Mourchid, and W. L. Nighan, “The properties of free carriers in amorphous silicon,” *Journal of Non-Crystalline Solids*, vol. 141, pp. 76–87, Jan. 1992.

[19] G. H. Glover, “Study of electron energy relaxation times in GaAs and InP,” *Journal of Applied Physics*, vol. 44, no. 3, pp. 1295–1301, Mar. 1973.

[20] E. Cartier, M. V. Fischetti, E. A. Eklund, and F. R. McFeely, “Impact ionization in silicon,” *Appl. Phys. Lett.*, vol. 62, no. 25, pp. 3339–3341, Jun. 1993.

[21] T. Kotani and M. van Schilfgaarde, “Impact ionization rates for Si, GaAs, InAs, ZnS, and GaN in the GW approximation,” *Phys. Rev. B*, vol. 81, no. 12, p. 125201, Mar. 2010.

[22] S. M. Sze and K. K. Ng, *Physics of semiconductor devices*, 3rd ed. Hoboken, N.J: Wiley-Interscience, 2007.

[23] S. F. Soares, “Photoconductive Gain in a Schottky Barrier Photodiode,” *Jpn. J. Appl. Phys.*, vol. 31, no. 2R, p. 210, Feb. 1992.

[24] T. Sugeta, T. Urisu, S. Sakata, and Y. Mizushima, “Metal-Semiconductor-Metal Photodetector for High-Speed Optoelectronic Circuits,” *Japanese Journal of Applied Physics*, vol. 19, no. S1, p. 459, Jan. 1980.

[25] J. P. Vilcot, J. L. Vaterkowski, D. Decoster, and M. Constant, “Temperature effects on high-gain photoconductive detectors,” *Electronics Letters*, vol. 20, no. 2, pp. 86–88, Jan. 1984.

[26] R. R. Mehta and B. S. Sharma, “Photoconductive gain greater than unity in CdSe films with Schottky barriers at the contacts,” *Journal of Applied Physics*, vol. 44, no. 1, pp. 325–328, Jan. 1973.

[27] C. Y. Chen, “Theory of a modulated barrier photodiode,” *Appl. Phys. Lett.*, vol. 39, no. 12, pp. 979–981, Dec. 1981.

[28] L. Yan, Y. Yu, A. Zhang, D. Hall, I. A. Niaz, M.A.R. Miah, Y-H. Liu, Y-H. Lo, "An amorphous silicon photodiode with 2 THz gain-bandwidth product based on cycling excitation process," *Appl. Phys. Lett.*, vol. 111, no. 10, p. 101104, Sep. 2017.

[29] M. Akiyama, M. Hanada, H. Takao, K. Sawada, and M. Ishida, "Excess Noise Characteristics of Hydrogenated Amorphous Silicon p-i-n Photodiode Films," *Jpn. J. Appl. Phys.*, vol. 41, no. 4S, p. 2552, Apr. 2002.

[30] R. Van Overstraeten and H. De Man, "Measurement of the ionization rates in diffused silicon p-n junctions," *Solid-State Electronics*, vol. 13, no. 5, pp. 583–608, May 1970.

[31] W. Shockley, "Problems related top-n junctions in silicon," *Czech J Phys*, vol. 11, no. 2, pp. 81–121, Feb. 1961.

[32] B. K. Ridley, "Lucky-drift mechanism for impact ionisation in semiconductors," *J. Phys. C: Solid State Phys.*, vol. 16, no. 17, pp. 3373–3388, Jun. 1983.

[33] E. Bringuier, "High-field transport statistics and impact excitation in semiconductors," *Phys. Rev. B*, vol. 49, no. 12, pp. 7974–7989, Mar. 1994.

[34] K. Jandieri, O. Rubel, S. D. Baranovskii, A. Reznik, J. A. Rowlands, and S. O. Kasap, "Lucky-drift model for impact ionization in amorphous semiconductors," *J Mater Sci: Mater Electron*, vol. 20, no. 1, pp. 221–225, Jan. 2009.

[35] O. Rubel, S. D. Baranovskii, I. P. Zvyagin, P. Thomas, and S. O. Kasap, "Lucky-drift model for avalanche multiplication in amorphous semiconductors," *physica status solidi (c)*, vol. 1, no. 5, pp. 1186–1193, 2004.

[36] K. Jandieri, O. Rubel, S. D. Baranovskii, A. Reznik, J. A. Rowlands, and S. O. Kasap, "One-dimensional lucky-drift model with scattering and movement asymmetries for impact ionization in amorphous semiconductors," *physica status solidi c*, vol. 5, no. 3, pp. 796–799, 2008.

[37] L. Yan, M. A. Raihan Miah, Y-H. Liu, and Y-H. Lo, "Single photon detector with a mesoscopic cycling excitation design of dual gain sections and a transport barrier," *Opt. Lett.*, vol. 44, no. 7, p. 1746, Apr. 2019.

Chapter 4

Quantitative Analysis of Defect Assisted Carrier Multiplication in Amorphous Silicon

Chapter 4 will describe a theoretical framework to calculate the carrier multiplication process in a-Si or other disordered materials involving donor acceptor pairs (DAPs). It will provide detailed calculations of the carrier multiplication rate in disordered material modeled by the co-existence of mobile bands and bandgap states next to each mobile band. The analysis will also show the relations between detector characteristics and key parameters such as the density of band tail states, layer thickness, and applied electric field. DAP assisted carrier multiplication rate will be computed first. Carrier multiplication coefficients for electrons and holes under given applied field are then calculated using a trial distribution function that satisfies both the continuity equation and the energy balance equation. Using the calculated carrier multiplication coefficients, voltage dependent gain of the device will be computed.

4.1 DAP Assisted Carrier Multiplication Formulation

4.1.1 Theoretical Framework

To reduce the computation complexity without losing the generality, we have approximated the band tail states in conduction and valence bands by two discreate levels. We denote these levels as localized donor and acceptor states. An empty donor state is positively

charged and near the mobile valence band, and an occupied acceptor state is negatively charged and near the mobile conduction band [1]. We calculate the donor-acceptor pair (DAP) assisted carrier multiplication rate in a-Si by assuming an energetic carrier in the mobile band is relaxed to a lower energy state to excite a donor-acceptor pair exciton which is then ionized into an e-h pair. Our current analysis does not include ionization of DAP exciton since under room temperature and high-field condition where the device operates, most DAP excitons are ionized into mobile bands rapidly. However, this simplification could overestimate the gain and ignore gain saturation, which will be manifested in the comparison between the calculation and the experiment.

For the DAP before excitation (i.e. occupied donor and unoccupied acceptor states), we used 1s hydrogen wavefunction with corrected mass and dielectric constant to approximate their wavefunction. For the wavefunctions of the energetic carrier and the carrier after losing part of its energy to excite the DAP pair, we employed density functional theory (DFT) computation [2] to calculate the Bloch wavefunctions where all bands of relevant energy levels (4 bands in conduction band and 4 bands in valence bands) were taken into account. This many-body calculation using Fermi's golden rule can produce carrier multiplication rate for amorphous material involving donor-acceptor pairs that relax the k-selection rule.

The above analysis produces carrier multiplication rate as a function of carrier energy. However, to connect the microscopic model to measurable device properties, we need to know how carriers, under an applied E-field, are distributed over the energy range and at each position in the gain medium. This requires solution of the Boltzmann transport equations. However, solving the coupled transport equations for electrons and holes including the realistic (non-parabolic) band structures, carrier multiplication process, as well as electron (hole) phonon scattering is extremely complicated. On the other hand, the bulk of work in literature that solved

the transport equations numerically or from Monte Carlo simulations have shown the general properties of the carrier distribution, which possesses a modified Gaussian-like function [3], [4]. Hence, we assumed a trial function of such property for carrier distribution. However, a legitimate trial distribution function must satisfy two key equations: carrier continuity equation and energy balance equation. Hence, we have used these criteria to choose the parameters in the carrier distribution function.

Another important remark is that we did not treat the momentum relaxation process in the transport equations as people do with conventional semiconductors. This is because for disordered materials such as a-Si, the momentum relaxation time is extremely short (1-10 fs) compared to the energy relaxation time, verified experimentally [5] and manifested by their very low mobility [6], [7]. As a result, in the time and length scales of our concern, the momentum of electrons and holes already reaches their steady state value and the motion of carriers can be simply characterized by their mobility even for thin a-Si layers [8]. On the other hand, since phonon scattering is not nearly as effective in relaxing carrier energy than it does with carrier momentum due to the large mass mismatch between ions and electrons (holes), carriers under high E-field can remain energetic. This provides another reason for disordered materials to become highly efficient for carrier multiplication. It is to be noted that carrier multiplication rate depends on carrier energy, not momentum. Therefore, an energetic electron with its momentum relaxed by phonon scattering can have a greater probability of producing impact ionization within a thin layer than a fast travelling electron of the same energy since the latter spends little time in the material. Therefore, from this consideration, the low mobility of disordered material can be more favorable than high mobility crystalline semiconductor in producing carrier multiplication. The difference becomes more pronounced if the gain medium is so thin that carriers in the crystalline material travel ballistically.

4.1.2 Quantum Mechanical Formulation of Carrier Multiplication Rate

In calculating the carrier multiplication process for a-Si, we focus on the most dominant process of having an energetic conduction (valence) band electron (hole) interacts with a DAP via Coulomb potential and excites the DAP into a DAP exciton. Fig. 4.1 sketches the schematic diagram of the process. Due to energy conservation, the hot carrier loses its energy to become a carrier of lower energy in the mobile band.

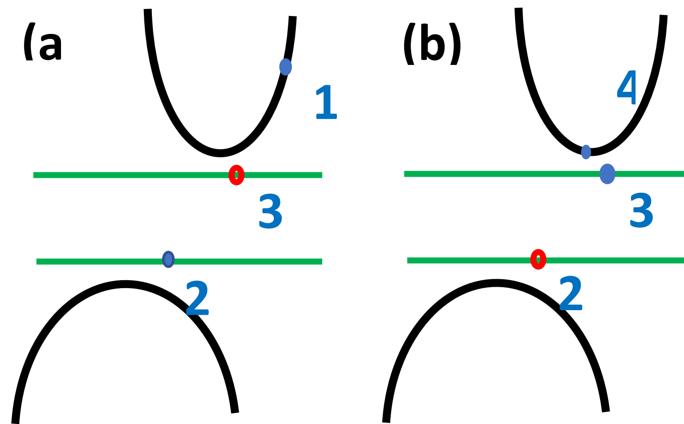

Figure 4.1: Schematic diagram of DAP pair assisted electron multiplication process in a-Si. (a) Before the start of multiplication process there are a high energy electron (state 1) and occupied donor (state 2), (b) Electron from state 1 loses its energy to excite a DAP pair and create a low energy electron (state 4) and exciton (state 2 and 3) at the end of multiplication process. At room temperature and high field, excitons are rapidly ionized to mobile bands.

We consider a perturbation Hamiltonian H' from the Coulomb interaction between the hot carrier with its position represented by $\boldsymbol{r_1}$ and a localized electron in the occupied state near the valence band at $\boldsymbol{r_2}$ as

$$H' = \frac{q^2}{4\pi\epsilon|\boldsymbol{r_1} - \boldsymbol{r_2}|} \qquad (4.1)$$

Where q is elementary electron charge and ϵ is dielectric constant of amorphous silicon.

Although the band diagram between a-Si and crystalline Si is very different near the band edge, the wavefunctions for high kinetic energy carriers are quite similar. Hence, we use the calculated wavefunction of crystalline Si for the carriers in the mobile band. We denote $\psi_{1,\boldsymbol{k_1}}(n_1, \boldsymbol{r})$ as the wavefunction of hot electron (hole) with wavevector $\boldsymbol{k_1}$, energy E_1 and band index n_1, and $\psi_{4,\boldsymbol{k_4}}(n_4, \boldsymbol{r})$ the wavefunction of conduction (valence) band state with wavevector $\boldsymbol{k_4}$, energy E_4 in the mobile bands, and band index n_4, both calculated from crystalline Si by the density functional theory (DFT) [2] .

On the other hand, wavefunction of the traps are modeled as 1s Hydrogen orbital. $\psi_2(\boldsymbol{r})$ and $\psi_3(\boldsymbol{r})$ are the wavefunctions of the localized donor and localized acceptor states respectively and can be represented as:

$$\psi_2(\boldsymbol{r}) = \frac{e^{-\frac{|\boldsymbol{r_D}|}{a_D}}}{\sqrt{\pi a_D^3}} \quad (4.2a)$$

$$\psi_3(\boldsymbol{r}) = \frac{e^{-\frac{|\boldsymbol{r_A}|}{a_A}}}{\sqrt{\pi a_A^3}} \quad (4.2b)$$

Where $\boldsymbol{r_A}$ and $\boldsymbol{r_D}$ are the distances from the position of the acceptor ($\boldsymbol{r_{acc}}$) and donor states ($\boldsymbol{r_{don}}$), respectively, i.e. $|\boldsymbol{r_A}| = |\boldsymbol{r_{acc}} - \boldsymbol{r}|$ and $|\boldsymbol{r_D}| = |\boldsymbol{r_{don}} - \boldsymbol{r}|$. a_D and a_A are Bohr radius for the donor and acceptor states. For our calculation, we put the acceptor at origin, i.e. $|\boldsymbol{r_A}| = |\boldsymbol{r}|$

For simplicity, we will assume that, all the shallow traps are at a single energy level E_2 (donor) or at E_3 (acceptor) with equal trap concentration N_T. From the first order perturbation theory [9]–[13], the excitation rate of a DAP exciton with electron-hole energy E_2 and E_3, R_{E_2,E_3}, can be represented as,

$$R_{E_2,E_3}(E_1, r_{acc}, r_{don})$$

$$= 2\frac{2\pi}{\hbar}\frac{V}{(2\pi)^3}\sum_{n_1,\boldsymbol{k_1}}\sum_{n_4}\int_{k_4}|M|^2\delta\left(E_{n1}(\boldsymbol{k_1}) + E_2 - E_3 - E_{n_4}(\boldsymbol{k_4})\right)d^3k_4 \quad (4.3)$$

where E_1 is the energy of the energetic carrier that initiates the process and E_4 is the energy the carrier decays to afterwards. V is the volume of amorphous silicon, and M is the matrix element. The summation over $n_1, \boldsymbol{k_1}$ includes those states in all the mobile conduction bands with wave vector $\boldsymbol{k_1}$ that have their energy eigen value E_1.

Above, we describe the process as if electrons are distinguishable. The anti-symmetry property of electron is considered in the expression of the matrix element M of the interaction [11], [14]

$$|M|^2 = \frac{1}{2}(|M_D|^2 + |M_E|^2 + |M_D - M_E|^2) \quad (4.4)$$

Here M_D is the direct process, i.e. the first electron is transitioned from state 1 to state 4 and the second electron is transitioned from a donor state (state 2) to an acceptor trap (state 3). Exchange interaction element, M_E is the same as M_D except that electrons are exchanged. Since M_D and M_E have very similar values [14], we can ignore the last term in (4).

We can then express M for electron-initiated carrier multiplication process involving a donor-acceptor pair as

$$M = \int_{r_1} \int_{r_2} \psi_{n4}^{*}(\boldsymbol{k_4}, \boldsymbol{r_1}) \psi_3^{*}(\boldsymbol{r_2}) H' \psi_{n1}(\boldsymbol{k_1}, \boldsymbol{r_1}) \psi_2(\boldsymbol{r_2}) d^3 r_1 d^3 r_2 \qquad (4.5)$$

Equation (4.5) can be simplified as follows,

$$M = \frac{8q^2 \sqrt{a_D^3 a_A^3}}{V \epsilon \pi^2} C(k_1, n_1; k_4, n_4) D\left(a_{A,} a_D, z_d, \boldsymbol{k_1}, \boldsymbol{k_4}\right) \quad (4.6)$$

Here C is the overlap integral between state 1 and 4 and expressed as

$$C(k_1, n_1; k_4, n_4) = \int_{\boldsymbol{r_1}} \frac{\psi_{n1}(\boldsymbol{k_1}, \boldsymbol{r_1})}{e^{i\boldsymbol{k_1}.\boldsymbol{r_1}}} \frac{\psi_{n4}^{*}(\boldsymbol{k_4}, \boldsymbol{r_1})}{e^{-i\boldsymbol{k_4}.\boldsymbol{r_1}}} d^3 r_1 \quad (4.7a)$$

Here $\psi_{n1}(\boldsymbol{k_1}, \boldsymbol{r_1})$ and $\psi_{n4}(\boldsymbol{k_4}, \boldsymbol{r_1})$ are Bloch functions directly solved from the DFT calculation. Dividing them by the plane wave term $e^{i\boldsymbol{k}.\boldsymbol{r}}$ gives the atomic part of the wavefunction.

D is defined as

$$D\left(a_{A,} a_D, r_{don}, \boldsymbol{k_1}, \boldsymbol{k_4}\right) = \frac{e^{-i(\boldsymbol{k_4} - \boldsymbol{k_1}).\boldsymbol{r_{don}}}}{(|\boldsymbol{k_4} - \boldsymbol{k_1}|)^2} \int_{\boldsymbol{k_2}} \frac{e^{-i\boldsymbol{k_2}.\boldsymbol{r_{don}}}}{(1 + a_A^2 k_2^2)^2 (1 + a_D^2 |\boldsymbol{k_4} - \boldsymbol{k_1} + \boldsymbol{k_2}|^2)^2} d^3 k_2 \, (4.7b)$$

Detailed derivations are given in appendix B.1. Similar equations can be derived for the hole-initiated carrier multiplication process. Substituting (4.6) into (4.3), the impact ionization rate produced by an energetic electron of energy E_1 can be calculated. Assuming equal concentration for both donor and acceptor trap states in the band tails of valence and conduction band, we can convert the distance between the nearest DAP pair into the density of acceptor and donor states, using the relation, $d_{DAP} = |\boldsymbol{r_{acc}} - \boldsymbol{r_{don}}| = |\boldsymbol{r_{don}}| = N_D^{-\frac{1}{3}} = N_{DAP}^{-\frac{1}{3}}$ Then the net rate of impact ionization via excitation of a DAP exciton by a hot electron of energy E_1 can be represented as,

$$R(E_1) \sim R_{E_2, E_3}(E_1, r_{don}) V N_{DAP} \quad (4.8)$$

4.1.3 Carrier Multiplication Coefficient Calculation

To find the carrier multiplication coefficients, we also need to know how electrons (holes) are distributed over energy. Instead of solving the transport equations for electrons and holes, we take a trial function that has the general characteristics of previously calculated distribution function by numerical analysis and Monte Carlo simulation [3], [4]. To determine the parameters in the trial function, we need to assure that the trial function for electron (hole) distribution satisfies two key equations: continuity equation (4.9) and energy balance equation (4.10) below.

$$\frac{\partial n(z)}{\partial t} = -\frac{\partial J_n}{\partial z} + v_d \langle \alpha_e(z, \mathcal{E}) \rangle n(z) - \frac{n(z) - n_o}{\tau} \qquad (4.9)$$

$$\frac{dn(z)\langle T(z, \mathcal{E}) \rangle}{dz} = n(z)\mathcal{E} - \frac{n(z)[\langle T(z, \mathcal{E}) \rangle - T_o]}{l_e} - n(z)\langle \alpha_e(z, \mathcal{E}) \rangle E_0 \quad for\ d \leq z \leq l_a \quad (4.10)$$

The terms in Eqs. (4.9) and (4.10) are defined below:

$T(z, \mathcal{E})$: kinetic energy of electron at position z under applied electric field $\mathcal{E}$.

$\langle T(z, \mathcal{E}) \rangle$: electron kinetic energy at $(z, \mathcal{E})$ averaged over energy T

$\langle \alpha_e(z, \mathcal{E}) \rangle$: electron multiplication coefficient at $(z, \mathcal{E})$ averaged over energy T.

T_o: electron kinetic energy at thermal equilibrium.

E_o: Excitation energy for a DAP pair.

d: dead space, i.e. minimum distance for an electron to gain sufficient energy to initiate carrier multiplication.

l_a: length a-Si gain medium.

v_d: electron drift velocity.

τ: electron lifetime.

n_o: electron concentration at thermal equilibrium.

$n(z)$: electron concentration at position z.

$J_n(z)$: electron flux at position z

l_e: electron energy relaxation length due to phonon scattering.

τ_e: electron energy relaxation time due to phonon scattering ($l_e = v_d \tau_e$).

Similar equations also exist for holes. According to their definitions $\langle T(z,\mathcal{E})\rangle$ and $\langle \alpha_e(z,\mathcal{E})\rangle$ can be represented as:

$$\langle T(z,\mathcal{E})\rangle = \frac{\int T f_e(T,z,\mathcal{E})\rho(T)dT}{\int f_e(T,z,\mathcal{E})\rho(T)dT} = \frac{\int T f_e(T,z,\mathcal{E})\rho(T)dT}{n(z)}; \qquad (4.11a)$$

$$\langle \alpha_e(z,\mathcal{E})\rangle = \frac{1}{v_d}\frac{\int R_e(T) f_e(T,z,\mathcal{E})\rho(T)dT}{\int f_e(T,z,\mathcal{E})\rho(T)dT}$$

$$= \frac{1}{v_d}\frac{\int R(T) f_e(T,z,\mathcal{E})\rho(T)dT}{n(z)} \qquad (4.11b)$$

Here $f_e(T,z,\mathcal{E})$ is the distribution function over energy T, $\rho(T)$ is the density of states for electrons and $R_e(T)$ is essentially $R(E_1)$ in Eq. (4.8) with a change of notation for electron scattering rate to avoid confusions. Here we would like to point out that the electron (hole) multiplication coefficient in (4.11b) has the electron (hole) drift velocity in the denominator. This shows explicitly how lower mobility favors carrier multiplication by allowing the energetic carriers to spend more time in the material.

In the following subsections, we describe in detail how we determine the electron distribution function $f_e(T, z, \mathcal{E})$ that depends on electron energy, position, and the applied electric field. Over the past decades, much work has been done for solving the carrier distribution function from Boltzmann transport equation [3], [4], [15]–[17]. Some of the works use Monte Carlo technique [3] whereas others use deterministic approach [4], [17]. Here we use an empirical trial distribution function described in Eq. (4.12), which resembles the shape of the published results [3], [4].

$$f_e(T, z, \mathcal{E}) = A \text{ when } T < \big(F - F_o - b \times F_R(T)\big)z \qquad (4.12a)$$

$$f_e(T, z, \mathcal{E}) = A \exp\left\{-\frac{\left[T - \left(F - F_o - b \times F_R(T)\right)z\right]^2}{2a^2}\right\} \text{ elsewhere} \quad (4.12b)$$

where, $F_R(T) \equiv R_e(T)E_0/v_d$; $F_0 \equiv \frac{T_0}{l_e}$ and $F = q\mathcal{E}$ i.e. force applied to an electron by an external electric field, $\mathcal{E}$.

Besides the prefactor A that is determined by the device boundary condition (i.e. the electron injection from the electrode into a-Si), the two parameters a, b in Eq. (4.12) are chosen to make sure that the trial distribution function satisfies the continuity and energy balance equations Eqs. (4.9) and (4.10).

At steady state and using the relation $J_n = nv_d$ (i.e. ignoring the diffusion current), we can rewrite (4.9) as

$$\frac{\partial n}{\partial z} = \langle \alpha_e(z, \mathcal{E}) \rangle n(z) - \frac{n(z) - n_o}{v_d \tau} \quad (4.13)$$

Expressing (10) and (13) in terms of distribution function, we get:

$$\int \rho(T) \left[\frac{df_e(T,z,\mathcal{E})}{dz} - \frac{R(T)}{v_d} f_e(z,T) + \frac{f_e(T,z,\mathcal{E})}{v_d \tau} - \frac{f_{eo}(T)}{v_d \tau} \right] dT = 0 \qquad (4.14)$$

$$\int \rho(T) \left[T \frac{df_e(T,z,\mathcal{E})}{dz} + \left(\frac{T - T_o}{l_e} - \mathcal{E} + \frac{E_0 R_e(T)}{v_d} \right) f_e(T,z,\mathcal{E}) \right] dT = 0 \qquad (4.15)$$

Here $f_{eo}(T)$ is the distribution function at thermal equilibrium. For a-Si, the carrier lifetime (τ) is orders of magnitude greater than the energy relaxation time by phonon scattering τ_e [18] and hence can be neglected. By adding the net carrier multiplication at thermal equilibrium, $\int \rho(T) R_e(T) f_{eo}(T) dT$, which is essentially zero, to Eq. (4.15), we can rewrite (4.14) as

$$\frac{d}{dz} \int \rho(T) f_e(T,z,\mathcal{E}) dT = \frac{1}{v_d} \int \rho(T) [f_e(T,z,\mathcal{E}) - f_{eo}(T)] R_e(T) dT \qquad (4.16)$$

Multiplying (4.16) with E_0 and adding the equation with (4.15), we get

$$\frac{d}{dz} \int \rho(T)(T + E_o)[f_e(T,z,\mathcal{E}) - f_{eo}(T)] dT$$

$$= \int \rho(T) \, [f_e(T,z,\mathcal{E}) - f_{eo}(T)] \left[\mathcal{E} - \frac{T - T_o}{l_e} \right] dT + \mathcal{E} n_o \qquad (4.17)$$

Integrating (4.16) and (4.17) from $z = 0$ to $z = l_a$, we get

$$\int \rho(T) f_e(T, l_a, \mathcal{E}) dT = \frac{1}{v_d} \int \rho(T) \left[\int_0^{l_a} dz \, f_e(T,z,\mathcal{E}) \right] R(T) dT + n(0) \qquad (4.18)$$

$$\int \rho(T)(T + E_o) f_e(T, l_a, \mathcal{E}) dT$$

$$= \frac{1}{l_e} \int \rho(T) \left[\int_0^{l_a} dz \, f_e(T,z,\mathcal{E}) \right] [(\mathcal{E} - \mathcal{E}_o) l_e - T] dT + P(0) \qquad (4.19)$$

where $n(0) = \int f_e(T, z = 0, \mathcal{E})\rho(T)dT$ is the electron concentration at the end of dead space of a-Si region which is essentially same as the electrons injected into cathode. $P(0) = E_0 + T(0)$ with $T(0)$ being the electron kinetic energy at injection; $T(0) = \frac{\int T\rho(T)f_e(T,0,\mathcal{E})dT}{\int \rho(T)f_e(T,0,\mathcal{E})dT}$. The value of $n(0)$ and $T(0)$ can be determined by the boundary conditions.

Equations (4.18) and (4.19) are numerically computed by substituting the trial distribution function (4.12) and the energy dependent carrier multiplication rate calculated from (4.8).

For a given set of material properties (e.g. the energy relaxation length by phonon scattering, l_e, and excitation energy for DAP, E_0), device structure (e.g. a-Si thickness l_a, and applied electric field $\mathcal{E}$, we can determine the value of a, b in (4.12) that satisfy both (4.18) and (4.19). We then use the distribution function to calculate the average carrier multiplication coefficient for a given a-Si layer thickness:

$$\overline{\langle \alpha_e(z, \mathcal{E}, l_a) \rangle} = \frac{1}{v_d}\frac{1}{l_a}\left[\int_0^{l_a} dz \frac{\int R_e(T)f_e(T,z,\mathcal{E})\rho(T)dT}{\int f_e(T,z,\mathcal{E})\rho(T)dT}\right] \quad (4.20)$$

To aid device simulations with a commercial software such as Silvaco [19], we can fit thickness dependent carrier multiplication coefficients $\overline{\langle \alpha_e(z, \mathcal{E}, l_a) \rangle}$ for electrons and holes from (20) to the empirical local field impact ionization model in Silvaco [20].

$$\overline{\langle \alpha_e(z, \mathcal{E}, l_a) \rangle} = A_n(l_a) \exp\left(-\left(\frac{B_n(l_a)}{\mathcal{E}}\right)\right) \quad (4.21)$$

It should be noted that such fit is for the convenience of device simulation, leveraging the established functions of a widely used semiconductor device simulator. Our analysis does not assume any local field approximation.

4.2 Results and Discussions

This section consists of three parts. At first, we show the DAP assisted carrier multiplication rate from the formulation in section 4.1.2. Next, we use this rate to determine the proper distribution function which simultaneously satisfies continuity and energy balance equations. This distribution function gives us thickness dependent carrier multiplication coefficient under different electric fields. Finally, we show the gain dependence of a-Si thickness and compare simulated and experimental results.

4.2.1 Defect Assisted Carrier Multiplication Rate

Experimental observations of high gain in highly doped, heavily compensated silicon p/n junction [21], [22] and amorphous silicon [23] lead us to postulate the origin of gain attributed to the high density of localized states in the band tails.

To investigate further, we calculated DAP assisted carrier multiplication initiated by energetic electrons and holes. DFT calculation was performed for bulk silicon using SIESTA package [24] to extract wavefunctions and dispersion relations of mobile bands. Generalized gradient approximation (GGA) functional [25] was used as the exchange-correlation potential. In the calculation, mesh cutoff is 100 Rydberg. We used 28×28×28 k point grid for the DFT calculation [26]. Fig. 4.2a shows the calculated electron-initiated carrier multiplication rate as a function of the electron energy. Similar analysis also produces the hole-initiated carrier multiplicate rate (Fig. 4.2b). For both calculations, we have used donor-acceptor trap density of $5 \times 10^{19}\ cm^{-3}$ and chosen the energy level of traps to be 0.25eV from the edge of the mobile bands. Compared with crystalline Si [14], [27], the carrier multiplication rate for a-Si rise sharply

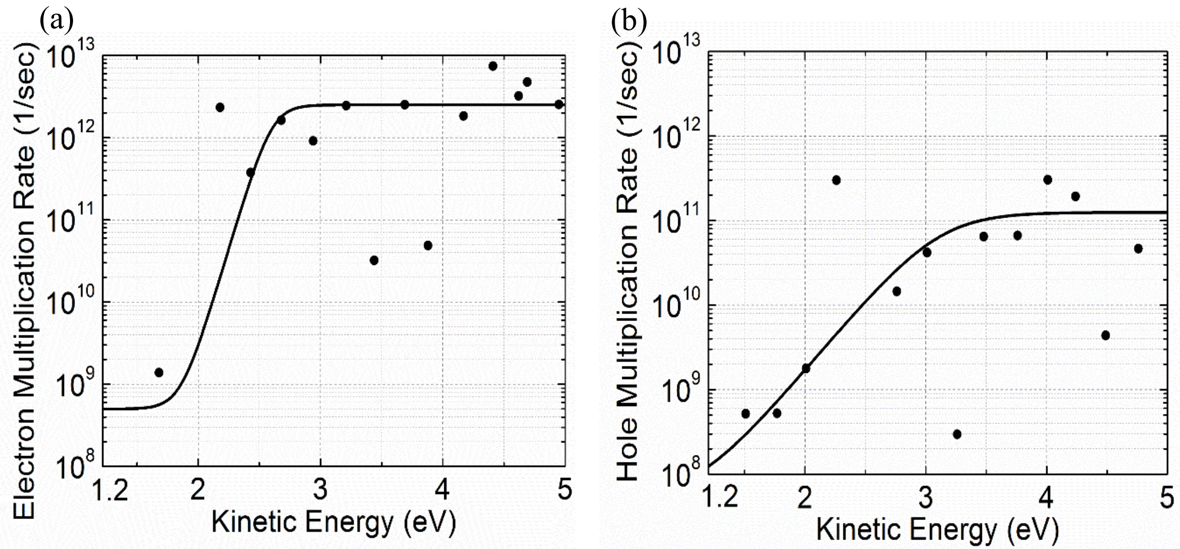

Figure 4.2: DAP assisted multiplication rate for (a) electrons and (b) holes at different kinetic energy. Solid curve is the fitted curve used for distribution function and gain calculation.

with the carrier energy due to the relaxed k selection rule by the localized donor and acceptor states. The calculations in Fig. 4.2 contain data points that deviate significantly from the trend line. Those calculations are unreliable and ignored due to the limited k-points within a supercell in the DFT band structure calculation. That is the main reason we used crystalline Si instead of a-Si to simulate the mobile bands. For a-Si, the supercell needs to be much greater than crystalline Si, thus the effective number of k-points in the simulation is reduced, leading to large fluctuations in the density of states and the multiplication rate. At higher energy, multiplication rate plateaus as a direct consequence of density of states at higher energy (shown in appendix B, Fig B.1). Since k selection rule is relaxed for defect assisted multiplication rate, the availability of possible final states primarily depends on energy conservation and follows the density of states.

4.2.2 Distribution Function and Carrier Multiplication Coefficient

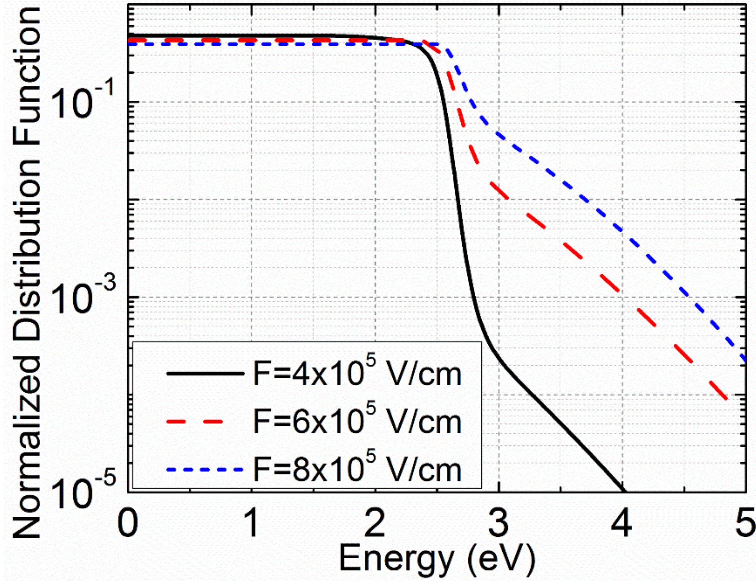

Figure 4.3: Normalized electron distribution function at the end of a 40nm thick a-Si layer under different electric fields. Normalization means the distribution function is divided by the electron concentration at the position, so the result represents the probability of an electron to have a certain energy at a given position under an electric field.

Studies from chapter 3 suggest carrier multiplication coefficient in a-Si varies with thickness [8], [28]. The thinner the a-Si layer is, the stronger the carrier multiplication coefficient is [8]. This leads to the important design criterion of using thin (30 to 60nm) a-Si as the gain medium, which is about one tenth of the multiplication region for crystalline Si avalanche detectors [29], [30]. We used the process described in section 4.1.3 to investigate thickness dependence of carrier multiplication coefficient. The first step is to find the distribution function. Using the form of literature reported distribution function with fitting parameters, a, b we compute thickness dependent carrier multiplication coefficients.

The trial distribution function for different a-Si layer thickness under different electric field are calculated. In Fig. 4.3 we show the "normalized" distribution function at the end of the layer (i.e. $z = l_a$) for a 40nm thick a-Si device as an example. Here normalization means the distribution function is divided by the electron concentration at each position, so the plot represents the probability for an electron to have a certain energy. The field dependence of the distribution function found in our method also matches the reported results in literature [3], [4]. With this distribution function, the calculated carrier multiplication coefficient is plotted in Fig. 4.4.

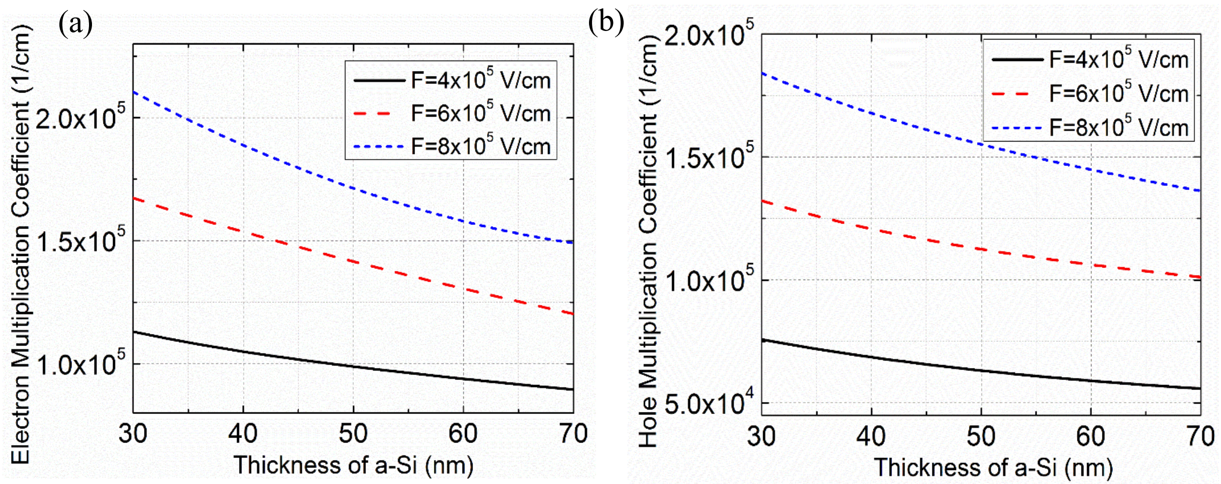

Figure 4.4: Carrier multiplication coefficient of (a) electrons and (b) holes for different thickness of a-Si.

The reduction of electron (hole) multiplication coefficient with increasing a-Si thickness can be explained from the similar trend of average kinetic energy over thickness (see appendix B, Fig B.2). The two energy loss mechanisms for an electron (hole) are phonon scattering and DAP assisted carrier multiplication. When the a-Si thickness is small compared to the length of energy relaxation by phonon scattering (i.e. $l_a < l_e$), the energy gained from the electric field can be substantially greater than the energy lost by phonon scattering, thus the overall electron (hole) energy increases as it travels through the a-Si layer. On the other hand, when the a-Si layer thickness increases so that $l_a > l_e$, the energy gains from the electric field is lost to phonon

scattering, thus the electron energy does not increase as it travels in a-Si. Fig. 4.2 shows that the carrier multiplication rate is highly sensitive to the carrier energy before the value plateaus. Hence the overall carrier multiplication coefficient for a thin a-Si layer is greater than the coefficient for a thick a-Si layer. The dependence of carrier multiplication coefficient on a-Si layer thickness is more prominently manifested in the voltage dependent gain discussed next.

4.2.3 Gain Dependence on a-Si Thickness

To study how the layer thickness affects the gain, which is an experimentally measurable quantity and most relevant to practical applications, we performed simulations on devices of varying a-Si thickness using a commercial device simulation software Silvaco which numerically solved carrier and current continuity equations coupled with Poisson's equation [19]. The simulated device structure consists of an a-Si layer sandwiched by a metal contact (cathode) and an n^+-Si substrate (anode).

Since the model for carrier multiplication in Silvaco is an empirical equation based on the local field model [20], having the carrier multiplication coefficients depend only on electric field, not layer thickness, we have taken the following steps to adapt the Silvaco program to our analysis: For each given a-Si thickness, l_a, we first extracted the parameters of local field model A_n and B_n by fitting the empirical expression to our calculated $\overline{\langle \alpha_e(z, \mathcal{E}, l_a) \rangle}$ from (21).

Next, we used the fitted A_n and B_n in device simulator. The voltage dependence of carrier multiplication coefficient extracted from Silvaco is plotted in Fig. 4.5. Here we use voltage instead of electric field to plot the data since experimentally we measure voltage dependent gain of devices, and the result shows the "efficiency" of signal amplification. Using these values, photo-

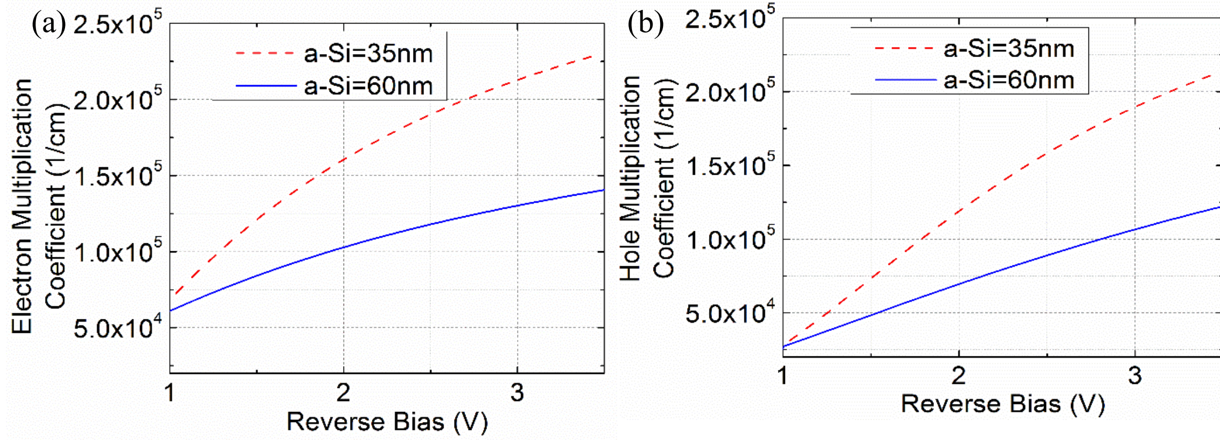

Figure 4.5: Bias dependence of carrier multiplication coefficient of (a) electrons and (b) holes for different thickness of a-Si.

current multiplication gain was calculated for each thickness at various bias voltage. As can be seen from Fig. 4.6 (a), the gain is higher for device with a thinner a-Si layer under the same voltage bias. In practice, many applications prefer a thin multiplication region due to considerations of timing jitter, excess noise, and gain-bandwidth product. We also measured the voltage dependent gain of a 30nm a-Si device and the measured and calculated results are plotted in Fig. 4.6b. The experimental and simulated gain show reasonably good agreements in several key features, but also show deviations. Importantly, both results indicate high carrier multiplication gain under very low bias voltage, demonstrating that a thin layer of disordered material such as a-Si can be a highly effective gain medium [23], [31]. Notably such thin multiplication layer is considered impossible for any avalanche photodetectors (APDs) made of crystalline materials since it is shorter than the dead space (typically of the order of 100nm). The experimental and theoretical results both show rapidly increasing gain with bias voltage. However, the experiment and theory deviate when the bias is above 3.5V. Experimental data show a clear sign of gain saturation, but the theory does not predict a similar characteristic. This is, in fact, not surprising since in our model of DAP assisted carrier multiplication process, we have assumed that all the excited DAP excitons are eventually

ionized into the mobile bands under room temperature and high electric field, contributing to the photocurrent. In reality, however, the process requires phonon excitation or field-enhanced (elastic or inelastic) tunneling. These processes can limit the achievable gain. Since our current model does not include these mechanisms, it is not surprising that our model does not predict gain saturation observed experimentally.

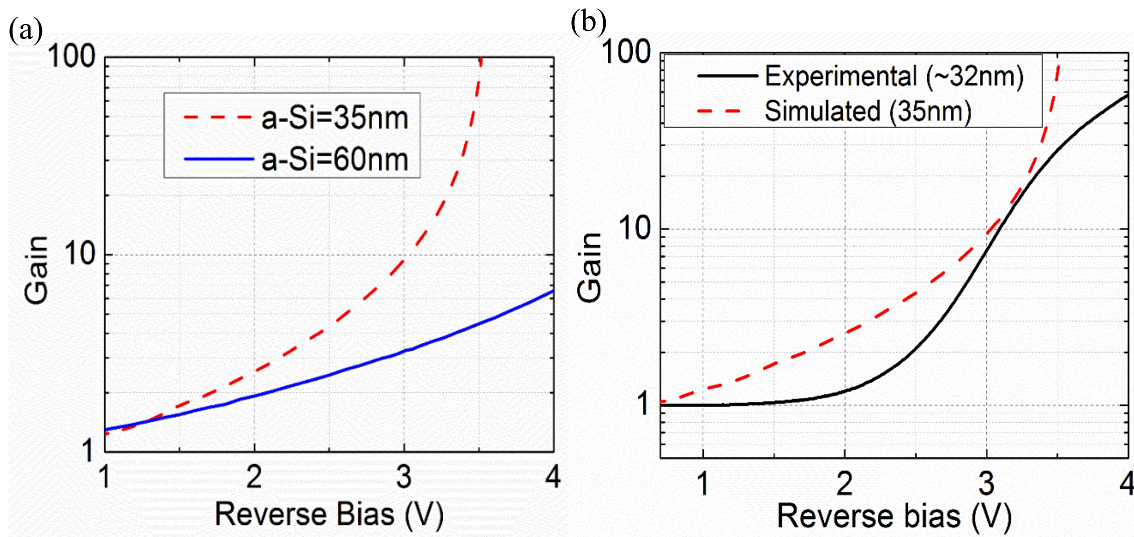

Figure 4.6: (a) Gain of a-Si photodetector devices for various thickness of a-Si. (b) Gain of simulated and experimental photodetector device of ~30nm a-Si

4.3 Conclusion

To summarize, we have developed a theoretical model for internal carrier multiplication gain in amorphous silicon. The model can be applied to other disordered materials as potential gain medium for signal amplification. We have focused on the DAP assisted carrier multiplication process where the donor-acceptor pairs are the bandtail states next to the mobile bands. With some approximations, we have combined the analytical model for the DAP pair and the DFT calculation for the mobile states including all bands and states of relevant energy. The calculation shows rapid increase in rate of carrier multiplication process involving excitation of DAP states, proving their

effect of relaxation of the k-selection rule that limits the efficiency of conventional impact ionization process.

The chapter also includes the method of finding the electron (hole) distribution function over energy by assuming a trial function with general properties matched to the published numerical and Monte Carlo simulation results of Boltzmann transport equations. The parameters in the carrier distribution function were chosen to assure the distribution satisfies both continuity equation and energy balance equation.

With the energy dependent carrier multiplication rate and the carrier distribution function, we can relate the microscopic properties to the macroscopic properties such as the electron (hole) multiplication coefficient and carrier multiplication gain for practical devices. Thus, our model has bridged the microscopic physical phenomenon and the easily measurable macroscopic device properties.

The key contributions of the analysis include: (a) establishing the physical model to demonstrate low mobility disordered materials with abundant band tail states can be a highly efficient gain medium for photocurrent amplification, (b) showing the effect of a-Si layer thickness on carrier multiplication and the benefits of having a much thinner multiplication layer than a thicker layer found in most avalanche photodetectors, and (c) showing the feasibility of high carrier multiplication gain under low bias voltage. Finally, the theoretical results are compared with experimental results from a 30nm a-Si device and to demonstrate the model's ability to describe the key features of a-Si CEP detectors except for gain saturation which is believed to be related to phonon excitation which our current model does not consider. Overall, our analysis provides an effective physical model for carrier multiplication in disordered materials which can find many important applications, especially for photodetectors, because of the advantages of low cost, easy

fabrication, and scalability.

This chapter, in part, is a reprint of material as it appears in the following work submitted for publication: M. A. R. Miah*, I. A. Niaz*, and Y. H. Lo, “Defect Assisted Carrier Multiplication in Amorphous Silicon”, IEEE Journal of Quantum Electronics.(∗→ co-first author). The dissertation author is a co-first author of this material.

References:

[1] D. V. Lang, J. D. Cohen, and J. P. Harbison, “Measurement of the density of gap states in hydrogenated amorphous silicon by space charge spectroscopy,” *Phys. Rev. B*, vol. 25, no. 8, pp. 5285–5320, Apr. 1982.

[2] W. Kohn and L. J. Sham, “Self-Consistent Equations Including Exchange and Correlation Effects,” *Physical Review*, vol. 140, no. 4A, pp. A1133–A1138, Nov. 1965.

[3] R. Thoma, H. J. Peifer, W. L. Engl, W. Quade, R. Brunetti, and C. Jacoboni, “An improved impact-ionization model for high-energy electron transport in Si with Monte Carlo simulation,” *Journal of Applied Physics*, vol. 69, no. 4, pp. 2300–2311, Feb. 1991.

[4] N. Goldsman, Y. Wu, and J. Frey, “Efficient calculation of ionization coefficients in silicon from the energy distribution function,” *Journal of Applied Physics*, vol. 68, no. 3, pp. 1075–1081, Aug. 1990.

[5] P. M. Fauchet, D. Hulin, R. Vanderhaghen, A. Mourchid, and W. L. Nighan, “The properties of free carriers in amorphous silicon,” *Journal of Non-Crystalline Solids*, vol. 141, pp. 76–87, Jan. 1992.

[6] A. R. Moore, “Electron and hole drift mobility in amorphous silicon,” *Appl. Phys. Lett.*, vol. 31, no. 11, pp. 762–764, Dec. 1977.

[7] P. G. Le Comber and W. E. Spear, “Electronic Transport in Amorphous Silicon Films,” *Phys. Rev. Lett.*, vol. 25, no. 8, pp. 509–511, Aug. 1970.

[8] I. A. Niaz, M.A.R. Miah, L. Yan, Y. Yu, Z. He, Y. Zhang, A. Zhang, J. Zhou, Y.H. Zhang and Y-H. Lo “Modeling Gain Mechanisms in Amorphous Silicon Due to Efficient Carrier Multiplication and Trap-Induced Junction Modulation,” *J. Lightwave Technol.*, vol. 37, no. 19, pp. 5056–5066, Oct. 2019.

[9] N. Sano and A. Yoshii, “Impact-ionization theory consistent with a realistic band structure of silicon,” *Phys. Rev. B*, vol. 45, no. 8, pp. 4171–4180, Feb. 1992.

[10] A. Kuligk, N. Fitzer, and R. Redmer, “*Ab initio* impact ionization rate in GaAs, GaN, and ZnS,” *Phys. Rev. B*, vol. 71, no. 8, p. 085201, Feb. 2005.

[11] S. Picozzi, R. Asahi, and A. J. Freeman, “First Principles Calculations of Auger Recombination and Impact Ionization Rates in Semiconductors,” *Journal of Computational Electronics*, vol. 2, no. 2–4, pp. 197–202, Dec. 2003.

[12] M. Isler, “Phonon-assisted impact ionization of electrons in In 0.53 Ga 0.47 As,” *Phys. Rev. B*, vol. 63, no. 11, p. 115209, Mar. 2001.

[13] G. R. Li, Z. X. Qin, G. F. Luo, B. Shen, and G. Y. Zhang, “Calculation of the electron and hole impact ionization rate for wurtzite AlN and GaN,” *Semicond. Sci. Technol.*, vol. 25, no. 11,

p. 115010, Nov. 2010.

[14] T. Kotani and M. van Schilfgaarde, “Impact ionization rates for Si, GaAs, InAs, ZnS, and GaN in the G W approximation,” *Phys. Rev. B*, vol. 81, no. 12, p. 125201, Mar. 2010.

[15] D. Ventura, A. Gnudi, G. Baccarani, and F. Odeh, “Multidimensional spherical harmonics expansion of Boltzmann equation for transport in semiconductors,” *Applied Mathematics Letters*, vol. 5, no. 3, pp. 85–90, May 1992.

[16] M. Lenzi, P. Palestri, E. Gnani, S. Reggiani, A. Gnudi, D. Esseni, L. Selmi and G. Baccarani , “Investigation of the Transport Properties of Silicon Nanowires Using Deterministic and Monte Carlo Approaches to the Solution of the Boltzmann Transport Equation,” *IEEE Trans. Electron Devices*, vol. 55, no. 8, pp. 2086–2096, Aug. 2008.

[17] N. Goldsman, L. Henrickson, and J. Frey, “A physics-based analytical/numerical solution to the Boltzmann transport equation for use in device simulation,” *Solid-State Electronics*, vol. 34, no. 4, pp. 389–396, Apr. 1991.

[18] D. S. Shen, J. P. Conde, V. Chu, and S. Wagner, “Carrier lifetime in amorphous semiconductors,” *Journal of Applied Physics*, vol. 75, no. 11, pp. 7349–7355, Jun. 1994.

[19] “Atlas User Manual.” Silvaco Inc., 30-Aug-2016.

[20] “Analysis and Simulation of Semiconductor Devices | S. Selberherr | Springer.” [Online]. Available: https://www.springer.com/us/book/9783709187548. [Accessed: 19-Feb-2019].

[21] Y.H. Liu, L. Yan, A. Zhang, D. Hall, I. A. Niaz, Y. Zhou, L. J. Sham and Y-H. Lo,, “Cycling excitation process: An ultra efficient and quiet signal amplification mechanism in semiconductor,” *Appl. Phys. Lett.*, vol. 107, no. 5, p. 053505, Aug. 2015.

[22] Y. Zhou, Y.-H. Liu, S. N. Rahman, D. Hall, L. J. Sham, and Y-H. Lo, “Discovery of a photoresponse amplification mechanism in compensated PN junctions,” *Appl. Phys. Lett.*, vol. 106, no. 3, p. 031103, Jan. 2015.

[23] L. Yan, Y. Yu, A. Zhang, D. Hall, I. A. Niaz, M.A.R. Miah, Y. Liu and Y-H. Lo, “An amorphous silicon photodiode with 2 THz gain-bandwidth product based on cycling excitation process,” *Appl. Phys. Lett.*, vol. 111, no. 10, p. 101104, Sep. 2017.

[24] J. M. Soler, E. Artacho, J. D. Gale, A. García, J. Junquera, P. Ordejón and D. Sánchez-Portal, “The SIESTA method for *ab initio* order- *N* materials simulation,” *J. Phys.: Condens. Matter*, vol. 14, no. 11, pp. 2745–2779, Mar. 2002.

[25] J. P. Perdew, K. Burke, and Y. Wang, “Generalized gradient approximation for the exchange-correlation hole of a many-electron system,” *Phys. Rev. B*, vol. 54, no. 23, pp. 16533–16539, Dec. 1996.

[26] H. J. Monkhorst and J. D. Pack, “Special points for Brillouin-zone integrations,” *Phys. Rev. B*, vol. 13, no. 12, pp. 5188–5192, Jun. 1976.

[27] E. Cartier, M. V. Fischetti, E. A. Eklund, and F. R. McFeely, “Impact ionization in silicon,”

Appl. Phys. Lett., vol. 62, no. 25, pp. 3339–3341, Jun. 1993.

[28] M. Akiyama, M. Hanada, H. Takao, K. Sawada, and M. Ishida, “Excess Noise Characteristics of Hydrogenated Amorphous Silicon p-i-n Photodiode Films,” *Jpn. J. Appl. Phys.*, vol. 41, no. 4S, p. 2552, Apr. 2002.

[29] A. R. Hawkins, T. E. Reynolds, D. R. England, D. I. Babic, M. J. Mondry, K. Streubel, and J. E. Bowers, “Silicon heterointerface photodetector,” *Appl. Phys. Lett.*, vol. 68, no. 26, pp. 3692–3694, Jun. 1996.

[30] Y. Kang, H-D. Liu, M. Moorse, M. J. Paniccia, M. Zadka, S. Litski, G., Sarid, A. Pauchard, Y-H., Kuo, H-W. Chen, W-S. Zaoui, J.E. Bowers, A. Beling, D.C. McIntosh, X. Zheng and J.C. Campbell,, “Monolithic germanium/silicon avalanche photodiodes with 340 GHz gain–bandwidth product,” *Nature Photonics*, vol. 3, no. 1, pp. 59–63, Jan. 2009.

[31] L. Yan, M. A. Raihan Miah, Y.-H. Liu, and Y.-H. Lo, “Single photon detector with a mesoscopic cycling excitation design of dual gain sections and a transport barrier,” *Opt. Lett.*, vol. 44, no. 7, p. 1746, Apr. 2019.

Chapter 5

Conclusions

This chapter will provide brief summary and outlook on the material presented in the dissertation.

5.1 Thesis Summary

This thesis presented a thorough analysis of physics of recently discovered cycling excitation process (CEP). The initial proposition was to create localized states in crystalline silicon by highly counter doping both p-n junction and relax k-selection rule. Density functional theory calculation also shows localization of carriers around impurity atoms and states inside bandgap [1], effectively increasing the probability of auger excitation.

However, high dark current stemming from high doping was one of the drawbacks of BP doped quasi disordered silicon photodiode. Furthermore, precise control of compensation ratio all over the sample is difficult to achieve. Using the rationale of having a disordered material with localized states, amorphous silicon was explored as an alternative gain medium [2].

In amorphous silicon, there are two possible gain sources: the first one is the intrinsic carrier multiplication emanating from localized states and the second one comes from the change of tunneling barrier at amorphous silicon and metal interface due to trapping of carriers in deep trap states. To distinctively demonstrate intrinsic gain, frequency dependent measurement and numerical simulation shows existence of gain at higher frequency much higher than trapping

lifetime of defect states [3].

Another key finding is that thinner a-Si gives rise to higher multiplication efficiency than thicker a-Si. The thickness dependence of gain comes from the difference in momentum relaxation time and energy relaxation time [4]. Due to very fast momentum relaxation time, at higher field, electrons reach saturation velocity and gains energy from electric field. Since, energy relaxation time is orders of magnitude higher, so the two loss mechanisms i.e. energy loss due to phonon scattering and impact ionization requires some length to take full effect and reach a steady state value. Hence, there is an effective "kinetic energy overshoot" which creates higher effective kinetic energy at thinner sample. This results in higher impact ionization coefficient in thinner amorphous silicon.

Quantitative analysis of carrier multiplication efficiency in disordered materials based on quantum mechanical calculations establishes relations between detector characteristics and key parameters such as the density of band tail states, layer thickness, and applied electric field. Higher voltage dependent gain for thinner a-Si shows the efficiency of signal amplification and this can be useful for better performance in terms of gain-bandwidth product, timing jitter and excess noise.

In a nutshell, in spite of their low mobility and high defect density, amorphous materials of small thickness can become efficient gain media to amplify signals (e.g. photocurrent) via defect assisted carrier multiplication. It is of great significance to realize this unique property of amorphous materials because of their low cost, high scalability, and simple process.

5.2 Outlook

The observation of gain mechanism in disordered material and theoretical framework opens the possibility of using a pool of amorphous materials for various applications.

The photodetector is at the heart of most CMOS image sensors. There are different requirements for photodetectors depending on the application. For biological application, highly sensitive detectors with low dark current are preferable. CEP mechanism can be employed in amorphous gain media with low dark current, high gain and low operation bias to replace conventional photodiodes in a pixel. The gain mechanism can not only be used in photodetection but also in transimpedance amplifiers to substitute amplifying functions [5]–[8]. Furthermore, there is search for visible light detection using large array SPADs. CMOS compatible silicon based CEP devices can be viable solution for 3D image sensors [9], [10].

Another possible application of the CEP mechanism can be in infrared (IR) detection which has attracted a great deal of interest for its various applications, from military use and night vision to motion detection systems and 'collision response system' in car for safety applications [11]. The existing high-performance detectors are based on technologies such as microbolometer, multi-quantum well (MQW), HgCdTe, InGaAs and Type-II superlattice structure [12]. The less expensive microbolometer-based IR system, which is based on heat absorption of IR radiation, is unable for high-speed detection and as such poses drawback in collision response in car [13], [14]. Compared to complicated and expensive process for typical far IR detectors [15], amorphous materials are cost effective to be deposited by plasma enhanced chemical vapor deposition (PECVD). As of the time of this thesis writing, highly sensitive far infrared (FIR) detector has been demonstrated using amorphous germanium (IR absorption media) and amorphous silicon (multiplication region) [16].

References:

[1] M. A. Raihan Miah, I. A. Niaz, Y.-H. Liu, D. Hall, and Y.-H. Lo, “A high-efficiency low-noise signal amplification mechanism for photodetectors,” presented at the SPIE OPTO, San Francisco, California, United States, 2017, p. 101080X.

[2] L. Yan, Y. Yu, A. C. Zhang, D. Hall, I. A. Niaz, M.A.R. Miah, Y-H. Liu, Y-H. Lo,, “An amorphous silicon photodiode with 2 THz gain-bandwidth product based on cycling excitation process,” *Appl. Phys. Lett.*, vol. 111, no. 10, p. 101104, Sep. 2017.

[3] I. A. Niaz, M.A.R. Miah, L. Yan, Y. Yu, Z. He, Y. Zhang, A. C. Zhang, J. Zhou, Y.H. Zhang and Y-H. Lo, “Modeling Gain Mechanisms in Amorphous Silicon Due to Efficient Carrier Multiplication and Trap-Induced Junction Modulation,” *J. Lightwave Technol.*, vol. 37, no. 19, pp. 5056–5066, Oct. 2019.

[4] P. M. Fauchet, D. Hulin, R. Vanderhaghen, A. Mourchid, and W. L. Nighan, “The properties of free carriers in amorphous silicon,” *Journal of Non-Crystalline Solids*, vol. 141, pp. 76–87, Jan. 1992.

[5] A. Biber, P. Seitz, and H. Jackel, “Avalanche photodiode image sensor in standard BiCMOS technology,” *IEEE Trans. Electron Devices*, vol. 47, no. 11, pp. 2241–2243, Nov. 2000.

[6] R. Xu, B. Liu, and J. Yuan, “A 1500 fps Highly Sensitive 256$\,\times\,$256 CMOS Imaging Sensor With In-Pixel Calibration,” *IEEE J. Solid-State Circuits*, vol. 47, no. 6, pp. 1408–1418, Jun. 2012.

[7] K. Murari, R. Etienne-Cummings, N. Thakor, and G. Cauwenberghs, “Which Photodiode to Use: A Comparison of CMOS-Compatible Structures,” *IEEE Sensors J.*, vol. 9, no. 7, pp. 752–760, Jul. 2009.

[8] E. R. Fossum and D. B. Hondongwa, “A Review of the Pinned Photodiode for CCD and CMOS Image Sensors,” *IEEE J. Electron Devices Soc.*, vol. 2, no. 3, pp. 33–43, May 2014.

[9] C. Niclass, A. Rochas, P.-A. Besse, and E. Charbon, “Design and characterization of a CMOS 3-D image sensor based on single photon avalanche diodes,” *IEEE J. Solid-State Circuits*, vol. 40, no. 9, pp. 1847–1854, Sep. 2005.

[10] D. Stoppa, L. Pancheri, M. Scandiuzzo, L. Gonzo, G.-F. Dalla Betta, and A. Simoni, “A CMOS 3-D Imager Based on Single Photon Avalanche Diode,” *IEEE Trans. Circuits Syst. I*, vol. 54, no. 1, pp. 4–12, Jan. 2007.

[11] J. Caniou, *Passive Infrared Detection: Theory and Applications*. 1999.

[12] C. L. Tan and H. Mohseni, “Emerging technologies for high performance infrared detectors,” *Nanophotonics*, vol. 7, no. 1, pp. 169–197, Jan. 2018.

[13] C. Chen, X. Yi, X. Zhao, and B. Xiong, “Characterizations of VO2-based uncooled

microbolometer linear array," *Sensors and Actuators A: Physical*, vol. 90, no. 3, pp. 212–214, May 2001.

[14] A. K. R. Koppula; A. Abdullah; T. Liu; O. Alkorjia; C. Zhu; C. Warder; S. Wadle; P. Deloach; S. Lewis; E. Kinzel and M. Almasri, "Material response of metasurface integrated uncooled silicon germanium oxide SixGeyO1-x-y infrared microbolometers," in *Infrared Technology and Applications XLV*, Baltimore, United States, 2019, p. 56.

[15] C. Livache, B. Martinez, N. Goubet, J. Ramade, and E. Lhuillier, "Road Map for Nanocrystal Based Infrared Photodetectors," *Front. Chem.*, vol. 6, p. 575, Nov. 2018.

[16] J. Zhou, M.A.R. Miah, Y. Yu, A.C. Zhang, Z. Zeng, S. Damle, **I.A. Niaz**, Y. Zhang, Y-H. Lo, "Room-temperature long-wave infrared detector with thin double layers of amorphous germanium and amorphous silicon", *Optics Express*, 2019 (accepted)

Appendix

A. Modeling Gain Mechanisms in Amorphous Materials

A.1 Local Electric Field Dependent Impact Ionization Model

Here, we demonstrate that local electric field dependent impact ionization model can be used to simulate carrier multiplication in a-Si and also show the role of a-Si thickness in observed gain. For carrier multiplication to occur, the electron kinetic energy has to reach threshold and the minimum distance it needs to travel to achieve that energy i.e. dead space is $d > \frac{E_0}{q\mathcal{E}}$

E_0 is the threshold ionization energy. For amorphous Silicon case, if we assume that threshold energy is $E_0 = 1.1eV$, (assuming 350meV below the 1.8eV bandgap for a-Si due to the tails in conduction and valence bands that provide the localized states), the estimated dead space is $d \approx 15nm$ under an electric field of $\mathcal{E} = 10^6\ V/cm$.

The rate equation for electron kinetic energy can be written as:

$$\frac{dT}{dt} = qv_d(\mathcal{E})\mathcal{E} - \frac{T}{\tau_e}\ ; \quad for\ 0 \le t \le t_d \qquad (A.1a)$$

$$\frac{dT}{dt} = qv_d(\mathcal{E})\mathcal{E} - \frac{T}{\tau_e} - \alpha_e v_d E_o; \quad for\ t_d \le t \le t_{tr} \qquad (A.1b)$$

T : Electron kinetic energy,

τ_e: Energy relaxation time,

α_e: Coefficient of carrier multiplication by electron (1/cm),

t_d: Time to travel through the dead space,

E_0: Energy loss in an impact ionization event.

Due to the very short momentum relaxation time [1], velocity can be expressed in terms of electric field, $v_d = \mu\mathcal{E}$ (μ is mobility, a valid parameter as shown in chapter 3).

We can define energy relaxation length due to phonon scattering as: $l_e = v_d\tau_e$, where τ_e is energy relaxation time by phonon scattering. For thin a-Si ($l_a < l_e$), we solve (A.1a) and (A.1b) by approximating α_e by an average value $\overline{\alpha_e}$

$$T(t) = v_d\tau_e[q\mathcal{E}]\left(1 - e^{-t/\tau_e}\right);\ \ for\ \ 0 \leq t \leq\ t_d \qquad (A.2a)$$

$$T(t) = v_d\tau_e[q\mathcal{E} - \overline{\alpha_e}E_o]\left(1 - e^{-(t-t_d)/\tau_e}\right) + T(t_d)e^{-(t-t_d)/\tau_e}; for\ t_d \leq t \leq t_{tr} \qquad (A.2b)$$

By changing the variable in T from time "t" to position "x" using the relation $x = v_d t$, we obtain

$$T(x) = v_d\tau_e[q\mathcal{E}]\left(1 - e^{-x/l_e}\right);\ \ for\ 0 \leq x \leq d \qquad (A.3a)$$

$$T(x) = v_d\tau_e[q\mathcal{E} - \overline{\alpha_e}E_o]\left(1 - e^{-(x-d)/l_e}\right) + d[q\mathcal{E}]e^{-(x-d)/l_e};\quad for\ d \leq x \leq l_a \qquad (A.3b)$$

For large a-Si thickness, $T(x \gg l_e) = l_e[q\mathcal{E} - \overline{\alpha_e}E_o] \equiv T(\infty)$ is position independent (or history independent). This is the regime where the local field approximation works.

When $x < l_e$

$$T(x) = l_e\left\{q\mathcal{E}\left[1 - \left(1 - \frac{d}{l_e}\right)e^{-(x-d)/l_e}\right] - \overline{\alpha_e}E_o\left[1 - e^{-(x-d)/l_e}\right]\right\} \qquad (A.3c)$$

By changing of variable of $x - d = z$, we car rewrite the equation as:

$$T(z) = l_e\left\{q\mathcal{E}\left[1 - \left(1 - \frac{d}{l_e}\right)e^{-\frac{z}{l_e}}\right]\right\} - \overline{\alpha_e}E_o\left[1 - e^{-\frac{z}{l_e}}\right] \qquad (A.4)$$

The average kinetic energy over the a-Si layer excluding the dead space is

$$\bar{T} = \int_0^{l_a-d} T(z)dz\,/(l_a-d)$$

$$\bar{T} = \int_0^{l_a-d} [L_e\left\{q\mathcal{E}\left[1-(1-\frac{d}{L_e})e^{-z/l_e}\right]-\overline{\alpha_e}E_o\left[1-e^{-z/l_e}\right]\right\}]/(l_a-d)$$

$$\bar{T} = l_e\left\{q\mathcal{E}\left[1-\left(\frac{l_e-d}{l_a-d}\right)\left(1-e^{-\frac{(l_a-d)}{l_e}}\right)\right]\right\}-l_e\overline{\alpha_e}E_o\left[1-\frac{l_e}{l_a-d}e^{-\frac{(l_a-d)}{l_e}}\right] \quad (A.5)$$

By defining, $u \equiv \frac{(l_a-d)}{l_e}$, if energy relaxation length, $l_e \gg d$, then $\frac{l_e-d}{l_a-d} \approx \frac{l_e}{l_a-d} = \frac{1}{u}$.

Then the equation for kinetic energy becomes

$$\bar{T} = l_e\left\{q\mathcal{E}\left[1-\frac{1}{u}(1-e^{-u})\right]-\overline{\alpha_e}E_o\left[1-\frac{e^{-u}}{u}\right]\right\}$$

$$\bar{T} \approx l_e[q\mathcal{E}-\overline{\alpha_e}E_o]+l_e\left[\overline{\alpha_e}E_o\frac{e^{-u}}{u}-qE\frac{(1-e^{-u})}{u}\right]$$

$$\bar{T} = T(\infty)+l_e\left[(\overline{\alpha_e}E_o+q\mathcal{E})\frac{e^{-u}}{u}-\frac{q\mathcal{E}}{u}\right] \quad (A.6)$$

For a-Si with $\tau_e{\sim}1ps$, $l_e \gg d$ (e.g. $d{\sim}15nm$ under high E-field and $l_e{\sim}100nm$). By having a-Si thickness that satisfies the condition: $d \ll l_a \ll l_e$, then $u \ll 1$

$$\bar{T} = l_e\left[q\mathcal{E}+\left(\frac{l_e}{l_a}-1\right)\overline{\alpha_e}E_o\right] > T(\infty) \quad \text{(A.7)}$$

Since kinetic energy is also a function of local electric field from (A.7) and the impact ionization coefficient is kinetic energy dependent, the multiplication coefficient is also local field dependent for thin a-Si layer. This justifies the use of local field approximation to model the behaviors of devices with thin and thick a-Si layer.

A.2 Parameters for Device Simulation of Chapter 3

Table A.1 shows material parameters used in simulation in chapter 3.

TABLE A.1
MATERIAL PROPERTIES

Material	a-Si	c-Si
Bandgap (eV)	1.8	1.08
Electron saturation velocity (cm/sec)	10^6	10^7
Hole saturation velocity (cm/sec)	10^6	10^7
Electron affinity (χ) (eV)	4.1	4.17
Richardson constant (A/cm^2/K^2)	197	110
N_D (cm^{-3})	-	10^{19}

Table A.2 shows the impact ionization parameters used for c-Si and a-Si to closely match the experimental photocurrent density in Fig. 3.5.

TABLE A.2
IMPACT IONIZATION PARAMETERS

Parameter	c-Si	a-Si (45nm)	a-Si (120nm)
A_n (1/cm)	7.03×10^5	8×10^5	4×10^5
B_n (V/cm)	1.23×10^6	8×10^5	1×10^6

Table A.3 shows the junction modulation parameters used in a-Si for producing the results in Fig. 3.3.

TABLE A.3
JUNCTION MODULATION PARAMETERS

Parameter	Typical	Varied
μ_n / μ_p	200	[1, 50, 200] (Fig 1a)
E_{tD}, E_{tA} (eV)	0.89	[0.6, 0.75, 0.89] (Fig 1b)
N_{tD} (/cm^3)	5×10^{17}	$[1, 3, 5]\times10^{17}$ (Fig 1c)
N_{tA} (/cm^3)	10^{17}	-

B. Defect Assisted Multiplication Coefficient

B.1 Quantum Mechanical Calculation of Scattering Rate

From equation (4.1), (4.2) and (4.5) we can write,

$$M = \int_{r_1}\int_{r_2} \psi_{n4}^*(\boldsymbol{k_4},\boldsymbol{r_1})\psi_3^*(\boldsymbol{r_2})\frac{q^2}{4\pi\epsilon|\boldsymbol{r_1}-\boldsymbol{r_2}|}\psi_{n1}(\boldsymbol{k_1},\boldsymbol{r_1})\psi_2(\boldsymbol{r_2})d^3\boldsymbol{r_1}d^3\boldsymbol{r_2} \quad (A.1)$$

$$\psi_3(\boldsymbol{r_2}) = \frac{e^{-\frac{r_A}{a_A}}}{\sqrt{\pi a_A^3}} = \left(\frac{1}{2\pi}\right)^3\frac{1}{\sqrt{\pi a_A^3}}\int_{\boldsymbol{k_2}} G(\boldsymbol{k_2})e^{i\boldsymbol{k_2}.\boldsymbol{r_A}}\, d^3\boldsymbol{k_2} \ (A.2)$$

$$\psi_2(\boldsymbol{r_2}) = \frac{e^{-\frac{r_D}{a_D}}}{\sqrt{\pi a_D^3}} = \left(\frac{1}{2\pi}\right)^3\frac{1}{\sqrt{\pi a_D^3}}\int_{\boldsymbol{k_3}} L(\boldsymbol{k_3})e^{i\boldsymbol{k_3}.\boldsymbol{r_D}}\, d^3\boldsymbol{k_3} \ (A.3)$$

where, $G(\boldsymbol{k_2}) = \frac{8\pi a_A^3}{(1+a_A^2k_2^2)^2}$ and $L(k_3) = \frac{8\pi a_D^3}{(1+a_D^2k_3^2)^2}$ are Fourier coefficients.

Using (A.2) and (A.3), equation (A.1) can be rewritten as,

$$M = \left(\frac{1}{2\pi}\right)^6\frac{1}{\pi\sqrt{a_A^3a_D^3}}\frac{q^2}{4\pi\epsilon}\int_{\boldsymbol{k_2}} e^{i\boldsymbol{k_2}.\boldsymbol{r_{acc}}-i\boldsymbol{k_3}.\boldsymbol{r_{don}}}G(\boldsymbol{k_2})d^3\boldsymbol{k_2}$$

$$\int_{\boldsymbol{k_3}} L(\boldsymbol{k_3})\, d^3\boldsymbol{k_3}\int_{r_1}\int_{r_2}\frac{\psi_{n4}^*(\boldsymbol{k_4},\boldsymbol{r_1})\psi_{n1}(\boldsymbol{k_1},\boldsymbol{r_1})e^{i\boldsymbol{k_3}.\boldsymbol{r_2}-i\boldsymbol{k_2}.\boldsymbol{r_2}}}{|\boldsymbol{r_1}-\boldsymbol{r_2}|}d^3\boldsymbol{r_1}d^3\boldsymbol{r_2} \ (A.4)$$

Now, choosing $\boldsymbol{r_{acc}}$ as origin, and $\boldsymbol{r_{21}} = \boldsymbol{r_2}-\boldsymbol{r_1}$, we can write equation (A.4) as,

$$M = \left(\frac{1}{2\pi}\right)^6\frac{1}{\pi\sqrt{a_A^3a_D^3}}\frac{q^2}{4\pi\epsilon}\int_{\boldsymbol{k_2}} e^{-i\boldsymbol{k_3}.\boldsymbol{r_{don}}}G(\boldsymbol{k_2})d^3k_2\int_{\boldsymbol{k_3}} L(\boldsymbol{k_3})\, d^3k_3$$

$$\times\int_{r_1}\int_{r_{12}}\frac{\psi_{n4}^*(\boldsymbol{k_4},\boldsymbol{r_1})\psi_{n1}(\boldsymbol{k_1},\boldsymbol{r_1})e^{i(\boldsymbol{k_3}-\boldsymbol{k_2}).\boldsymbol{r_{12}}}e^{i(\boldsymbol{k_3}-\boldsymbol{k_2}).\boldsymbol{r_1}}}{|\boldsymbol{r_{12}}|}d^3r_1d^3\rho \ (A.5)$$

Since, ψ_{n1} and ψ_{n4} are bloch waves, they can be expressed as,

$$\psi_{n1}(\boldsymbol{k_1},\boldsymbol{r_1}) = e^{i\boldsymbol{k_1}.\boldsymbol{r_1}}u_{n1}(\boldsymbol{k_1},\boldsymbol{r_1}) \quad (A.6.1)$$

$$\psi_{n4}(\boldsymbol{k_4},\boldsymbol{r_1}) = e^{i\boldsymbol{k_4}.\boldsymbol{r_1}}u_{n4}(\boldsymbol{k_4},\boldsymbol{r_1}) \quad (A.6.2)$$

Then,

$$\int_{r_1} \psi_{n4}^*(\boldsymbol{k_4},\boldsymbol{r_1})\psi_{n1}(\boldsymbol{k_1},\boldsymbol{r_1})\, e^{i(\boldsymbol{k_3}-\boldsymbol{k_2}).\boldsymbol{r_1}} d^3\boldsymbol{r_1}$$

$$= \int_{r_1} u_{n4}^*(\boldsymbol{k_4},\boldsymbol{r_1})u_{n1}(\boldsymbol{k_1},\boldsymbol{r_1})\, e^{i(\boldsymbol{k_1}+\boldsymbol{k_3}-\boldsymbol{k_2}-\boldsymbol{k_4}).\boldsymbol{r_1}} d^3 r_1$$

$$= \left[\frac{(2\pi)^3}{V}\delta(\boldsymbol{k_3}-\boldsymbol{k_2}+\boldsymbol{k_1}-\boldsymbol{k_4})\right]\int_{r_1} u_{n4}^*(\boldsymbol{k_4},\boldsymbol{r_1})u_{n1}(\boldsymbol{k_1},\boldsymbol{r_1})\, d^3 r_1$$

$$= \left[\frac{(2\pi)^3}{V}\delta(\boldsymbol{k_3}-\boldsymbol{k_2}+\boldsymbol{k_1}-\boldsymbol{k_4})\right] C(\boldsymbol{k_1}, n_1 \colon \boldsymbol{k_4}, n_4)\ (A.7.1)$$

$$\int_{\boldsymbol{r_{12}}} \frac{e^{i(\boldsymbol{k_4}-\boldsymbol{k_1}).\boldsymbol{r_{12}}}}{|\boldsymbol{r_{12}}|} d^3\boldsymbol{r_{12}} = \frac{4\pi}{(|\boldsymbol{k_4}-\boldsymbol{k_1}|)^2}\ \ (A.7.2)$$

and,

$$\int_{\boldsymbol{k_3}} e^{-i\boldsymbol{k_3}.\boldsymbol{r_{don}}} L(\boldsymbol{k_3})\,\delta(\boldsymbol{k_1}+\boldsymbol{k_3}-\boldsymbol{k_2}-\boldsymbol{k_4}) d^3 k_3$$

$$= e^{-i(\boldsymbol{k_4}-\boldsymbol{k_1}+\boldsymbol{k_2}).\boldsymbol{r_{don}}} \frac{8\pi a_D^3}{(1+a_D^2|\boldsymbol{k_4}-\boldsymbol{k_1}+\boldsymbol{k_2}|^2)^2}\ \ (A.7.3)$$

Using (A.6) and (A.7), equation (A.5) can be found as,

$$M = \frac{8q^2\sqrt{a_D^3 a_A^3}}{V\epsilon\pi^2} C(\boldsymbol{k_1}, n_1; \boldsymbol{k_4}, n_4) D\left(a_{A,} a_D, \boldsymbol{r_{don}}, \boldsymbol{k_1}, \boldsymbol{k_4}\right)$$

where,

$$C(\boldsymbol{k_1}, n_1; \boldsymbol{k_4}, n_4) = \int_{\boldsymbol{r_1}} \frac{\psi_{n1}(\boldsymbol{k_1},\boldsymbol{r_1})}{e^{i\boldsymbol{k_1}.\boldsymbol{r_1}}} \frac{\psi_{n4}^*(\boldsymbol{k_4},\boldsymbol{r_1})}{e^{-i\boldsymbol{k_4}.\boldsymbol{r_1}}} d^3\boldsymbol{r_1}\quad (A.8.1)$$

$$D\left(a_{A,} a_D, \boldsymbol{r_{don}}, \boldsymbol{k_1}, \boldsymbol{k_4}\right) = \frac{e^{-i(\boldsymbol{k_4}-\boldsymbol{k_1}).\boldsymbol{r_{don}}}}{(|\boldsymbol{k_4}-\boldsymbol{k_1}|)^2} \int_{\boldsymbol{k_2}} \frac{e^{-i\boldsymbol{k_2}.\boldsymbol{r_{don}}}}{(1+a_A^2 k_2^2)^2 (1+a_D^2|\boldsymbol{k_4}-\boldsymbol{k_1}+\boldsymbol{k_2}|^2)^2} d^3\boldsymbol{k_2}\ \ (A.8.2)$$

C is calculated using wavefunction from DFT calculation of bulk crystalline Silicon and D is calculated numerically.

B.2 Band structure and density of states

Band diagram and density of states (DOS) were calculated in SIESTA package using 28×28×28 k points grid for bulk Si. Scissor method [2] was used to adjust the bandgap to 1.7eV.

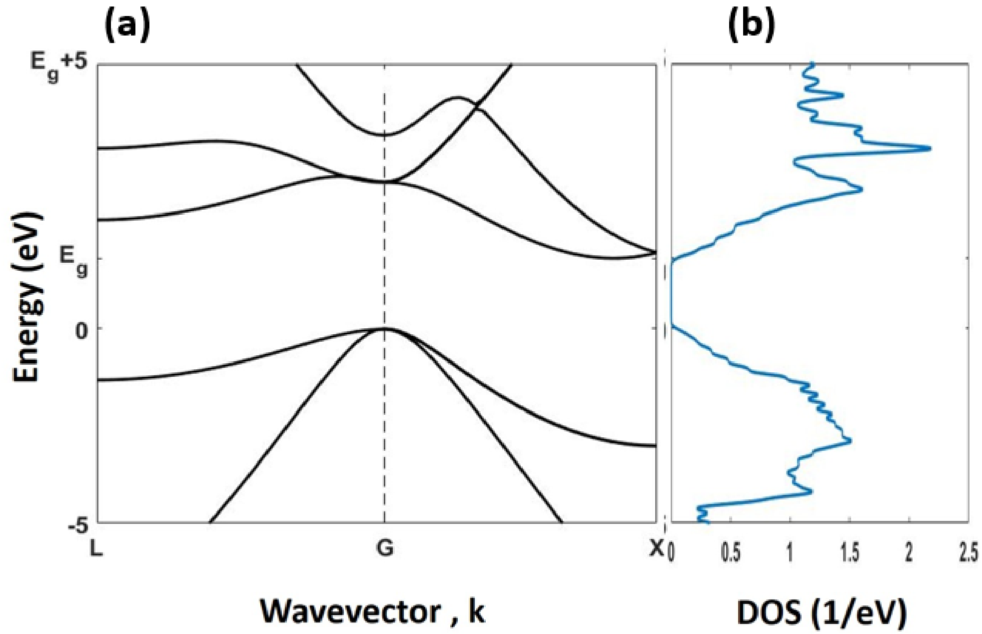

Figure B1: (a) Band structure and (b) Density of states of silicon from DFT calculation.

B.3 Average Kinetic Energy versus Thickness

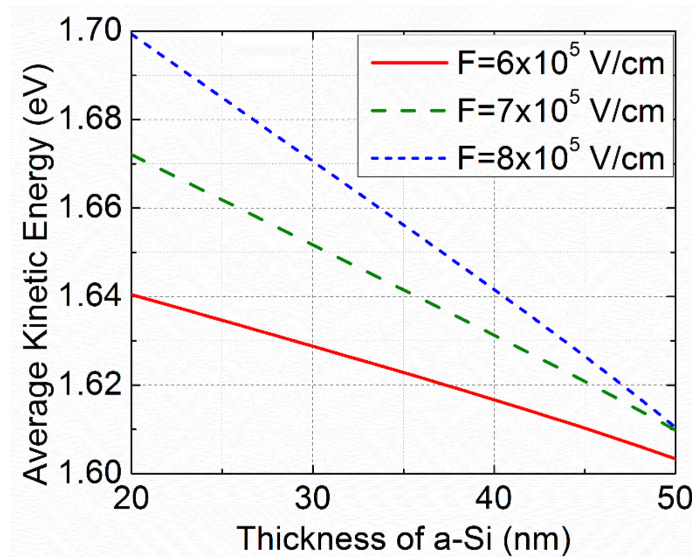

Figure B2: Average kinetic energy vs a-Si thickness.

B.4 Parameters for device simulation

We used the following parameters for Silvaco simulations for Fig. 4.5.

TABLE B.1

Material Properties

Material	**a-Si**	**c-Si**
Bandgap (eV)	1.7	1.08
Electron saturation velocity (cm/sec)	10^6	10^7
Hole saturation velocity (cm/sec)	10^4	10^7
Electron affinity (χ) (eV)	4.1	4.17
Richardson constant ($A/cm^2/K^2$)	197	110

References:

[1] P. M. Fauchet, D. Hulin, R. Vanderhaghen, A. Mourchid, and W. L. Nighan, "The properties of free carriers in amorphous silicon," *Journal of Non-Crystalline Solids*, vol. 141, pp. 76–87, Jan. 1992.

[2] K. A. Johnson and N. W. Ashcroft, "Corrections to density-functional theory band gaps," *Phys. Rev. B*, vol. 58, no. 23, pp. 15548–15556, Dec. 1998.